# The Effect of High-Pressure on Molecular Magnetism

## Alessandro Prescimone

A Thesis Submitted for the degree of Doctor of Philosophy

School of Chemistry

Faculty of Science and Engineering

University of Edinburgh

Edinburgh – October 2009

# Abstract

The effect of pressure on a number of magnetically interesting compounds such as single-molecule magnets and dimeric copper and manganese molecules has been investigated to probe the validity of ambient magneto-structural correlations.

The first chapter is an introduction to the equipment and methodologies that have been adopted to carry out the experimental high-pressure work.

The second chapter reports the first combined high-pressure single crystal X-ray diffraction and high pressure magnetism study of four single-molecule magnets (SMMs). At 1.5 GPa the structures [Mn$_6$O$_2$(Et-sao)$_6$(O$_2$CPh(Me)$_2$)$_2$(EtOH)$_6$] (**1**) – an SMM with a record effective anisotropy barrier of ~86 K – and [Mn$_6$O$_2$(Et-sao)$_6$(O$_2$C-naphth)$_2$(EtOH)$_4$(H$_2$O)$_2$] (**2**) both undergo significant structural distortions of their metallic skeletons which has a direct effect upon the observed magnetic response. Up to 1.5 GPa pressure the effect is to flatten the Mn-N-O-Mn torsion angles weakening the magnetic exchange between the metal centres. In both compounds one pairwise interaction switches from ferro- to antiferromagnetic, with the Jahn-Teller (JT) axes compressing (on average) and re-aligning differently with respect to the plane of the three metal centres. High pressure dc $\chi_M$T plots display a gradual decrease in the low temperature peak value and slope, simulations showing a decrease in |$J$| with increasing pressure with a second antiferromagnetic $J$ value required to simulate the data. The *"ground states"* change from $S$ = 12 to $S$ = 11 for **1** and to $S$ = 10 for **2**. Magnetisation data for both **1** and **2** suggest a small decrease in |$D$|, while out-of-phase ($\chi_M^{//}$) ac data show a large decrease in the effective energy barrier for magnetisation reversal. The third SMM is the complex [Mn$_3$(Hcht)$_2$(bpy)$_4$](ClO$_4$)$_3$·Et$_2$O·2MeCN (**3**·Et$_2$O·2MeCN) that at 0.16 GPa loses all associated solvent in the crystal lattice, becoming **3**. At higher pressures structural distortions occur changing the distances between the metal centres and the bridging oxygen atoms making |$J$| between the manganese ions weaker. No significant variations are observed in the JT axis of the only Mn$^{III}$ present in the structure. High-pressure dc $\chi_M$T plots display a gradual decrease in the low temperature peak value and slope. Simulations show a decrease in $J$ with increasing pressure although the ground state is preserved. Magnetisation data do not show any change in |$D$|. The

fourth SMM, $[(tacn)_6Fe_8O_2(OH)_{12}](ClO_4)_{3.9}Br_{4.1}\cdot6H_2O$, (**4**) is the largest inorganic compound ever studied at high-pressure. Up to 2.0 GPa the conformation of the complex remains largely unaffected, with the counter ions and water molecules moving around to accommodate a compression of the unit cell volume. High pressure magnetic susceptibility data collected up to 0.93 GPa confirm minimal changes in the intra-molecular exchange interactions.

The third chapter focuses on three hydroxo-bridged $Cu^{II}$ dimers: $[Cu_2(OH)_2(H_2O)_2(tmen)_2](ClO_4)_2$ (**5**), $[Cu_2(OH)_2(tben)_2](ClO_4)_2$ (**6**) and $[Cu_2(OH)_2(bpy)_2](BF_4)_2$ (**7**) have been structurally determined up to 2.5, 0.9 and 4.7 GPa, respectively. **6** and **7** have never been reported before. Pressure imposes important distortions in the structures of all three complexes, particularly on the bond distances and angles between the metal centres and the bridging hydroxo groups. **5** undergoes a phase transition between 1.2 and 2.5 GPa caused by the loss of a coordinated water molecule. This leads to a loss of symmetry and dramatic changes in the molecular structure of the complex. The structural changes are manifested in different magnetic behaviours of the complexes as seen in dc susceptibility measurements up to ~0.9 GPa: $J$ becomes less antiferromagnetic in **5** and **6** and more ferromagnetic in **7**.

The fourth chapter shows the compression of two oxo-bridged $Mn^{II}/Mn^{III}$ mixed valence dimers: $[Mn_2O_2(bpy)_4](ClO_4)_3\cdot3CH_3CN$, (**8**) has been squeezed up to 2.0 GPa whilst $[Mn_2O_2(bpy)_4](PF_6)_3\cdot2CH_3CN\cdot1H_2O$, (**9**) could be measured crystallographically up to 4.55 GPa. **9** has never been reported before, while **8** has been reported in a different crystallographic space group. The application of pressure imposes significant alterations in the structures of both complexes. In particular, in **8** the Mn-Mn separation is reduced by the contraction of some of the Mn-O bond distances, **9** shows essentially analogous behaviour: the Mn-Mn distance and nearly all the Mn-N bonds shrink significantly. The magnetic behaviour of the complexes has been measured up to 0.87 GPa for **8** and 0.84 GPa for **9**, but neither display any significant differences with respect to their ambient data.

# Acknowledgements

To properly acknowledge all the people who have contributed to the making of this thesis only one page wouldn't probably be enough… as I also would like to show my great appreciation to all the people that have also contributed to make these three and half years such a wonderful period of my life I think an entire chapter would just suffice.

I'll do my best to be as concise but comprehensive as possible.

First of all, a VERY big *"Thank you!"* goes to my great boss – Dr. Euan Brechin – not only because he gave me the chance to live in a fantastic place, doing some really top science, but also, and especially, for the great time I had working for him. He has always been extremely helpful, friendly and able to bear all my *"it is almost done"* & *"nearly ready to go"* without going crazy. Most of all, he managed to stand me every time Italy have beaten Scotland in either rugby or football (I know this last point was probably the hardest for him).

Actually the same VERY big *"Thank you!"* goes to my second great boss – Prof. Simon Parsons – for being so sociable and supportive and for making me part of his amazing group. I must not forget his numerous attempts to overcome my sloppy English trying to communicate with me in Italian… all his *"matrice"* & *"porca miseria"* are memorable.

When I also think of Euan and Simon being crazy enough to offer me a postdoc position to work with them for three more years, I will never be able to express my joy and gratitude in any appropriate way.

Going through the ranks, I must enormously thank the *"second in command"* – Dr. Steve Moggach, Dr. Javier Sanchez-Benitez and Dr. Costas Milios – as they all have joined the club of my closest friends sharing with me all the ups and downs of these years. From them I learnt so many things… crystallographic Cow-Boy attitude, football skills, how to be a Greek crystal making machine, a bit of Spanish, the secrets of the tortilla and many more. I would also like to show my appreciation to them for being so special.

Being divided between a *"better group"* and another (but which is which??) I met several wonderful people that I'll treasure for the future: Russell (another proud explorer of the spooky *"Path of Doom"*), Fraser (the actual inventor of the "better group theory"), Laura, Anna (Collins), Nick, Pete (Wood), Leigh, Ian (the Gassman), Maria, Ross, Kevin, Giorgios and the new entries Simon and Peter.

Outside the Joe Black Building I used to hang around with many people and, among them, a special mention goes to the affiliates of the so-called *"European Mafia"* (another spot-on Fraser's definition). Daniela, Maria, Pilar – a.k.a. *"the three Devils"* – have been, without a doubt, the most prominent members of it. I can't forget how much fun we had all together

trying to speak a language that was a Frankenstein of Italian, Napoletano, English, Greek and Spanish, forcing Dany to prepare her "lasagne" and watching bad movies. My flatmates Alejandro, Jone and Javier – a.k.a. *"the Spanish Community"* – have all become close friends by being such good comrades. They have been amazing in feeding me when I couldn't be bothered to heat up a frozen pizza and I think we had very good times in many occasions. Andrea, Davide, Michele, Chiara, Iria, Cecile, Giai, Ana, Luis and all the others whose names are slipping away in this moment, have been so good companions and I can only thank them.

And now… my family! A really deep *"Thank you"*. I owe them everything: in particular the moral and *ehm* practical support they generously gave me during these years spent far away from home. I will never be able to thank them enough. They are such a close and lovable family and I cannot explain what I feel for them.

Last but certainly not least Anna about whom I don't need to say more.

## Declaration

I hereby declare that except where specific reference is made to other sources, the work contained in this thesis is the original work of the author. It has been composed by the candidate and has not been submitted, in whole or in part, for any other degree, diploma or other qualification.

Alessandro Prescimone

8th October 2009

# Format of the Thesis

Each chapter of this thesis, with the exception of Chapter 1, is made of published or to-be-published papers. To fulfil the requirements of the University of Edinburgh regarding the preparation and submission of a thesis for the degree of PhD they have been reformatted accordingly.

**Chapter 2:**

*1-* A. Prescimone, C. J. Milios, S. A. Moggach, J. E. Warren, A. R. Lennie, J. Sanchez-Benitez, K. Kamenev, R. Bircher, M. Murrie, S. Parsons and E. K. Brechin, *Angew. Chemi. Int. Ed.*, 2008, **47**, 2828.

*2-* A. Prescimone, C. J. Milios, J. Sanchez-Benitez, K. Kamenev, C. Loose, J. Kortus, S. A. Moggach, M. Murrie, J. E. Warren, A. R. Lennie, S. Parsons and E. K. Brechin, *Dalton Trans.*, 2009, 4858.

*3-* A. Prescimone, J. Wolowska, G. Rajaraman, S. Parsons, W. Wernsdorfer, M. Murugesu, G. Christou, S. Piligkos, E. McInnes and E. K. Brechin, *Dalton Trans.*, 2007, 5282.

*4-* A. Prescimone, J. Sanchez-Benitez, K. Kamenev, S. A. Moggach, M. Murrie, J. E. Warren, A. R. Lennie, S. Parsons and E. K. Brechin, *Dalton Trans.*, 2009, 7390.

*5-* A. Prescimone, S. A. Moggach, J. Sanchez-Benitez, K. V. Kamenev, J. E. Warren, A. R. Lennie, S. Parsons and E. K. Brechin, *Inorg. Chem.*, 2009, **Submitted**.

**Chapter 3:**

*6-* A. Prescimone, J. Sanchez-Benitez, K. Kamenev, S. A. Moggach, J. E. Warren, A. R. Lennie, S. Parsons and E. K. Brechin, *Dalton Trans.*, 2010, 113.

**Chapter 4:**

*7-* A. Prescimone, J. Sanchez-Benitez, K. Kamenev, S. A. Moggach, J. E. Warren, A. R. Lennie, M. Murrie, S. Parsons and E. K. Brechin, *Z. Naturforsch. B,* 2010, **65b**, 221.

# Publications

1. A. Prescimone, J. Sanchez-Benitez, K. Kamenev, S. A. Moggach, J. E. Warren, A. R. Lennie, S. Parsons and E. K. Brechin, *Dalton Trans.*, 2010, 113.

2. A. Prescimone, J. Sanchez-Benitez, K. Kamenev, S. A. Moggach, J. E. Warren, A. R. Lennie, M. Murrie, S. Parsons and E. K. Brechin, *Z. Naturforsch. B, 2010, 65b, 221.*

3. A. Prescimone, J. Sanchez-Benitez, K. Kamenev, S. A. Moggach, M. Murrie, J. E. Warren, A. R. Lennie, S. Parsons and E. K. Brechin, *Dalton Trans.*, 2009, 7390.

4. A. Prescimone, S. A. Moggach, J. Sanchez-Benitez, K. V. Kamenev, J. E. Warren, A. R. Lennie, S. Parsons and E. K. Brechin, *Inorg. Chem.*, 2010, **Submitted**.

5. A. Prescimone, C. J. Milios, J. Sanchez-Benitez, K. Kamenev, C. Loose, J. Kortus, S. A. Moggach, M. Murrie, J. E. Warren, A. R. Lennie, S. Parsons and E. K. Brechin, *Dalton Trans.*, 2009, 4858.

6. C. J. Milios, R. Inglis, L. F. Jones, A. Prescimone, S. Parsons, W. Wernsdorfer and E. K. Brechin, *Dalton Trans.*, 2009, 2812.

7. L. F. Jones, A. Prescimone, M. Evangelisti and E. K. Brechin, *Chem. Comm.*, 2009, 2023.

8. A. Prescimone, C. J. Milios, S. A. Moggach, J. E. Warren, A. R. Lennie, J. Sanchez-Benitez, K. Kamenev, R. Bircher, M. Murrie, S. Parsons and E. K. Brechin, *Angew. Chemi. Int. Ed.*, 2008, **47**, 2828.

9. L. F. Jones, C. J. Milios, A. Prescimone, M. Evangelisti and E. K. Brechin, *Comptes Rendus Chimie*, 2008, **11**, 1175.

10. T. Burgarcic, A. Habtermariam, J. Stepankova, P. Heringova, J. Kasparkova, R. J. Deeth, R. D. L. Johnstone, A. Prescimone, A. Parkin, S. Parsons, V. Brabec and P. J. Sadler, *Inorg. Chem.*, 2008, **47**, 11470.

11. E. K. Brechin, L. Calucci, U. Englert, L. Margheriti, G. Pampaloni, C. Pinzino and A. Prescimone, *Inorg. Chim. Acta*, 2008, **361**, 2375.

12. A. Prescimone, J. Wolowska, G. Rajaraman, S. Parsons, W. Wernsdorfer, M. Murugesu, G. Christou, S. Piligkos, E. McInnes and E. K. Brechin, *Dalton Trans.*, 2007, 5282.

13. A. F. A. Peacock, A. Habtermariam, S. A. Moggach, A. Prescimone, S. Parsons and P. J. Sadler, *Inorg. Chem.*, 2007, **46**, 4049.

14. C. J. Milios, A. Vinslava, W. Wernsdorfer, A. Prescimone, P. A. Wood, S. Parsons, S. P. Perlepes, G. Christou and E. K. Brechin, *J. Am. Chem. Soc.*, 2007, **129**, 6547.

15. C. J. Milios, A. Prescimone, A. Mishra, S. Parsons, W. Wernsdorfer, G. Christou, S. P. Perlepes and E. K. Brechin, *Chem. Comm.*, 2007, 153.

16. C. J. Milios, R. Inglis, A. Vinslava, A. Prescimone, S. Parsons, S. P. Perlepes, G. Christou and E. K. Brechin, *Chem. Comm.*, 2007, 2738.

17. M. Manoli, A. Prescimone, A. Mishra, S. Parsons, G. Christou and E. K. Brechin, *Dalton Trans.*, 2007, 532.

18.	M. Manoli, A. Prescimone, R. Bagai, A. Mishra, M. Murugesu, S. Parsons, W. Wernsdorfer, G. Christou and E. K. Brechin, *Inorg. Chem.*, 2007, **46**, 6968.

19.	C. J. Milios, A. Prescimone, J. Sanchez-Benitez, S. Parsons, M. Murrie and E. K. Brechin, *Inorg. Chem.*, 2006, **45**, 7053.

20.	L. Calucci, G. Pampaloni, C. Pinzino and A. Prescimone, *Inorg. Chim. Acta*, 2006, **359**, 3911.

# Conferences/Meeting/Workshops attended

**2008**	**BCA08** Spring and Autumn meetings (York and Newcastle UK) 20 minutes talk given in the main session of the meeting.

**ICMM08** (Firenze, Italy) poster presented – ***prize won*** for the best poster.

**2007**	**BCA07** Spring and Autumn meetings (Kent and Oxford, UK) poster presented

**BCA/CCG** Intensive Teaching School (Durham, UK)

**EPR** National Service Workshop (Manchester, UK)

**2006**	**ICMM06** (Victoria, Canada) poster presented

**BCA06** Spring and Autumn meetings (Lancaster and Glasgow, UK) poster presented

# Contents (index)

# Chapter 1

# Introduction

# 1.1 Equipment and Procedures for High-Pressure Crystallography

### 1.1.1 *Diamond anvil cell*

The diamond anvil cell (DAC) has become the standard tool for analysing the behaviour of materials under high hydrostatic pressure. DACs are constructed from two opposed diamond anvils, which are each polished with a flat face or *culet*. A small piece of metal sheet (the *gasket*), which has a cylindrical hole drilled through it, is placed between the culet faces of the diamond anvils in order to create a sample chamber (Figure 1a). Solid samples are usually loaded with a hydrostatic liquid (so that pressure is applied evenly to the sample) and a pressure marker (Figure 2).

Although DACs are now available in several different designs, as reviewed elsewhere,[1] the Merrill-Bassett Diamond anvil cell[2] is probably the most common. In this type of cell the diamonds are supported on so-called backing seats which have holes drilled through them to allow optical alignment of the diamonds and act as a window to view the sample, as shown in Figure 1c. The backing seats are supported on small steel platens which constitute the main body of the cell, whilst three screws keep them in place and are also the mean to apply pressure to the sample. The opening angle of the platens, which is typically around 80°, defines the available incident and diffracted beam-paths that may be used during single crystal data collection. Though this restricts the proportion of the diffraction pattern that can be collected, the small size of the Merrill-Bassett DAC makes it ideal for diffraction and spectroscopic measurements, and almost all high-pressure experiments on molecular solids have been carried out with this design of cell.

Another factor of great importance in the design of these tools is the choice of material for the backing seats as this can affect the quality of the diffraction patterns. There are two common combinations. The first uses Beryllium as the material to construct the backing seats. This has the advantage of having a small absorption coefficient for X-rays ($\lambda \leq 0.7$ Å), but the disadvantage of being polycrystalline and therefore producing a powder pattern that contaminates the diffraction pattern. The
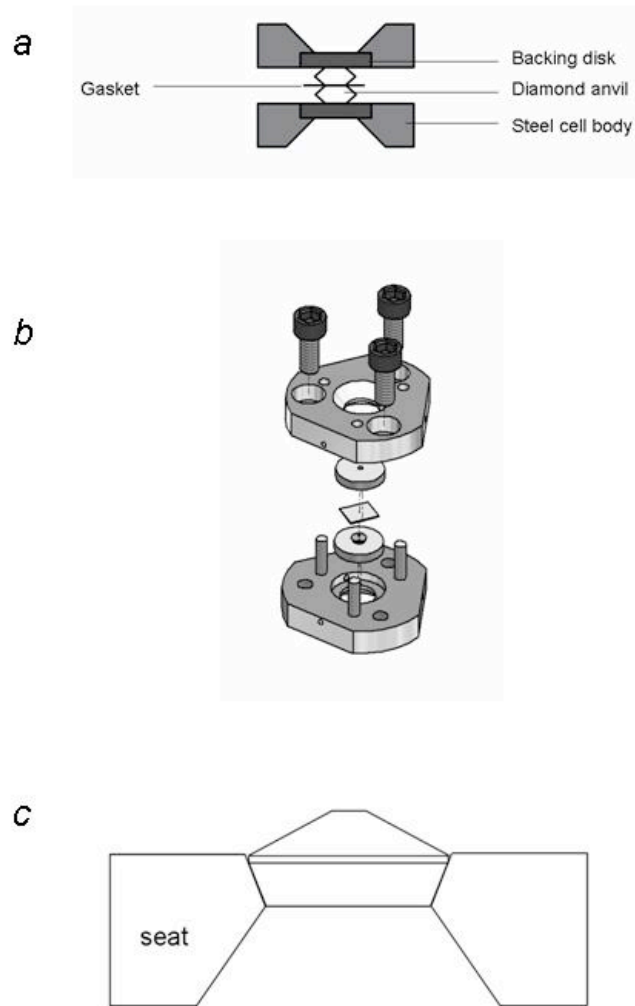
**Figure 1** (a) Schematic cross-section through a diamond anvil cell (DAC). (b) Merrill-Bassett DAC. (c) Boehler-Almax cut diamonds are embedded in the backing disk, providing good support and access through a conically ground hole.

second method uses conically ground tungsten carbide (WC) backing disks in conjunction with Boehler-Almax cut diamonds[3] which can be embedded in the WC plates themselves. The advantages of this particular design are the retaining of the same opening angle of around 80°, Figure 1c, providing support for the diamonds, maintaining the pressure range of the cell and avoiding the contaminations to the diffraction pattern as for the Beryllium design.

## 1.1.2 Hydrostatic media

Application of uniaxial pressure would quickly lead to sample destruction and so to avoid this problem samples for study at high-pressure need to be loaded into a DAC in conjunction with a hydrostatic medium. This consists of a material that stays fluid (or at least relatively soft) in the pressure range of interest, ensuring that pressure is applied uniformly.[1, 4]

The majority of high-pressure molecular crystal structures have been determined at pressures below 10 GPa, and this limit is partly the result of the properties of the hydrostatic media that are most convenient to use: hydrostatic conditions are maintained by a 16:3:1 by volume mixture of methanol, ethanol and water up to 10 GPa. Above this pressure the mixture becomes glassy losing the hydrostatic conditions, resulting in break-up of a crystalline sample or severe diffraction peak broadening. The choice of a hydrostatic medium has to consider possible chemical reactivity, interactions or solubilisation towards the sample. For these reasons,

**Table 1**: The most common hydrostatic media and their utilization limit.

| Medium | Max GPa of (quasi)hydrostaticity |
| --- | --- |
| Silicon oil | < 2.0 |
| Water | 2.5 |
| Isopropyl alcohol | 4.3 |
| Glycerine:water (3:2) | 5.3 |
| Petroleum ether | 6 |
| Penthane-isopentane (1:) | 7.4 |
| Methanol | 8.6 |
| Methanol:ethanol (4:1) | 10.4 |
| Methanol:ethanol:water (16:3:1) | 14.5 |
| Hydrogen | 177 |
| Helium | 60-70 |
| Neon | 16 |
| Argon | 9 |
| Xenon | 55 |
| Nitrogen | 13.0 |

MeOH:EtOH:$H_2O$ (although still popular) can be unsuitable for some studies. Other popular combinations are a 1:1 by volume mixture of pentane and isopentane or paraffin: the hydrostatic limits for these media are 7.4 GPa and 2 GPa, respectively.

Hydrostatic media such as the gasses Ar, He or $N_2$ are used for work above 10 GPa. Although these materials crystallise at fairly modest pressures, (1.9, GPa 3 GPa and 11.8 GPa, respectively), their low shear strengths (or softness) mean that they behave effectively as hydrostatic media well beyond these limits. However, it should be stressed that gas loading is technically much more difficult than loading with MeOH:EtOH or pentane:isopentane. Table 1 reports some of the most commonly used pressure media and their (quasi)hydrostatic limits.

### 1.1.3 Pressure measurement

The pressure within the cell is usually measured using fluorescence, with a ruby chip being the most common fluorescent probe.[5] Ruby fluorescence is characterised by an intense doublet, with sharp bands at approximately 694.2 and 692.8 nm under ambient conditions. Under compression, the doublet shifts to longer wavelengths and an empirical quasi-linear relationship has been calibrated up to 180 GPa as shown in Equation 1:[6]

$$P = 1904 \cdot \frac{\left[ \left( \lambda / \lambda_0 \right)^B - 1 \right]}{B} \tag{1}$$

For the correlation of the measured wavelength shift $\Delta\lambda$ (in nm) of one peak of the doublet with the applied pressure (GPa), B = 7.665 for quasi-hydrostatic and B = 5 for non-hydrostatic high-pressures and temperatures. Another advantage of the use of ruby fluorescence is that the splitting of the signals is a good indicator to verify if the hydrostatic conditions are maintained through all pressures. This is possible because in a hydrostatic pressure environment the splitting between the two signals of the peak remains almost constant. It is well known that non-hydrostatic stress in the pressure transmitting fluid can broaden the ruby fluorescence lines[7] as well as change the splitting of the signals.[8] In the absence of specifically designed apparatus, fluorescence measurements can be conveniently carried out using a Raman spectrometer and a visible-light laser.

A photograph of a crystal inside a pressure cell, together with a chip of ruby, is shown in Figure 2.
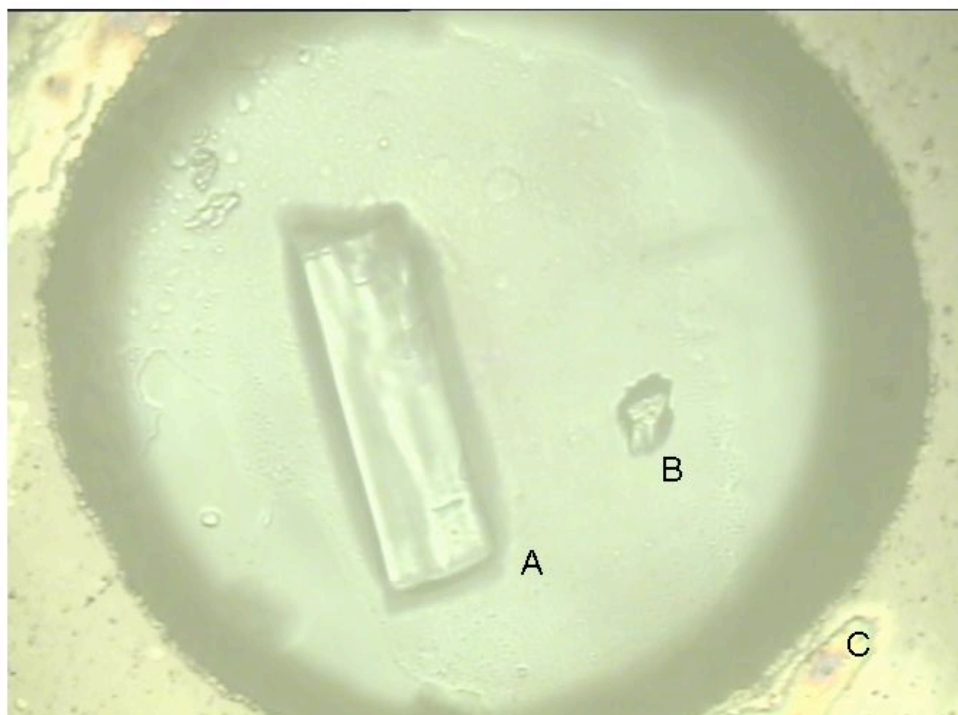
**Figure 2** A crystalline sample in a high pressure cell. The crystal of the sample is at A, the ruby chip for pressure measurement via fluorescence is at B, and the gasket is at C. The crystal is surrounded by a hydrostatic medium, in this case a mixture of pentane and isopentane.

## 1.1.4 X-ray Diffraction

In normal high-pressure data-collection on a diffractometer the pressure cell is attached to a stainless steel table (usually with superglue or some other adhesive) that has a vertical pin that can fit into a standard goniometer head. For the pressure cell to fit onto the goniometer a short collimator usually has to be used to give enough clearance for the cell to be rotated whilst collecting data (Figure 3). The small size of the pressure chamber and the limited opening angle of the pressure cell give rise to two significant problems. The first is that single-crystal samples loaded into the pressure cell have to be small enough to fit into the chamber created between the two diamond anvils and the gasket hole. The maximum size of crystals loaded in the pressure cell is generally no larger than 100 x 100 x 50μm in size. Although this is not unusually small, absorption from the backing seat and diamond anvils reduces the intensity of the measured reflections, and this is a particular issue at high
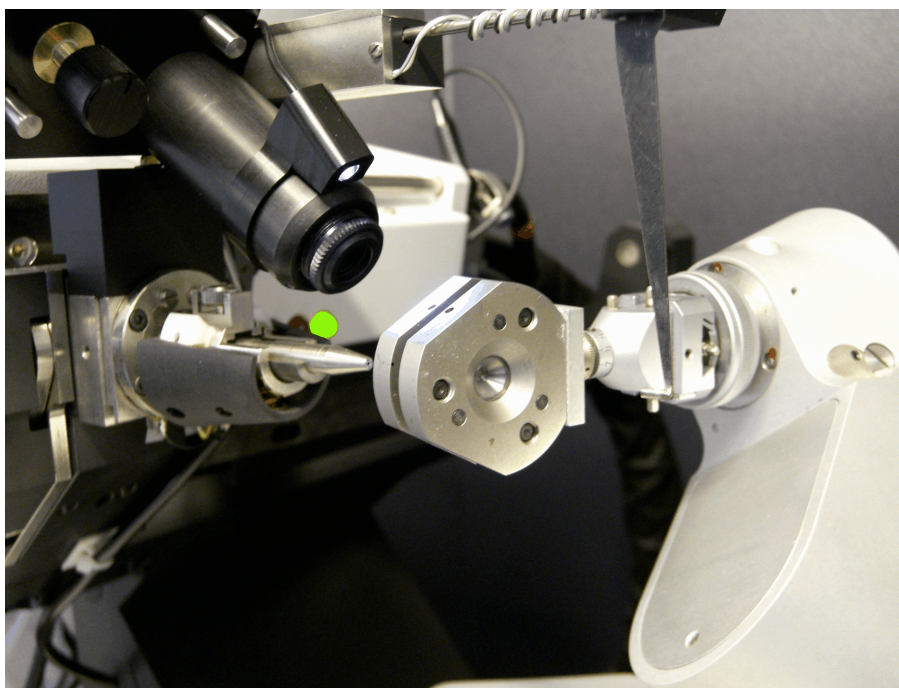
**Figure 3** A diamond anvil cell mounted on a normal diffractometer ready for data collection.
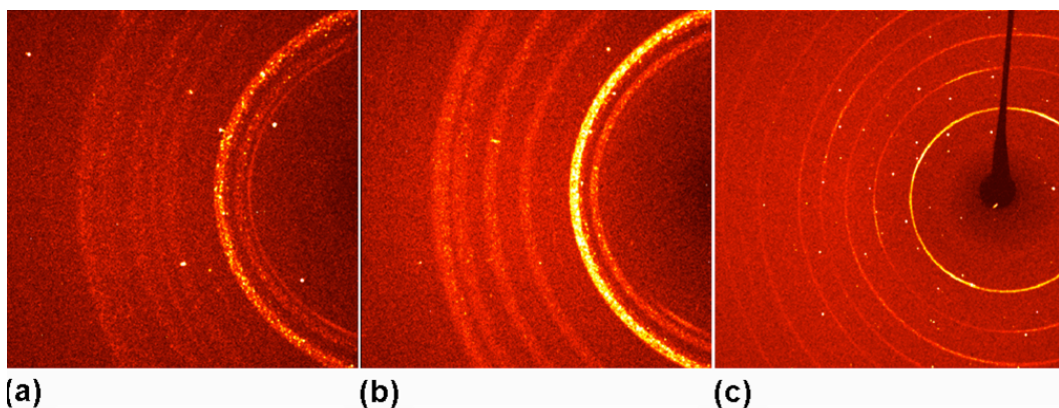


**Figure 4** images taken with a sample in **(a)** Beryllium DAC in a normal CCD diffractometer, **(b)** the same cell collecting data using synchrotron radiation and **(c)** Merrill-Bassett DAC collection using synchrotron radiation.

resolution. The second problem is a consequence of the opening angle of the cell, which for a single-crystal high-pressure cell is generally about 80°, because this restricts the volume of reciprocal space that can be sampled during a data collection. Figure 5 shows a comparison between the reciprocal spaces of a typical ambient conditions data collection with one collected in a DAC. The completeness of data sets may be as low as 20%, introducing difficulties in structure solution and refinement.

**Table 2**: Coverage statistics as a function of wavelength for $Mn_{12}$-acetate at high-pressure.

| $\lambda/Å$ | $R_1[F>4\sigma(F)]$ | Data with $F>4\sigma(F)$ | Total data | $d_{min}/Å$ | % Completeness to $d=0.8$ Å |
|---|---|---|---|---|---|
| 0.6909 | 0.0564 | 1646 | 1927 | 0.80 | 55 |
| 0.4577 | 0.0575 | 2892 | 5765 | 0.57 | 77 |
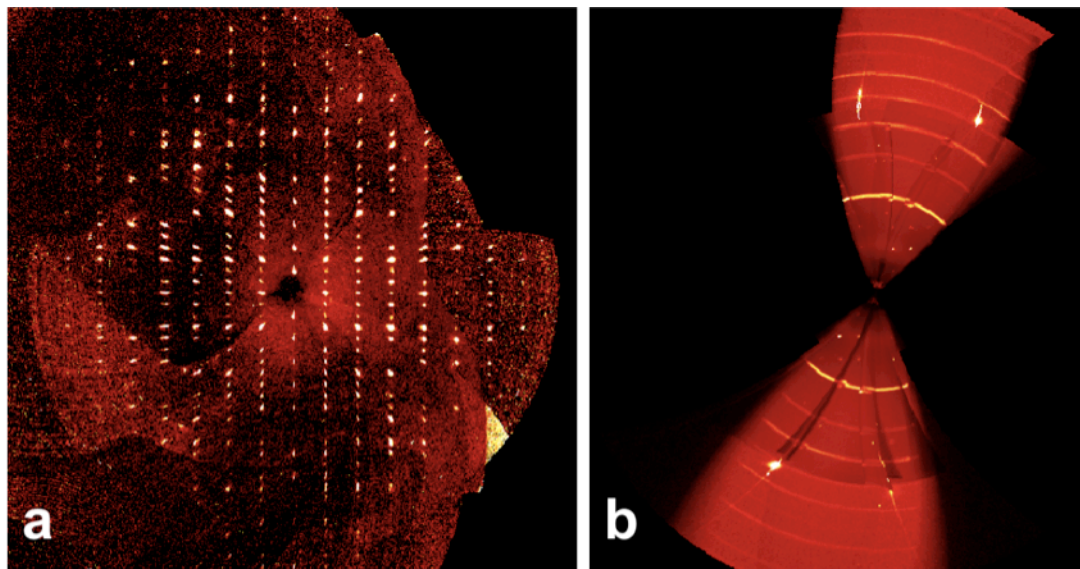


**Figure 5** images of the reciprocal space for **(a)** an ambient pressure data collection and **(b)** in a high-pressure data collection.

To overcome these problems as far as possible, use of short wavelength X-rays ($\lambda \leq$ 0.5 Å) at synchrotron sources is becoming more common as this increases the completeness compared to common lab sources, by increasing the size of the Ewald sphere, and provides an intense X-ray source to counteract the weakly diffracting nature of small samples. The data in Table 2 illustrate the improvement in completeness that can be gained by use of short wavelength radiation whilst the pictures in Figure 4 show examples of different images taken from cells with and without Beryllium and using normal lab or synchrotron X-ray sources. Two data sets were collected at $\lambda = 0.6909$ and 0.4577 Å on Station 9.8 at Daresbury Synchrotron Radiation Source using the same sample of the single-molecule magnet $Mn_{12}$-acetate (space group $I\bar{4}$).[9] The improvement in coverage in the latter data set is clear.

## *1.1.5 Data Processing*

Indexing high-pressure data from CCD detectors is non-trivial because the images contain not only sample reflections, but also intense diamond reflections and powder lines from the backing seat and gasket material. Default indexing procedures are rarely effective, and use of twin indexing programs (e.g. CELL_NOW[10] or DIRAX[11]) or manual editing of the indexing data set using a reciprocal lattice editor are required.

Integration of high-pressure data sets needs to take into account sections of the detector shaded by the pressure cell. Dawson *et al.* wrote a set of masks which take into account regions of the detector that are shaded during the integration process.[12] Facilities exist on some instruments for specifying the opening angle of a pressure cell, and this information is used together with image setting angles to determine which regions are masked. Data quality can also be enhanced by avoiding the harvesting of data overlapped with reflections from the diamond anvils.[13]

A correction for absorption by the cell may be determined empirically by measuring an experimental absorption profile or by calculating the beam paths through the different components of the cell.[14-16] Shading of the sample by the gasket forms another important systematic error, but this is difficult to treat exactly unless the precise geometrical parameters of the sample chamber, crystal and crystal position are known. Approximate formulae are available and quite straightforward to apply. Perhaps the most effective method for systematic error correction is to apply cell and gasket correction, and then take advantage of the high-redundancy of data collected on CCD detectors by 'mopping-up' residual errors using a multi-scan procedure such as SADABS[17] or SORTAV.[18]

Even after careful processing, data-sets may still contain outliers. For highly redundant data sets outliers are effectively eliminated using robust-resistant weights during merging.[19] Outliers can also be eliminated either manually or using robust-resistant weights during refinement.[20, 21]

## 1.2 Equipment and Procedures for High-Pressure Magnetochemistry.

The magnetic property measurement system [MPMS®] from Quantum Design USA[22] is probably the most advanced, user friendly and, therefore, the most popular SQUID magnetometer in the world. The MPMS can resolve magnetic moment changes as small as $10^{-8}$ emu over a wide range of temperatures and magnetic fields. There has long been a desire among the research community studying magnetic properties of materials to add pressure as a variable for the measurements in the MPMS. However, the MPMS puts severe constraints on the design of the pressure cell. The major constraint is size as the diameter of the inner bore of the MPMS is only 9 mm thus there are strong limitations on the design option to the piston-cylinder type of pressure cell. Several pressure cells of this type utilizing different design concepts have been made for the MPMS.[23-32]

### 1.2.1 Long cell

The cell described here is the one reported by Kamenev *et al.* in 2006.[26] The background of the sample support and the cell itself should be symmetric with respect to the sample, so that the SQUID signal from the sample inside the pressure cell is integrable by the standard MPMS MultiVu™ software.[22] To achieve this, the body of the pressure cell needs to be cylindrical and long enough to provide sufficient clearance between the sample and the pistons even at the maximum pressure. In the MPMS this distance is 20 mm, which corresponds to the typical dc scan length of 40 mm.

The sample chamber needs to be as large as possible in order to maximize the sample's contribution to the overall signal detected by the SQUID element. For the dc scan over 40 mm the length of the sample should not exceed ~10 mm. Further increase in the sample volume can thus only be achieved through an increase in the diameter of the sample space.

Pressure should be measured by means other than the use of manometers such as Pb, Sn, or In with known pressure dependent superconductive transitions.

An alternative method for measuring the pressure change is through the change in the external dimensions of the cell. The most sensitive method involves the use of strain gauges,[33] but they would have to be glued to the surface of the pressure cell in a position near to the sample contributing to the background: for this reason optical or mechanical micrometry should be preferred as methods to measure the changes in the dimensions of the cell.

In order for the pressure acting on the sample to be fully hydrostatic, the use of PTFE capsules has to be avoided and the pressure inside the cell should be induced by means of screws rather than with the use of external press because it is extremely difficult to keep such a long pressure cell well-aligned in the press during pressure application since a slight misalignment can lead to the piston being jammed inside the cell.

### 1.2.2  Calculations Design

The chosen outer diameter of the pressure cell of 8.7 mm is limited by the bore diameter of the MPMS sample chamber, which is just 9.0 mm. In order to maximize the sample volume the largest inner diameter of all of the reviewed pressure cells had to be used, 3.0 mm.

To verify if the expansion of the outer diameter of the cell would be sufficient to allow accurate determination of the pressure inside the cell, the Lamé equation (reported in Equation 2 used with the values of $a = 1.5$ mm and $b = 4.35$ mm, $E = 125$ GPa, and $\mu = 0.285$)

$$\frac{dD}{dP} = \frac{2b(2-\mu)}{E(b^2/a^2 - 1)} \tag{2}$$

can be used[34] to derive that the change of the diameter of the cell with pressure is $dD/dP = 16$ μm/GPa therefore a variation that would be measurable with a standard digital micrometer with a resolution of 1 μm.

The analysis has confirmed that even for the smallest sample volume, corresponding to the maximum applied pressure, the Lamé equation holds and the diameter of the cell is a linear function of the applied pressure as the cell can be treated as an infinite long cylinder.

A picture of the pressure cell is shown in Figure 6. All parts of the cell are made of BERYLCO-25 alloy. The body of the cell consists of two coaxial cylinders with

interference fit for extra strength. Because the parallelism of the bore and the surface finish are important for successful operation of the cell, all internal and external surfaces of the two cylinders have been honed and the cylinders were assembled by shrink fitting. The outer surfaces of the pistons are also honed to achieve the best possible fit between the piston and the cylinder.
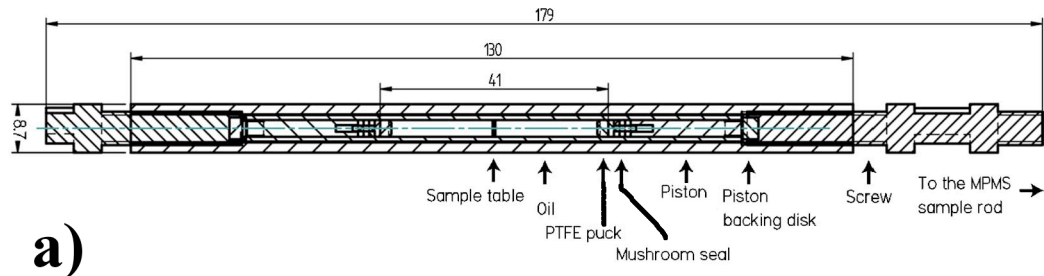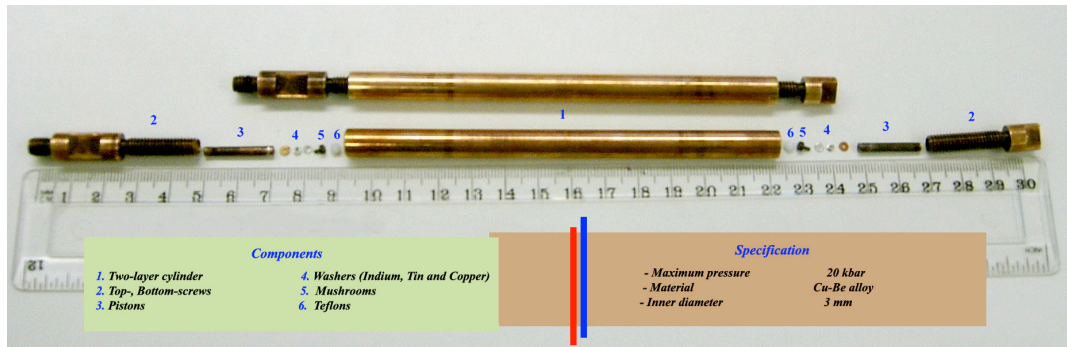


**Figure 6** The long-cell setup: **(a)** scheme and **(b)** picture.

## 1.2.3 Usage

The procedure to assemble the cell starts with one of the pistons, together with a mushroom seal with tin and copper washers, which is positioned inside the bore in such a way that the mushroom assembly just enters the bore of the cell. The piston is then backed up with a backing disk and the screw. In order to expand the tin and engage the seal, a gentle pressure on the mushroom assembly has to be applied with a rod through the opposite end of the cell. The cell is then filled with the pressure transmitting oil, Daphne 7373 oil, just above the midpoint of the bore and, at that point, the sample is inserted. The sample is mounted on a clover-shaped puck made of PTFE or gelatine with a diameter slightly larger than the inner diameter of the cell. The sample is sized in such a way that its diameter is somewhat smaller than the bore

of the cell (a powder sample needs to be pressed into a pellet prior to mounting), so that the pressure transmitting liquid can flow freely around it without moving the sample puck from its position. The puck with the sample is then inserted into the cell and positioned in the centre of the cylinder. The cell is then filled with oil almost to the top of the bore and the oil is stirred with a wire rod in order to get rid of any air bubbles trapped inside. At this stage the second piston assembly can be inserted. It has been found that for the mushroom to provide a good seal during the initial compression the tin should be expanded just as in the case of the first piston. With the other end already closed it is impossible to push on this mushroom with a rod. To overcome this problem a short tapered PTFE puck with the diameter marginally larger than the diameter of the inner bore of the cylinder can be used. Once pushed inside the bore it provides sufficient initial pressure on the mushroom to expand the soft metal seal. In order to provide a fully symmetric environment for the sample a PTFE puck has also to be inserted when the first piston is assembled (Figure 6).

At this point the cell is at ambient pressure and fully symmetric with respect to the sample so in order to maintain the symmetry of the setup at all pressures the operator just needs to make sure that the top and bottom screws that drive pistons towards each other are rotated the same number of turns. The length of the cell at ambient pressure (i.e., with the pistons all the way out) is such that it utilizes the whole available space inside the MPMS sample-loading chamber. As the pressure is increased the overall length of the cell decreases (Figure 6). Once the required pressure is achieved the pressure cell is attached to the standard sample rod by means of an M6 X 1 thread on the top screw and a simple two-way threaded adapter.

This long cell can be effectively used to measure the high-pressure response of even weakly magnetic molecular compounds, such as hydroxo-bridged copper dimers, because of the overall low background noise generated by the cell itself. Problems occur, though, at the lowest temperatures where the superconducting transition of the Indium of the washers is not only observed but also shades the features of most of the molecular materials. This means that the low temperature ac-field measurements, key features in the characterization of single-molecule magnets, cannot be carried out using this specific cell.

## 1.2.4 Pressure calibration and compressibility of Daphne 7373 oil

In order to establish the actual dependence of the diameter of the cell on the applied pressure we have conducted an experiment in which a sample of lead has been loaded into the pressure cell. The pressure was applied in steps at which the diameter
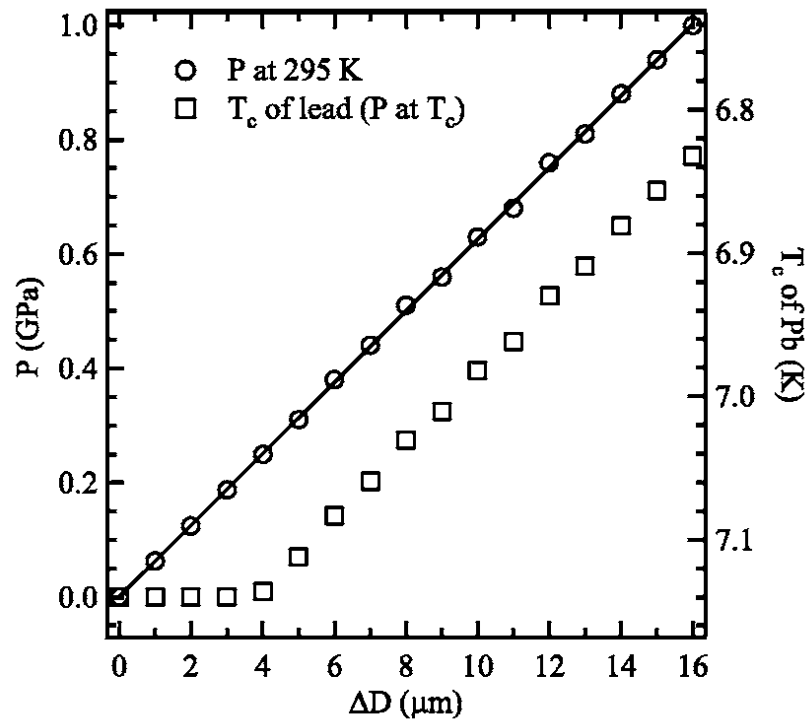


**Figure 7** Squares indicate the temperature *Tc* of the superconductive transition in Pb (right axis) and the corresponding pressure at *Tc* (left axis) as a function of the change in diameter of the pressure cell *(D)* measured at RT. Circles show the corresponding pressure at RT (left axis) as a function of the change in diameter of the pressure cell measured at RT vs *D*. The solid line is the linear fit to the data.

of the cell expanded in increments of 1 μm as measured by a digital micrometer. The cell was then placed inside the MPMS sample chamber and the temperature $T_c$ of the superconducting transition in Pb was measured, as shown in Figure 7, using the standard procedure.[28, 32]

The pressure at the superconductive transition $T_c$ of lead was calculated by its known pressure dependence $dT_c/dP = 0.405$ K/GPa.[35] Because of the difference in thermal expansion coefficients of the CuBe alloy and the oil used as a pressure transmitting fluid, the pressure drops as the pressure cell is cooled down. This explains why the first nonzero pressure point appears in the $T_c$ data at $\Delta D \approx 4$ μm (Figure 7). However,

it is clear that when the pressure is completely released at room temperature, it will remain zero when the pressure cell is cooled down. This zero reference point combined with the linear dependence of $T_c(\Delta D)$ allows us to work out how the diameter of the cell changes with pressure at room temperature. This can be achieved by
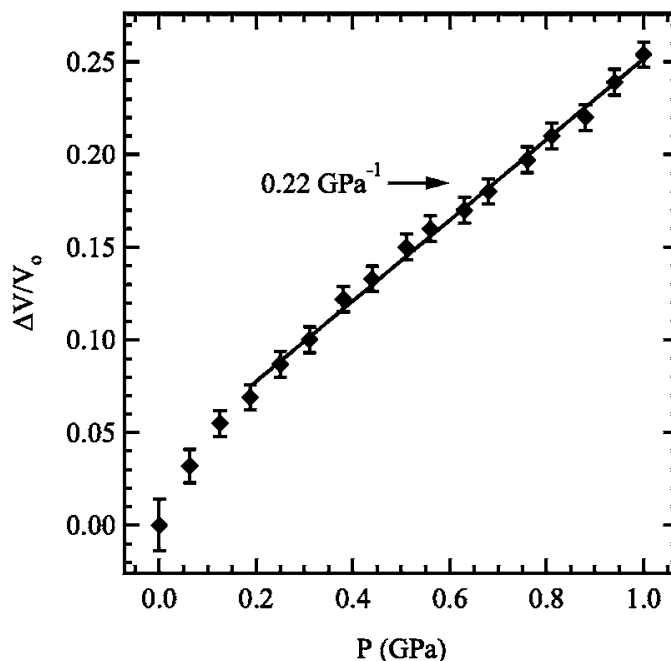


**Figure 8** Compressibility of Daphne 7373 oil. The solid line is a linear fit above 0.2 GPa.

shifting all of the high-pressure low-temperature data points, except the zero point, so that they form a continuous straight line with the point at P = 0 GPa (circles in Figure 7). The required offset representing the pressure drop inside the cell as it is cooled from 295 to 7 K is 0.24 GPa. This value is very similar to the number reported for Daphne 7373 oil.[32]

A linear fit to the room temperature data in Figure 7 shows that $dP/dD$ = 0.062 GPa/µm or that the diameter of the cell changes with pressure as $dD/dP$ = 16 µm/GPa, which is exactly the number predicted by the Lamé equation. Thus the data presented in Figure 7 show that the change in the diameter of the cell can be used as a sensitive indicator of the applied pressure. This not only eliminates the need to measure the superconductive transition at low pressure but also allows the operator of the cell to know what pressure is applied, in advance of the measurement, and also to spot an oil leak early if it occurs.

Together with the calibration of the diameter of the cell as a function of pressure, the compressibility of Daphne oil can also be measured as the simple piston-cylinder design of the cell allows extracting the volume of the oil inside the cell by
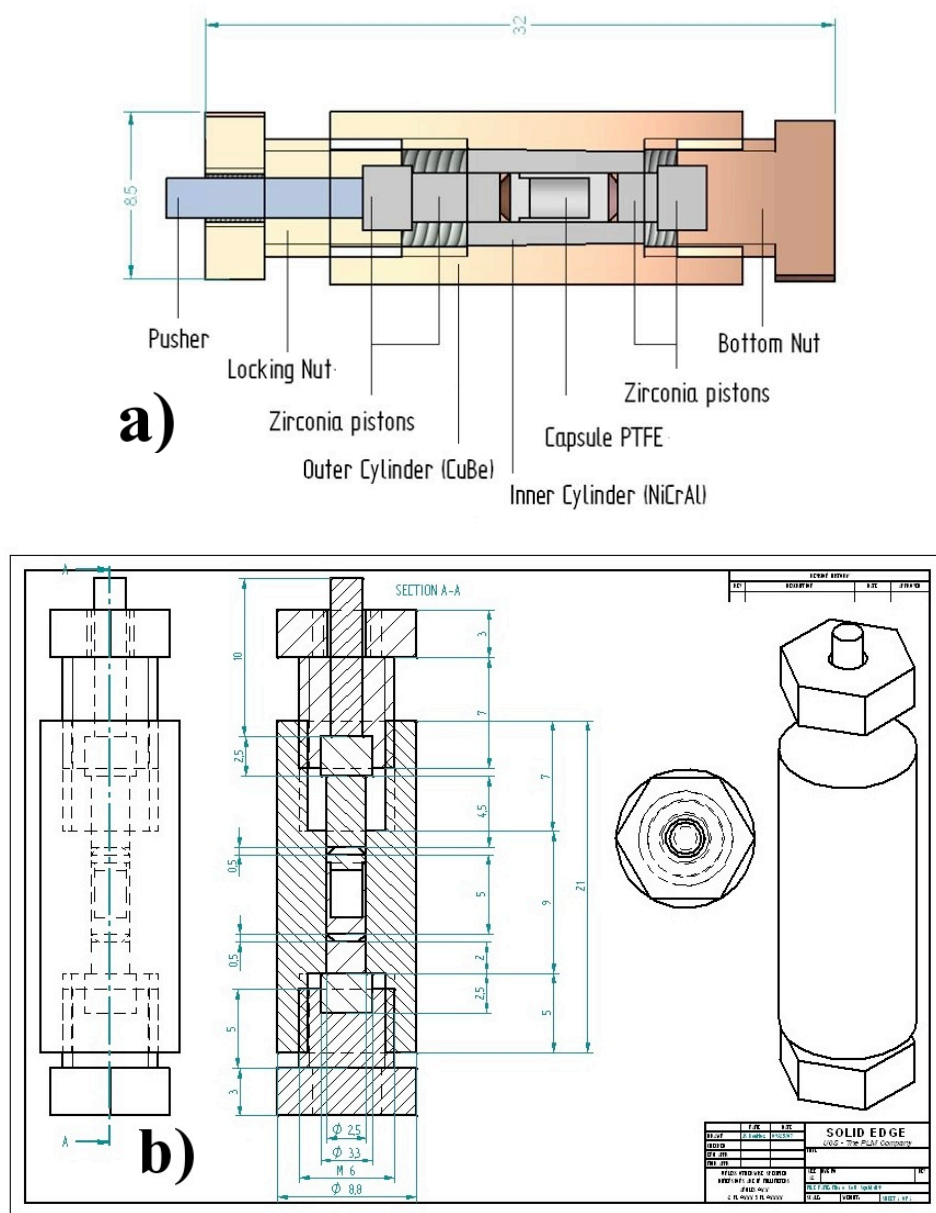


**Figure 9** The microcell: **(a)** a diagram and **(b)** a scheme.

monitoring the position of the two screws during the loading. The relative volume change as a function of pressure at $T=295$ K is reported in Figure 8. This is of interest as it provides direct information on the pressure-volume relationship for this

pressure-transmitting medium, and is constantly gaining popularity in the high-pressure community.[25, 30, 32, 36]

## 1.2.5 Microcell

The basic idea behind this particular design of pressure cell is similar to that designed by Uwatoko *et al.*[30] Because of the dimensions of the SQUID the outer diameter of this micro-cell is almost the same as the long cell (8.5 mm), but the inner diameter is only 2.5 mm, allowing higher pressures to be reached. The major difference between the two designs is the length of the main body; in the micro cell this is only 21 mm, with the total length including the pistons and the locking nuts, being just 32 mm. The biggest advantage of this setup is that the maximum pressure that can be reached is 2.0 GPa, nearly twice that of the long cell. Schematic drawings of the new high-pressure micro-cell are shown in Figures 9a and 9b with a picture of the cell with all the components is shown in Figure 10. The outer cylinder and the upper and lower nuts of the high-pressure micro-cell are made of hardened CuBe alloy (CI720B-HT), but the inner cylinder that holds the capsule with sample is made of NiCrAl alloy. A nonmagnetic Zirconia is used for the two pistons and the pusher. The high-pressure sample is put in a PTFE capsule that is placed in the centre of the inner cylinder and Daphne oil 7373 used as the pressure transmitting media.

Because of the short length of the outer cylinder the Lamé equation cannot be used to measure the pressure inside the cell, so a different approach has been adopted. In order to apply the pressure the cell is put in a press with the help of a WC pusher that acts as an external piston. Once the pressure has been applied by the press the pistons compress and shorten the cell so when the desired load has been applied the locking nut can be screwed-in to lock the pistons in position holding the pressure so that the cell can be removed from the press. The total pressure applied is extracted by building a calibration curve that plots the load applied by the press versus the actual pressure inside the cell measured through an internal manometer such as Pb, Sn or In with known pressure dependence of the superconductive transition.[37, 38]

A great advantage of this particular design of cell, together with the higher pressure limit of 2.0 GPa, is that the area where the sample is held is never in contact with the superconductive materials that pollute the signal of the sample, especially at low

temperatures. This makes this cell particularly suitable for the analysis of the ac-field features of single-molecule magnets. On the other hand, the material used can result
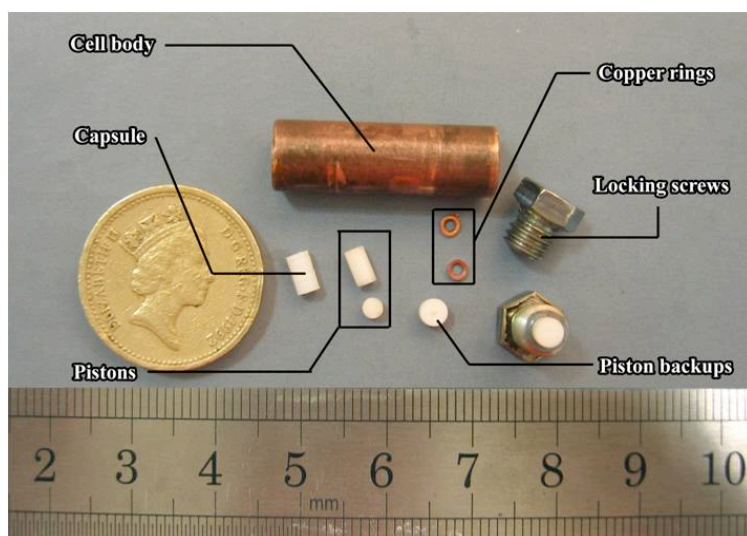


**Figure 10** A picture of the microcell with all its components.

in a large background signal that can significantly hamper detection of the magnetic response of weakly magnetic [molecular] materials.

## 1.3 References

1.      R. Miletich, D. R. Allan and W. F. Kuhs, *Rev. Mineral. Geochem.*, 2000, **41**, 445.
2.      L. Merrill and W. A. Bassett, *Rev. Sci. Instrum.*, 1974, **45**, 290.
3.      S. A. Moggach, D. R. Allan, S. Parsons and J. E. Warren, *J. Appl. Crystallogr.*, 2008, **41**, 249.
4.      R. J. Angel, M. Bujak, J. Zhao, G. D. Gatta and S. D. Jacobsen, *J. Appl. Cryst.*, 2007, **40**, 26.
5.      G. J. Piermarini, S. Block, J. D. Barnett and R. A. Forman, *J. Appl. Phys.*, 1975, **46**, 2774.
6.      P. M. Bell, J. A. Xu and H. K. Mao, eds., *Shock Waves in Condensed Matter*, Plenum Press, New York, USA, 1986.
7.      G. J. Piermarini, S. Block and J. D. BArnett, *J. Appl. Phys.*, 1973, **44**, 5377.
8.      D. M. Adams, R. Appleby and S. K. Sharma, *J. Phys. E: Sci. Instrum.*, 1976, **9**, 1140.
9.      S. A. Moggach, M. Murrie, S. Parsons and J. E. Warren, *Unpublished data.*
10.     G. M. Sheldrick, *CELL_NOW*, (2005), University of Göttingen, Göttingen, Germany.
11.     A. J. M. Duisenberg, *J. Appl. Crystallogr.*, 1992, **25**, 92.
12.     A. Dawson, D. R. Allan, S. Parsons and M. Ruf, *J. Appl. Crystallogr.*, 2004, **37**, 410.
13.     N. Casati, P. Macchi and A. Sironi, *J. Appl. Crystallogr.*, 2007, **40**, 628.
14.     D. R. Allan, S. J. Clark, S. Parsons and M. Ruf, *J. Phys.: Condens. Matter*, 2000, **12**, L613.
15.     R. J. Angel, *NATO Science Series, II: Mathematics, Physics and Chemistry*, 2004, **140**, 21.
16.     R. J. Angel, *J. Appl. Crystallogr.*, 2004, **37**, 486.
17.     G. M. Sheldrick, *SADABS Version 2006-1*, (2006) University of Göttingen, Göttingen, Germany.
18.     R. H. Blessing, *Acta Crystallogr., Sec. A*, 1995, **51**, 33.
19.     R. H. Blessing, *J. Appl. Crystallogr.*, 1997, **30**, 421.
20.     E. Prince, *Mathematical Techniques in Crystallography and Materials Science*, Springer-Verlag, New York, USA, 1982.
21.     E. Prince and W. L. Nicholson, *Acta Crystallogr., Sec. A*, 1983, **39**, 407.
22.     Quantum-Design, *http://www.qdusa.com*.
23.     *Mcell 10 pressure cell manufactured by easyLab Technologies*, website: http://www.easylab.co.uk/mcell.html.
24.     J. Diederichs, A. K. Gangopadhyay and J. S. Schilling, *Phys. Rev. B*, 1996, **54**, R9662.
25.     K. Kamashima, M. Hagiwara and H. Yoshida, *Rev. Sci. Instrum.*, 2001, **72**, 1472.
26.     K. V. Kamenev, S. Tancharakorn, N. Robertson and A. Harrison, *Rev. Sci. Instrum.*, 2006, **77**, 073905.
27.     M. Mito, H. Deguchi, T. Tajiri, S. Takagi, M. Yamashita and H. Miyasaka, *Phys. Rev. B*, 2005, **72**, 144421.
28.     S. Reich and T. Godin, *Meas. Sci. Technol.*, 1997, **7**, 1079.

29.   J. Sanchez-Benitez, S. Tancharakorn, M. K. Hutchinson and K. V. Kamenev, *J. Phys.: Conf. Ser.*, 2008, **121**, 122001.
30.   Y. Uwatoko, T. Fujiwara, M. Hedo, F. Tomioka and I. Umehara, *J. Phys.: Condens. Matter*, 2005, **17**, S1011.
31.   Y. Uwatoko, T. Hotta, E. Matsuoka, H. Mori, T. Ohki, J. L. Sarrao, J. D. Thompson, N. Mori and G. Oomi, *Rev. High Pressure Sci. Technol.*, 1998, **7**, 1508.
32.   J. Kamarad, Z. Machatova and Z. Arnold, *Rev. Sci. Instrum.*, 2004, **75**, 5022.
33.   J. Kamarad, K. V. Kamenev and Z. Arnold, in *High Pressure in Science and Technology*, ed. W. A. Trzeciakowski, World Scientific, Singapore, 1996, pp. 51-53.
34.   S. P. Timoshenko and J. N. Goodier, in *Theory of Elasticity*, McGraw-Hill, New York, 1970.
35.   B. Bireckoven and J. Witting, *J. Phys. E: Sci. Instrum.*, 1988, **21**, 841.
36.   K. Murata, H. Yoshino, H. O. Yadav, Y. Honda and N. Shirakawa, *Rev. Sci. Instrum.*, 1997, **68**, 2490.
37.   A. Eiling and J. S. Schilling, *J. Phys. F: Met. Phys.*, 1981, **11**, 623.
38.   T. F. Smith and C. W. Chu, *Phys. Rev.*, 1967, **159**, 353.

# Chapter 2

# The Effect of Pressure on

# Single-Molecule Magnets

## 2.1 Introduction

In 1952 Bleaney and Bowers[1] established a theoretical expression for the magnetic susceptibility of copper(II) acetate hydrate as a function of the temperature and the energy parameter $J$ characterising the interaction between the $Cu^{II}$ centres within the molecule. By the 1970s numerous small complexes had been synthesised allowing qualitative or quantitative correlations between structural and magnetic properties[2]. For example, Hatfield and Hodgson showed a linear relationship between $J$ and the Cu-O-Cu bridging angle $\varphi$ in planar bis($\mu$-hydroxo) copper(II) dimers.[3, 4] This was followed by other elegant studies on bis($\mu$-hydroxo)dichromium(III) complexes, bis($\mu$-halogeno)dicopper(II) compounds, dinuclear copper(II) complexes with equatorial diazine / $\mu$-1,1-azide bridge combinations, ($\mu$-oxo)diiron(III) species, and other dinuclear and oligonuclear systems.[5-32] These correlations have shown that the type and magnitude of the magnetic exchange interaction depends on the bridge identity, the metal-metal separation, the bond angles subtended at the bridging atoms, the dihedral angles between coordination planes containing the metal ions, the metal ligand bond lengths and the metal ion stereochemistries.[2]

The challenge in understanding such exchange becomes greater when the number of metal ions and hence the number of metal-metal exchange pathways increases. While in some cases it has been possible to determine semi-empirical rules that correctly predict magnetic behaviour they are usually valid only for very specific families and a robust generic theoretical explanation is almost always impossible. An "unavoidable" problem with this approach is that the molecules have a common "magnetic" skeleton but different co-ligands, counter ions, solvent molecules and crystallographic symmetry; adding some uncertainty into what contribution the non-magnetic ligands and chemical environment have. With the development of high pressure techniques it is now possible, at least in principle, to modify a structure via the application of external pressure, monitoring changes in structure via single crystal X-ray diffraction and correlating this to any changes seen in magnetic behaviour. With improvements in X-ray sources, diamond anvil cells (including Berillium-free variations) and software, single crystal high pressure crystallography

is becoming a well established area of research,[33-43] albeit one almost entirely focused on small organic molecules.[44-54] From a magnetometry point of view the situation is somewhat less developed, but constantly improving with the design and creation of more efficient pressure cells[55-57] – the fundamental problems up to now being associated with a simple lack of technology and the availability of the appropriate pressure cells able to perform experiments at the elevated pressures (and low temperatures) where structural (and magnetic) change occurs. Thus only a very limited number of studies have been published on Single-Chain Magnets (SCMs), coordination polymers and Single-Molecule Magnets (SMMs).[57-68] As yet there has been no report describing the combination of high pressure magnetic measurements with the use of high pressure single crystal X-ray diffraction. Indeed while the above studies have seen changes in the magnetic response monitored via a combination of magnetometry and INS their explanation is hindered by the lack of high pressure crystallographic data, and so remain somewhat speculative.[57, 60-62]

One of the most recent families of complexes added to the list of systems with a working semi-empirical magneto-structural correlation is the so called "Mn$_6$" family of SMMs,[69-74] a group of clusters comprising six Mn$^{3+}$ ions of general formula [Mn$_6$O$_2$(R-sao)$_6$(RCO$_2$)$_2$(L)$_{4-6}$] (where sao$^{2-}$ is the dianion of salicylaldoxime or 2-hydroxybenzaldeyhyde oxime). These Mn$_6$ compounds (Figure 1 shows complexes **1** and **2**), due to the presence of six $s = 2$ ions, can display spin ground states up to a maximum value of $S = 12$.[69-73] There are now over twenty five members of this family, whose ground state spin values are controlled via the structural distortion or "twisting" imposed by the bulky oximato groups. In particular it has been suggested that for Mn-N-O-Mn torsion angles greater than approximately 31° the pairwise exchange between two Mn$^{3+}$ ions switches from antiferromagnetic to ferromagnetic.[69-73] This chapter reports the use of high pressure magnetometry and single crystal X-ray diffraction to probe how structural changes in the core of [Mn$_6$O$_2$(Et-sao)$_6$(O$_2$CPh(Me)$_2$)$_2$(EtOH)$_6$] (**1**; Et-saoH$_2$ = 2-hydroxyphenylpropanone) and [Mn$_6$O$_2$(Et-sao)$_6$(O$_2$C-naphth)$_2$(EtOH)$_4$(H$_2$O)$_2$] (**2**; O$_2$C-naphth = β-naphthoate) are manifested in changes in the magnetic behaviour. Alongside **1** and **2** two other SMMs have been observed: [Mn$_3$(Hcht)$_2$(bpy)$_4$](ClO$_4$)$_3$·Et$_2$O·2MeCN (**1**·Et$_2$O·2MeCN; H$_3$cht is *cis,cis*-1,3,5-cyclohexanetriol). **3**, one of the smallest and

**Table 1** Crystallographic data for complex **1** at 0.5, 1.0 and 1.5 GPa and for complex **2** at 0.15, 0.5 and 1.5 GPa.

| Crystal data | 1 – [Mn$_6$(Et-sao)$_6$(EtOH)$_6$(Me$_2$COOPhen)$_2$O$_2$] | | |
|---|---|---|---|
| | 0.5 GPa | 1.0 GPa | 1.5 GPa |
| Space group | Monoclinic, $P2_1/n$ | Monoclinic, $P2_1/n$ | Monoclinic, $P2_1/n$ |
| Temperature | 300 K | 300 K | 300 K |
| $a, b, c$ (Å) | 12.7241 (13), 23.184 (7), 14.962 (2) | 12.5241 (8), 22.836 (3), 14.6696 (10) | 12.4723 (13), 22.703 (5), 14.5813 (15) |
| $\beta$ (°) | 108.029 (7) | 108.097 (4) | 108.186 (6) |
| $V$ (Å$^3$) | 4196.8 (14) | 3987.9 (7) | 3922.6 (10) |
| Radiation type | Synchrotron | Synchrotron | Synchrotron |
| $\lambda$ (Å) | 0.48650 | 0.48650 | 0.48650 |
| $\mu$ (mm$^{-1}$) | 0.96 | 1.01 | 1.02 |
| Crystal size (mm) | 0.16 × 0.15 × 0.10 | 0.16 × 0.15 × 0.10 | 0.16 × 0.15 × 0.10 |
| $T_{min}$ / $T_{max}$ | 0.34 / 0.91 | 0.37 / 0.90 | 0.30 / 0.90 |
| Measured, independent, observed reflections | 21787, 2449, 1590 | 33078, 4125, 1826 | 20027, 2288, 1422 |
| Criterion for observed reflections | $I > 2.0\ \sigma(I)$ | $I > 2.0\sigma(I)$ | $I > 2.0\sigma(I)$ |
| $R_{int}$ | 0.143 | 0.182 | 0.146 |
| $\theta_{max}$ (°) | 14.8 | 18.9 | 14.8 |
| Refinement | $F^2$ | $F^2$ | $F^2$ |
| $R$, $wR$, $S$ | 0.053, 0.089, 0.993 | 0.067, 0.106, 0.997 | 0.074, 0.122, 1.003 |
| Reflections | 2362 | 3956 | 2268 |
| Parameters | 538 | 538 | 538 |
| Restraints | 880 | 892 | 840 |
| $\Delta\rho_{max}, \Delta\rho_{min}$(eÅ$^{-3}$) | 0.41, –0.52 | 0.70, –0.57 | 0.79, –0.46 |

| Crystal data | 2 – [Mn$_6$O$_2$(Et-sao)$_6$(EtOH)$_4$(NaphtCOO)$_2$(H$_2$O)$_2$] | | |
|---|---|---|---|
| | 0.15 GPa | 0.5 GPa | 1.5 GPa |
| Space group | Monoclinic, $P2_1/c$ | Monoclinic, $P2_1/c$ | Monoclinic, $P2_1/c$ |
| Temperature | 300 K | 300 K | 300 K |
| $a, b, c$ (Å) | 16.009 (2), 19.7972 (15), 14.6045 (17) | 15.7129 (17), 19.6097 (12), 14.3635 (14) | 14.963 (4), 19.358 (3), 14.165 (4) |
| $\beta$ (°) | 112.994 (10) | 112.834 (8) | 110.929 (14) |
| $V$ (Å$^3$) | 4260.9 (9) | 4078.9 (7) | 3832.4 (16) |
| Radiation type | Synchrotron | Synchrotron | Synchrotron |
| $\lambda$ (Å) | 0.47670 | 0.47670 | 0.47670 |
| $\mu$ (mm$^{-1}$) | 0.94 | 0.98 | 1.05 |
| Crystal size (mm) | 0.13 × 0.09 × 0.08 | 0.13 × 0.09 × 0.08 | 0.13 × 0.09 × 0.08 |
| $T_{min}$ / $T_{max}$ | 0.62 / 0.93 | 0.62 / 0.92 | 0.66 / 0.92 |
| Measured, independent, observed reflections | 20999, 3738, 2634 | 20346, 3602, 2548 | 18519, 2489, 1266 |
| Criterion for observed reflections | $I > 2.0\sigma(I)$ | $I > 2.0\sigma(I)$ | $I > 2.0\sigma(I)$ |
| $R_{int}$ | 0.086 | 0.076 | 0.171 |
| $\theta_{max}$ (°) | 17.3 | 17.4 | 15.4 |
| Refinement | $F^2$ | $F^2$ | $F^2$ |
| $R$, $wR$, $S$ | 0.049, 0.062, 0.989 | 0.047, 0.058, 1.344 | 0.072, 0.088, 1.144 |
| Reflections | 3320 | 3134 | 2336 |
| Parameters | 539 | 539 | 539 |
| Restraints | 789 | 789 | 794 |
| $\Delta\rho_{max}, \Delta\rho_{min}$(eÅ$^{-3}$) | 0.34, –0.36 | 0.35, –0.33 | 0.74, –1.54 |

simplest Single-Molecule Magnets known and one of the very few, if not the only

one, to contain only one $Mn^{III}$ ion[75, 76] and $[(tacn)_6Fe_8O_2(OH)_{12}](ClO_4)_{3.9}Br_{4.1} \cdot 6H_2O$, (**4**; tacn = 1,3,5-triazacyclononane) – the first $Fe^{III}$ based SMM – a complex that also represents the largest inorganic complex ever studied by single crystal high pressure X-ray diffraction.

## 2.2 High-Pressure effects on the magneto-structural correlation in two hexametallic SMMs

### 2.2.1 Experimental Section

**Synthesis**

All reactions were carried out in aerobic conditions using materials as received. $[Mn_6O_2(Et\text{-}sao)_6(O_2CPh(Me)_2)_2(EtOH)_6]$ **1** and $[Mn_6O_2(Et\text{-}sao)_6(O_2C\text{-}naphth)_2(EtOH)_4(H_2O)_2]$ **2** were made as previously described.[72, 74]

**X-ray crystallography**

High-pressure single crystal experiments were carried out using a Merrill-Bassett diamond anvil cell[34] (half-opening angle 40°), equipped with Boehler-Almax diamonds with 600 μm culets and a tungsten gasket[77]. Petroleum ether was used as hydrostatic medium and a small ruby chip was loaded into the cell as the pressure calibrant with the ruby fluorescence used to measure the pressure.[78] Diffraction data were collected using synchrotron radiation of wavelength $\lambda$ = 0.4865 Å for **1** and $\lambda$ = 0.47670 Å for **2** at room temperature on a Bruker Smart APEX II diffractometer[35, 79] on Station 9.8 at SRS, Daresbury Laboratory. Integrations were carried out using the program SAINT[36] and absorption corrections with the program SADABS[40] and SHADE.[37] Data collections were taken at approximately 0.5, 1.0 and 1.5 GPa. For **1** and 0.15, 0.5 and 1.5 GPa for **2**. Refinements of the compressed form of **1** and **2** were carried out starting from the coordinates obtained from a separate data collection carried out under ambient conditions. The program CRYSTALS[41] was used to refine the structures against $F^2$ using the reflections with $I > 2\sigma(I)$. Due to the low completeness of the data sets, some thermal similarities, overall rigid-body motion tensors (TLS[80]) and vibrational restraints together with limits on C-C

distances have been applied; all the C, N, Mn and O atoms, except the disordered ligands, were refined with anisotropic displacement parameters, while for compound **2** the naphthalene has been refined as rigid group. Unit cells and refinement parameters are reported in Table 1.
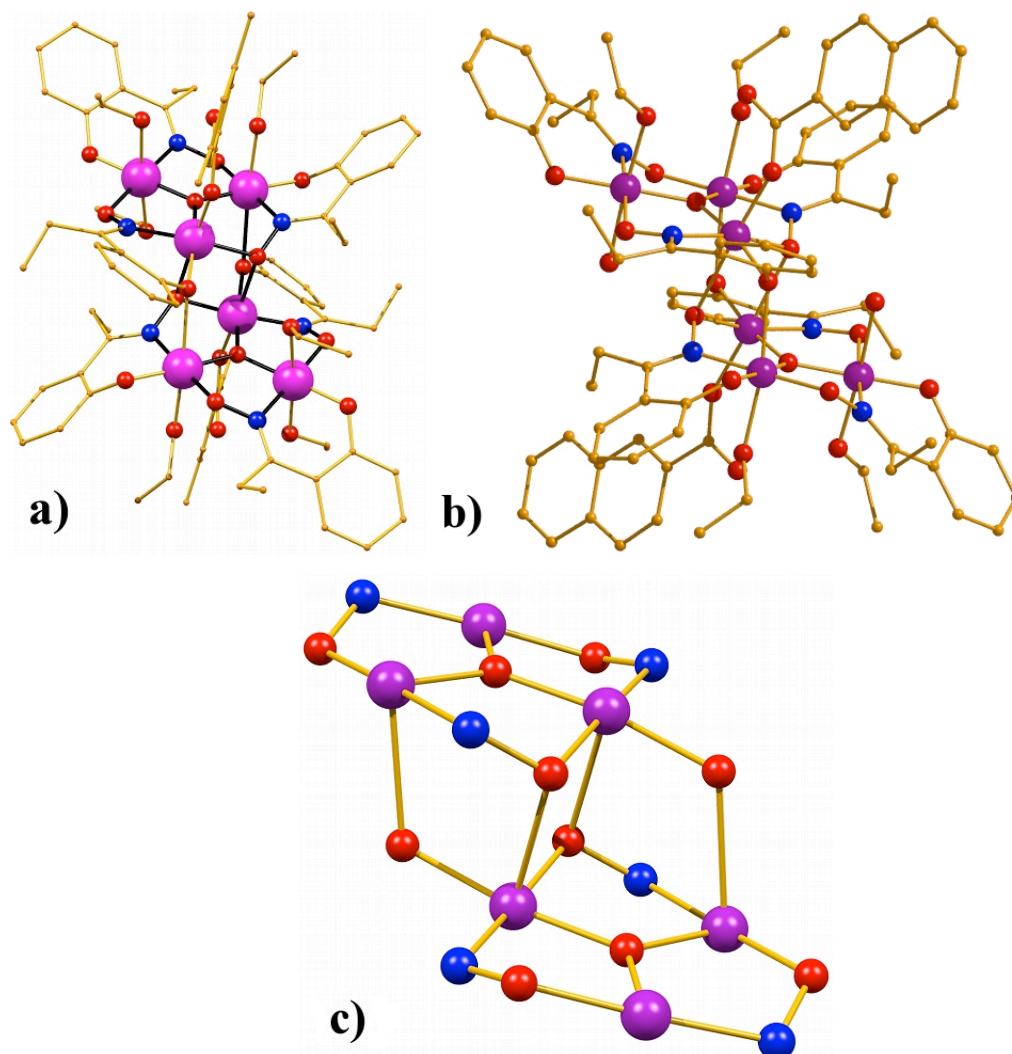


**Figure 1** a) The molecular structure of complex **1**. b) The molecular structure of complex **2**. c) The metallic skeleton common to **1** and **2**. Colour code: Mn = purple, O = red, N = blue, C = gold.

## Magnetic measurements.

Variable temperature magnetic susceptibility (dc and ac) measurements were made on a Quantum Design Magnetic Property Measurement System (SQUID magnetometer) equipped with a 5T magnet operating in the 300-2 K temperature range for **1** and on a Quantum Design Magnetic Property Measurement System

(SQUID magnetometer) equipped with a 7T magnet operating in the 300-2 K temperature range for **2**. Diamagnetic corrections were applied using Pascal's constants. For the high-pressure magnetic measurements a cell of piston-cylinder design capable of reaching 2.0 GPa was constructed. The body of the pressure cell was made of non-magnetic CrNiAl and BERYLCO-25 alloys with zirconia rods used as pistons. The sample was contained inside a PTFE capsule, with Daphne 7373 oil
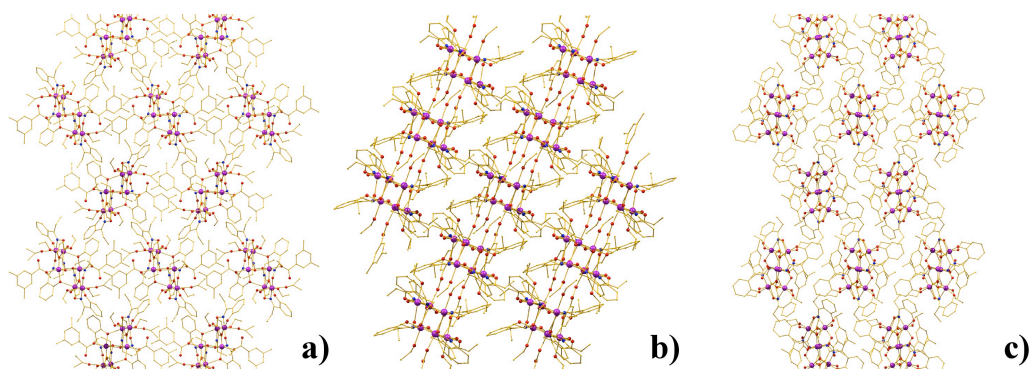


**Figure 2** Packing diagrams of **1** along the three crystallographic axes *a*, *b* and *c*

(IDEMITSU-ILS) used as the pressure transmitting medium. Pressure was applied in a hydraulic press and was calibrated by the load. Data were collected at approximately 0.75, 1.1, 1.5 and 1.75 GPa for complex **1** and 0.44, 0.7, 1.1 and 1.40 GPa for **2**

### 2.2.2  Results and Discussion

#### Description of Structures

The structures of **1** and **2** are analogous and so below we concentrate on describing the structure of **1** only. The core of   (Figure 1) contain a non-planar $[Mn^{III}_6(\mu_3\text{-}O^{2-})_2(\mu_2\text{-}OR)_2]^{12+}$ unit of two off-set, stacked $[Mn^{III}_3(\mu_3\text{-}O^{2-})]^{7+}$ triangular subunits linked by two central oximato O-atoms and two peripheral phenolate O-atoms, with the remaining four Et-sao$^{2-}$ ligands bridging in a $\eta^1{:}\eta^1{:}\eta^1{:}\mu_2$-fashion along the edges of the $[Mn^{III}_3(\mu_3\text{-}O^{2-})]^{7+}$ triangles. All six metal ions are six-coordinate and in distorted octahedral geometries, and are in the 3+ oxidation state – assigned using a combination of charge-balance and bond-length considerations, and BVS calculations. The Mn$^{III}$ centres exhibit a Jahn-Teller (JT) distortion, as expected for a

high-spin $d^4$ ion in near-octahedral geometry, each of which is approximately perpendicular to the $Mn_3$ planes. The symmetry equivalent "upper" and "lower" triangular faces are each occupied by one monodentate carboxylate and two EtOH molecules. In the crystal, molecules of **1** lie in a head-to-tail fashion such that the individual *S-shaped* molecules combine to form a zig-zag like packing of the molecules (Figure 2). The closest inter-molecular interactions are of the H-H type and occur between the methyl groups of the carboxylate ligand and the ethyl groups of the Et-sao$^{2-}$ ligands belonging to neighbouring oximic ligands.
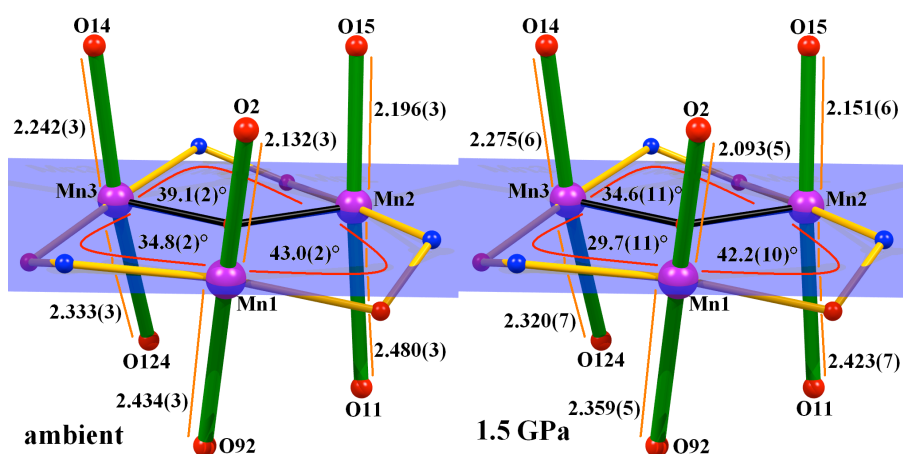


**Figure 3** Comparison of the Jahn–Teller bond lengths and Mn-N-O-Mn torsion angles in **1** at ambient conditions and at 1.5 GPa. Colour code: Mn = purple, O = red, N = blue, JT axes = green bonds.

**Table 2** Comparison of the amplitude of the Mn-O-N-Mn torsion angles (°) as function of pressure for complex **1**.

| P (GPa) | Mn1-O-N-Mn2 | Mn2–O–N-Mn3 | Mn3-O-N-Mn1 |
|---|---|---|---|
| 0 | 43.0(2) ° | 39.1(2) ° | 34.8(2) ° |
| 0.5 | 43.0(8) ° | 37.1(8) ° | 31.1(8) ° |
| 1.0 | 42.1.(8) ° | 35.1(8) ° | 30.4(8) ° |
| 1.5 | 42.2(10) ° | 34.6(11) ° | 29.7(11) ° |
| Δ/σ | 0.88 | 4.02 | 4.74 |

## Effect of Pressure on 1

The first, and perhaps most obvious, effect is the constant compression of the unit cell (Table 1). No strong intermolecular interactions, H-bonds or π-π stacking, are present in the structure and thus the compression of the cell is likely due to the reduction of voids between the molecules in the lattice. The application of pressure leads to some short inter-molecular H-H contacts: the two shortest contacts involve

H-atoms from the methyl groups of the carboxylate ligand and H atoms belonging to different ethyl groups of two Et-sao$^{2-}$ ligands: one contact, between H911 and H92, goes from 2.38 to 1.50 Å and the other, between H83 and H832, goes from 2.71 to 2.14 Å.

The intra-molecular structural changes are far more dramatic: the Mn-N-O-Mn torsion angles change considerably, becoming less puckered (Figure 3). The angle between Mn1-Mn3 decreases from 34.8(2)° to 29.7(11)° (a change of 4.3°), that between Mn2-Mn3 changes from 39.1(2)° to 34.6(11)°, and that between Mn1-Mn2 changes from 43.0(2)° to 42.2(10)°. The largest changes involve Mn3, probably due
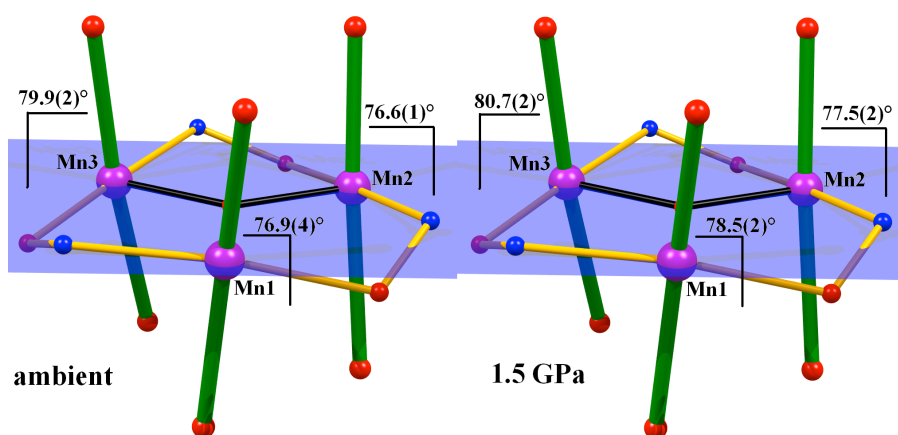


**Figure 4** Comparison of the Jahn–Teller alignments in **1** at ambient condition and at 1.5 GPa. Colour code: Mn = purple, O = red, N = blue, JT axes = green bonds.

**Table 3** Comparison of the bond lengths (Å) of the Jahn–Teller axes as function of pressure for complex **1**.

| P (GPa) | Mn1 – O2 | Mn1 – O92 | Mn2 – O15 |
|---------|----------|-----------|-----------|
| 0 | 2.132(3) | 2.434(3) | 2.196(3) |
| 0.5 | 2.131(4) | 2.414(3) | 2.180(4) |
| 1.0 | 2.107(4) | 2.375(7) | 2.178(4) |
| 1.5 | 2.093(5) | 2.359(5) | 2.151(6) |
| Δ/σ | 6.7 | 12.8 | 6.7 |
| **P (GPa)** | **Mn2 – O11** | **Mn3 – O14** | **Mn3 – O124** |
| 0 | 2.480(3) | 2.242(3) | 2.333(3) |
| 0.5 | 2.463(5) | 2.284(4) | 2.347(5) |
| 1.0 | 2.465(5) | 2.280(4) | 2.314(5) |
| 1.5 | 2.423(7) | 2.275(6) | 2.320(7) |
| Δ/σ | 7.5 | 4.9 | 1.7 |

to the fact that this metal centre is at the "periphery" of the molecule (Figure 1), is less rigidly held in position and is the only one bonded to two solvent molecules, which sit on its Jahn-Teller axes. It is therefore more able to distort helping to release

the structural tension caused by the pressure-induced compression. Mn1 and Mn2 are in more "rigid" positions, the oxime moiety that holds them together also bridging the two triangular units together, *i.e.* the oximic O-atom (O92) is μ-bridging rather than terminal (O91, O93). The torsion angle between Mn1 and Mn3 (and symmetry equivalent) is worthy of particular attention because it falls below the value previously reported (~31º) for being responsible for the switch in the pairwise exchange interaction between the two metals from ferromagnetic to antiferromagnetic.[69-73]

The changes in the Jahn-Teller axes (JT) with pressure are rather curious (Figure 3, Table 3): while Mn1 and Mn2 are compressed (2.132(3), 2.434(3) Å to 2.093(5), 2.359(5) Å for the former and 2.196(3), 2.480(3) Å to 2.151(6), 2.423(7) Å for the latter) Mn3 actually elongates at 0.5 GPa (2.242(3) to 2.284(4) Å and from 2.333(3) to 2.347(5) Å) and then constantly compresses resulting in a slight overall compression of the bond with O124 (2.320(7) Å), and to an elongation of the bond with O14 (2.275(6) Å). Another important variation in the structure is the angle that the JT axes form with respect to the plane of the [Mn$_3$] triangle, all becoming more perpendicular with increased pressure: that involving Mn1 goes from 76.9(4)° to 78.5(2)°, that involving Mn2 from 76.6(1)° to 77.5(2)° and that involving Mn3 from 79.9(2)° to 80.7(2)° at 1.5 GPa.

Although they do not appear to change with the application of pressure, some intra-molecular H-bonds are present in the structure involving the H atoms belonging to the solvent molecules coordinated to Mn3 and Mn2. H14 and H15 are directed towards O1, the uncoordinated oxygen atom that belongs to the carboxylate. H124, from the second ethanol molecule attached to Mn3, is directed in the opposite direction from the other two and is H-bonded to the phenolic O-atom from the ligand bridging Mn1 and Mn3 (plus symmetry equivalent).

## Effect of Pressure on 2

Similar observations to those seen for **1** generally hold true for **2**. Compression of the unit cell (Table 1) is present but mostly along the crystallographic *a* axis. There are no strong intermolecular interactions, H-bonds or π-π stacking, therefore the compression of the cell is likely due to the reduction of voids between the molecules

in the lattice. The application of pressure leads to some short inter-molecular H-H contacts: in particular the shortest contact occurs between H341 from the carboxylate



**Figure 5** Comparison of the Jahn–Teller bond lengths and torsion angles in **2** at ambient conditions and at 1.5 GPa. Colour code: Mn = purple, O = red, N = blue, JT axes = green bonds.

**Table 4** Comparison of the amplitude of the Mn-O-N-Mn torsion angles (°) as function of pressure for complex **2**.

| P (GPa) | Mn1-O-N-Mn2 | Mn2-O-N-Mn3 | Mn3-O-N-Mn1 |
|---|---|---|---|
| **0** | 41.1(2) ° | 40.5(2) ° | 33.2(2) ° |
| **0.5** | 40.2(9) ° | 38.6(8) ° | 31.0(8) ° |
| **1.5** | 41.1(17) ° | 36.5(18) ° | 27.5(17) ° |
| **Δ/σ** | 0.00 | 2.21 | 3.38 |

ligand and its equivalent in the neighbouring molecule, which goes from 2.14 Å to 2.07 Å. As far as intra-molecular structural changes are concerned, the Mn-N-O-Mn torsion angles hint at an analogous effect to that seen in **1**, but the changes observed are not statistically significant at the level of precision of the structure determination (Figure 5, Table 4). The angle between Mn1-Mn3 decreases from 33.2(2)º to 27.5(17)º (a change of 3.38º), for Mn2-Mn3 it decreases from 40.5(2)º to 36.5(18)º, while that between Mn1-Mn2 stays essentially unchanged at ~41.1º. As for **1**, Mn3 is the one most affected by pressure and there is one torsion angle that falls below the value previously reported (~31º) for being responsible for the switch in the pairwise exchange interaction between the two metals from ferromagnetic to antiferromagnetic.[69-73] The Jahn-Teller axes (JT) are all compressed (Figure 5, Table 5): Mn1, 2.102(3), 2.508(3) Å to 2.033(7), 2.486(9) Å; Mn2, 2.205(3), 2.397(3) Å to 2.141(9), 2.387(11) Å; Mn3, 2.395(3), 2.188(3) Å to 2.398(7), 2.107(7) Å.
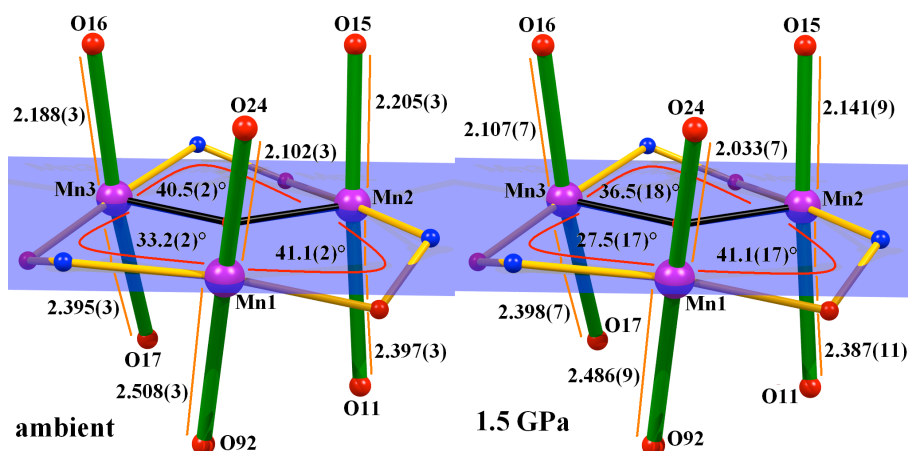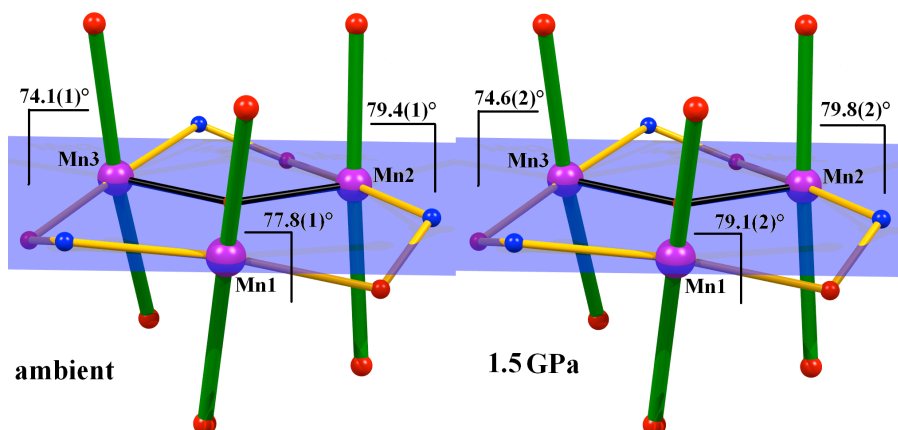
**Figure 6** Comparison of the Jahn–Teller alignments in **2** at ambient condition and at 1.5 GPa. Colour code: Mn = purple, O = red, N = blue, JT axes = green bonds.

**Table 5** Comparison of the bond lengths (Å) of the Jahn–Teller axes as function of pressure for complex **2**.

| P (GPa) | Mn1 – O24 | Mn1 – O92 | Mn2 – O15 |
|---|---|---|---|
| **0** | 2.102(3) | 2.508(3) | 2.205(3) |
| **0.5** | 2.102(3) | 2.501(4) | 2.215(5) |
| **1.5** | 2.033(7) | 2.486(9) | 2.141(9) |
| **Δ/σ** | 9.0 | 2.3 | 6.7 |
| P (GPa) | Mn2 – O11 | Mn3 – O17 | Mn3 – O16 |
| **0** | 2.397(3) | 2.395(3) | 2.188(3) |
| **0.5** | 2.388(5) | 2.388(3) | 2.191(3) |
| **1.5** | 2.387(11) | 2.398(7) | 2.107(7) |
| **Δ/σ** | 0.8 | 0.4 | 10.6 |

Variations in the alignment of the JT axes are within the statistical error on the measurements (Figure 6), though the trend appears analogous to that seen for **1**.

## 2.2.3 Magnetochemistry

### DC magnetic susceptibility and magnetisation measurements on 1

Variable temperature magnetic susceptibility data were collected on **1** in the temperature range 300-5 K in an applied field of 1 kG (Figure 8) at ambient and four different pressures. The magnetic behaviour of **1** at ambient pressure has been described in detail previously[69-73]; simulation of the susceptibility data using the Hamiltonian in Eqn 1 and the coupling scheme of Figure 7a affording the parameters $S = 12$, $g = 1.99$, and $J = 1.75$ cm$^{-1}$; while a fit of the magnetisation data (Figure 9) with an axial ZFS plus Zeeman Hamiltonian[81]

$$\hat{H} = D\left[\hat{S}_Z^2 - S(S+1)/3\right] + \mu_B gH\hat{S} \qquad (1)$$

over the whole field and temperature range afforded the parameters: $S = 12$, $D = -0.38$ cm$^{-1}$.

$$\hat{H} = -2J(\hat{S}_1\cdot\hat{S}_2+\hat{S}_2\cdot\hat{S}_3+\hat{S}_1\cdot\hat{S}_3+\hat{S}_{1'}\cdot\hat{S}_{2'}+\hat{S}_{2'}\cdot\hat{S}_{3'}+\hat{S}_{1'}\cdot\hat{S}_{3'}+\hat{S}_1\cdot\hat{S}_{2'}+\hat{S}_1\cdot\hat{S}_{1'}+\hat{S}_2\cdot\hat{S}_{1'}) \qquad (2)$$

$$\hat{H} = -2J_1(\hat{S}_1\cdot\hat{S}_2+\hat{S}_2\cdot\hat{S}_3+\hat{S}_{1'}\cdot\hat{S}_{2'}+\hat{S}_{2'}\cdot\hat{S}_{3'}+\hat{S}_1\cdot\hat{S}_{1'}+\hat{S}_1\cdot\hat{S}_{2'}+\hat{S}_2\cdot\hat{S}_{1'})-2J_2(\hat{S}_1\cdot\hat{S}_3+\hat{S}_{1'}\cdot\hat{S}_{3'}) \qquad (3)$$

Under pressure the room temperature $\chi_M T$ value of approximately 20 cm$^3$ K mol$^{-1}$
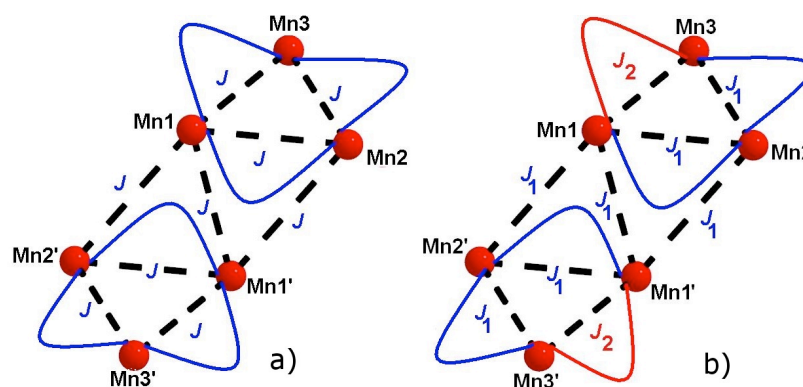


**Figure 7** Cartoon illustrating the scheme of interactions used simulate the $\chi_m T$ vs T data for **1** using a 1$J$ model (a) as defined in Eqn 2 and a 2$J$ model (b) as defined in Eqn 3.

remains almost unchanged at all pressures (Figure 8). As temperature is decreased the value remains relatively constant until ~120 K, below which $\chi_M T$ begins to increase following different paths as a function of the applied pressure to a maximum value at approximately 9 K. The intensities of these peaks are 71 cm$^3$ K mol$^{-1}$ at 0.75 GPa, 68 cm$^3$ K mol$^{-1}$ at 1.1 GPa, 63 cm$^3$ K mol$^{-1}$ at 1.5 GPa and 58 cm$^3$ K mol$^{-1}$ at 1.75 GPa. Below 9 K the value of $\chi_M T$ drops sharply in all cases. This trend is a clear indication that the ferromagnetic interactions between the manganese ions are being weakened by the application of pressure, consistent with the crystallographic observations that the Mn1-N-O-Mn3 and Mn2-O-N-Mn3 torsion angles become flatter with pressure. In particular the Mn1-Mn3 torsion angle at 1.5 GPa reaches a value of 29.7°, below the proposed F→AF "switching point" of 31° suggesting that an antiferromagnetic interaction should be introduced to our model to explain the high pressure magnetic data. Although the background of the pressure cell used in our experiment does not allow us to analyse the data in a rigorously quantitative manner it is still possible to interpret the trends in a qualitative fashion to extract

some important conclusions. Indeed it is important to point out that the pressure changes with changing temperature (we expect a change of the order of ~0.25 GPa between 300 and 5 K). In addition, when performing high pressure measurements we often observe a small discontinuity at ca. 225 K which is associated with the freezing of the oil and the consequent sudden drop in the pressure inside the cell.[55, 56] Up to 1.1 GPa the data can be successfully simulated using the same scheme of ferromagnetic-only interactions[82] pictured in Figure 7a and defined in Eqn 2.
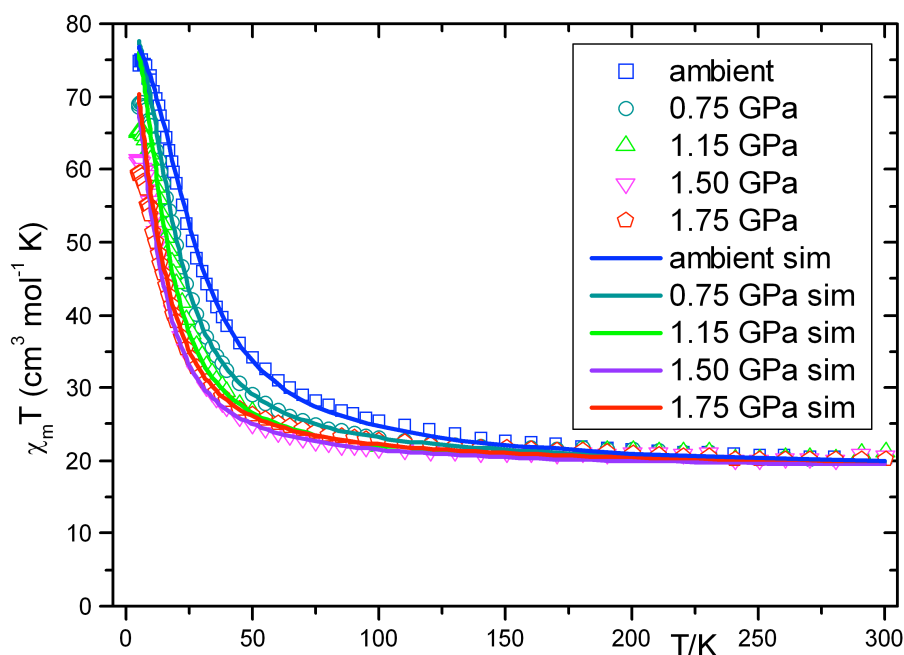


**Figure 8** Plots of $\chi_M T$ versus T for **1** recorded in the 300-5 K temperature range at the indicated pressures; the solid lines represent simulations of the data. The simulation at ambient pressure gives $J = 1.75$ cm$^{-1}$ with $S = 12$ using Eqn 2 and Figure 7a, whereas at 1.75 GPa $J_1 = 1.33$ cm$^{-1}$ and $J_2 = -0.45$ cm$^{-1}$ with $S = 11$ using Eqn 3 and Figure 7b.

**Table 6** Comparison of the $J$ values and the energy differences ($E_1$, $E_2$) between the ground spin state and first ($S_1$) /second ($S_2$) excited spin states as function of pressure for complex **1**.

| P (GPa) | S | J/cm$^{-1}$ | E$_1$/cm$^{-1}$ (S$_1$) | E$_2$/cm$^{-1}$ (S$_2$) |
|---------|---|-------------|--------------------------|--------------------------|
| 0 | 12 | 1.75 | 8.3 (S=11) | 16.8 (S=10) |
| 0.75 | 12 | 1.45 | 6.9 (S=11) | 14.5 (S=10) |
| 1.15 | 12 | 1.20 | 5.7 (S=11) | 11.5 (S=10) |
| 1.50 | 11 | 1.10/-0.10 | 2.4 (S=12) | 3.8 (S=10) |
| 1.75 | 11 | 1.00/-0.45 | 1.5 (S=10) | 2.98 (S=12) |

However it proved impossible to simulate the 1.5 and 1.75 GPa data using this model, and required introduction of a 2$J$-model (Figure 7b, Eqn 3) employing an antiferromagnetic interaction between Mn1-Mn3. This affords $S = 11$, $J_1 = 1.10$ cm$^{-1}$,

$J_2$ = -0.10 cm$^{-1}$ (1.5 GPa) and $S$ = 11, $J_1$ = 1.00 cm$^{-1}$, $J_2$ = -0.45 cm$^{-1}$ (1.75 GPa) (Table 6).
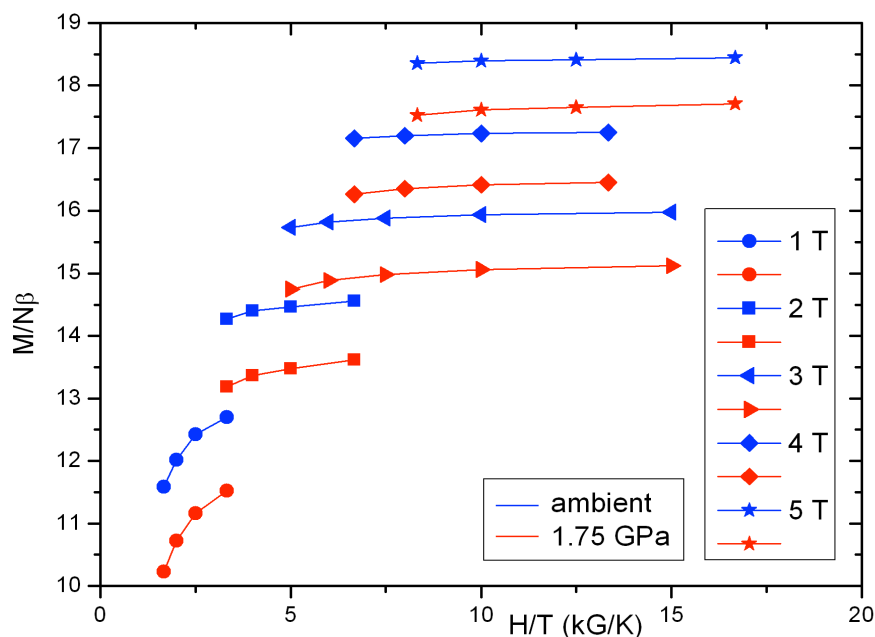


**Figure 9** Plots of M/Nβ versus H/T for **1** recorded in the 2-7 K temperature range at the indicated pressure and field values.

**Table 7** Comparison of the *D* values and spin states as a function of pressure for **1**.

| P (GPa) | *D*/ cm$^{-1}$ | *S* |
|---------|---------|-----|
| **0** | -0.38 | 12 |
| **0.75** | -0.36 | 12 |
| **1.15** | -0.38 | 12 |
| **1.50** | -0.32 | 11 |
| **1.75** | -0.34 | 11 |

The simulations thus suggest the spin ground state of the complex remains $S$ = 12 at lower pressures, but switches to $S$ = 11 in the last two data sets (Table 6). This *qualitative* interpretation must however be tempered by the fact there is likely a plethora of essentially degenerate spin states leading to a breakdown of the simplistic giant spin model.[83] The consequence of the weaker magnetic exchange between the Mn centres induced by the application of pressure is a further nesting of excited states upon the "ground state" (Table 6). At ambient pressure, for example, the $S$ = 11 state is 8.3 cm$^{-1}$ from the ground while the $S$ = 10 state is 16.8 cm$^{-1}$ higher in energy. At 1.75 GPa we find a different ground state ($S$ = 11) with $S$ = 10 and $S$ = 12 states only 1.5 cm$^{-1}$ and 2.98 cm$^{-1}$ higher in energy, respectively (Table 6). The role

of the excited states is clearly very important for this family of molecules.[83] For example under ambient conditions the complex [$Mn^{III}_6O_2$(Et-sao)$_6$($O_2$CPh)$_2$(EtOH)$_4$($H_2O$)$_2$] (**10**) displays an effective energy barrier of ~53 K – approximately 36 K below its theoretical upper limit.[69-73, 83] Single-crystal hysteresis loop and relaxation measurements in combination with detailed INS and FDMRS studies[83] suggest that excited states nested upon the ground state play a crucial role in determining the magnetic relaxation process since tunneling pathways also involve states of different total spin. Indeed this is nicely demonstrated in the comparison of the (ambient) magnetic analysis of **10** with **1** where an increase in the structural distortion leads to an increase in $J$ and an increase in $U_{eff}$,[71,75,79] manifested as an increase in the temperature at which both out-of-phase ac susceptibility signals and dc hysteresis is observed. What we can clearly conclude from the data is that the application of pressure weakens the ferromagnetic exchange.

Magnetisation data for complex **1** were collected in the ranges 10 – 50 kG, 2 – 7 K and 0-1.75 GPa. These are plotted as reduced magnetisation ($M/N\beta$) vs $H/T$ in Figure 9. Fitting of the experimental data with an axial ZFS plus Zeeman Hamiltonian,[81] reported in Eqn (1), suggests that the ground state does indeed change to $S = 11$ ($g = 1.98$) with a small decrease in $|D|$ with pressure to a value of $D = -0.34$ cm$^{-1}$ at 1.75 GPa, (Table 7).

## DC magnetic susceptibility and magnetisation measurements on 2

Analogous dc measurements have been carried out on compound **2** at three different pressures up to 1.4 GPa. The magnetic behaviour of **2** at ambient conditions has been described in detail previously.[74] Simulations of the susceptibility data using the Hamiltonian pictured in Figure 7 and defined in Eqn. 2 afforded the parameters $S = 12$, $g = 2.03$ and $J = 1.31$ cm$^{-1}$; while a fitting of the magnetisation data,[81] using the Hamiltonian in Eqn. 1, over the whole field and temperature range afforded the parameteres: $S = 12$, $D = -0.33$ cm$^{-1}$. Under pressure the room temperature $\chi_M T$ value of approximately 20 cm$^3$ K mol$^{-1}$ remains almost unchanged at all pressures (Figure 10). As the temperature is decreased the value remains relatively constant until around 120 K, below which $\chi_M T$ begins to increase following different paths as a function of applied pressure to a maximum value at approximately 10 K. The

intensities of these peaks are 54 cm$^3$ mol$^{-1}$ at 0.44 GPa, 37 cm$^3$ mol$^{-1}$ at 0.7 GPa and 34 cm$^3$ mol$^{-1}$ at 1.4 GPa. Below 9 K the value of $\chi_M T$ drops in all cases. This trend is again a clear indication that the ferromagnetic interactions between the manganese ions are being weakened by the application of pressure, consistent with the
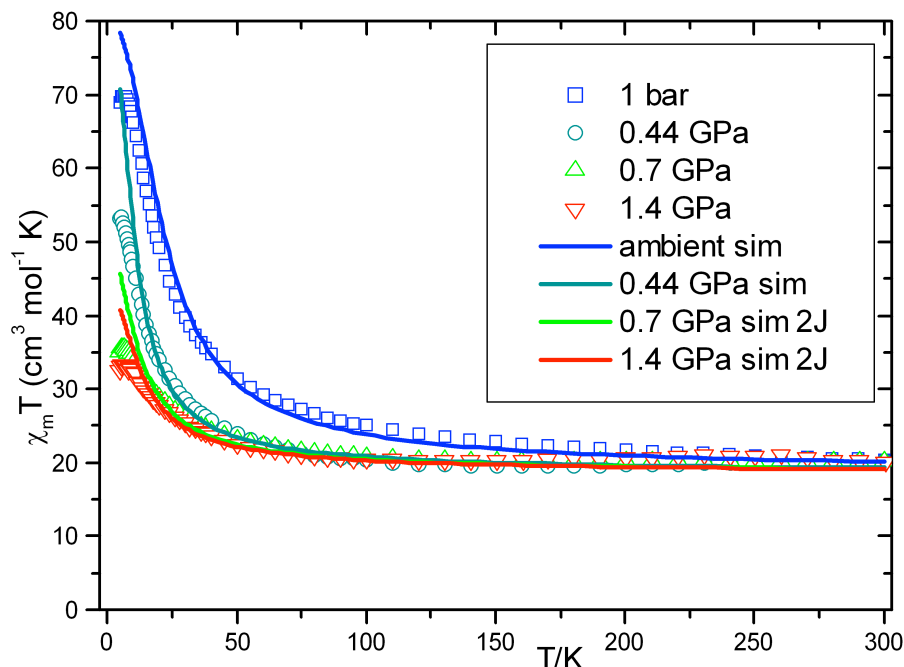


**Figure 10** Plots of $\chi_M T$ versus T for **2** recorded in the 300-5 K temperature range at the indicated pressures; the solid lines represent simulations of the data. The simulation at ambient pressure gives $J = 1.31$ cm$^{-1}$ with $S = 12$ using Eqn 2 and Figure 7a whereas at 1.4 GPa $J_1 = 0.88$ cm$^{-1}$ and $J_2 = -0.70$ cm$^{-1}$ with $S = 10$ using Eqn 3 and Figure 7b.

**Table 8** Comparison of the $J$ values and the energy ($E_1$, $E_2$) between the ground spin state and first ($S_1$) /second ($S_2$) excited spin states as function of pressure for complex **2**.

| P (GPa) | S | J/cm$^{-1}$ | E$_1$/cm$^{-1}$(S$_1$) | E$_2$/cm$^{-1}$ (S$_2$) |
|---------|---|-------------|------------------------|-------------------------|
| **ambient** | 12 | 1.31 | 8.3 (S=11) | 16.8 (S=10) |
| **0.44** | 12 | 0.66 | 3 (S=11) | 6 (S=10) |
| **0.7** | 10 | 0.8/-0.6 | 1.2 (S=11) | 2.7 (S=9) |
| **1.40** | 10 | 0.76/-0.70 | 1.8 (S=11) | 3.2 (S=9) |

**Table 9** Comparison of the $D$ values and the energy differences between the spin states as a function of pressure for complex **2**.

| P (GPa) | D/ cm$^{-1}$ | S |
|---------|--------------|---|
| **ambient** | -0.33 | 12 |
| **0.44** | -0.33 | 12 |
| **0.7** | -0.30 | 10 |
| **1.4** | -0.33 | 10 |

crystallographic observations that the Mn-N-O-Mn torsion angles become flatter

with pressure. In particular the Mn1-Mn3 torsion angle at 1.4 GPa reaches a value of 27.5°, below the suggested F→AF "switching point" of 31° suggesting that an antiferromagnetic interaction should be required in our high pressure model. The data have been simulated using the Hamiltonians and models pictured in Figures 7a and 7b and defined in Eqns 2 and 3. Compound **2** seems somewhat more sensitive to pressure than **1**. At 0.4 GPa the data can be successfully simulated using the same scheme of ferromagnetic-only interactions but with a very weak *J* value (Table 8). At
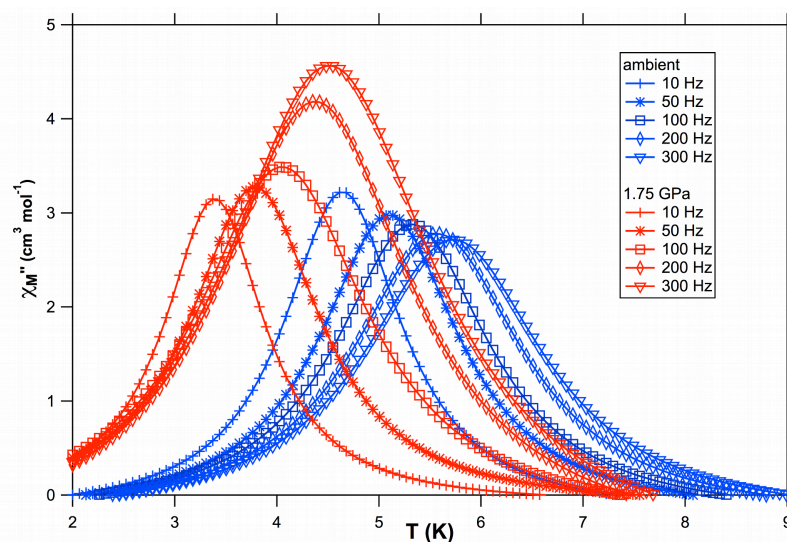


**Figure 11** Plots of $\chi''_M$ versus T for **1** recorded in the 2-10 K temperature range at the indicated pressures and frequencies.

higher pressures it proved impossible to simulate the 0.7 and 1.4 GPa data using this model, and required introduction of a 2*J*-model (Figure 7b, Eqn 3) employing an antiferromagnetic interaction between Mn1-Mn3. This affords $S = 10$, $J_1 = 0.8$ cm$^{-1}$, $J_2 = -0.6$ cm$^{-1}$ and $S = 10$, $J_1 = 0.76$ cm$^{-1}$, $J_2 = -0.7$ cm$^{-1}$ respectively (Table 8). Magnetisation data for complex **2** were collected on the 2-7 K and 0 - 7 T temperature and field ranges, but we have been unable to satisfactorily fit the data using the simple model above suggesting the presence of a number of different *S* states with similar energies.

## Ac magnetic susceptibility and hysteresis loop measurements for 1 and 2

Ac susceptibility studies were carried out in the 2 – 10 K range in a 4 G field oscillating at frequencies up to 300 Hz. The out-of-phase ($\chi_M^{//}$) ac signals for **1** as a function of pressure are shown in Figure 11.



**Figure 12** Arrhenius plots based on out-of-phase ac susceptibility measurements of **1** at different pressures.
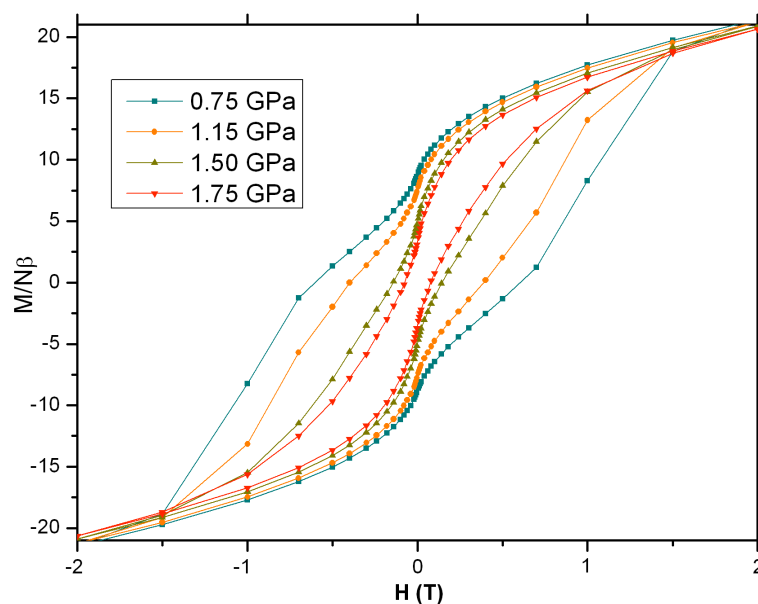


**Figure 13** Hysteresis loops for **1** recorded at the indicated pressures at 2 K.

There is a clear pressure and frequency-dependent decrease in the $\chi_M''$ peak position from T $\leq$ 6 K. For complex **1** the peak at 300 Hz at ambient pressure occurs at approximately 6.2 K whereas the same frequency curve at 1.75 GPa displays a peak at ~4.8 K. For complex **2** the peak at 100 Hz moves from 3.9 K to ~3 K at the 1.4 GPa. The high pressure data obtained were fit to the Arrhenius equation (Eqn 4) and are plotted in Figures 12, 14.

$$\tau(T) = \tau_0 \cdot \exp\left(\frac{U}{T \cdot k_B}\right) \qquad (4)$$

These show a clear reduction in the effective barrier for magnetisation reversal from ~83 K to ~45 K for **1** at the highest pressure studied, representing an almost two-fold reduction, compatible with a change in the spin ground state and/or increased nesting of excited states onto the ground state consistent with the presence of weaker pairwise exchange. The same effect is observed for **2** with the $U_{eff}$ that goes from ~63 K to ~46 K. This is also manifested in the change in the appearance of the hysteresis loops (Figures 13 and 15) that show a clear reduction in coercivity with increased pressure.

## Density functional theory calculations

In order to calculate zero field splitting (ZFS) parameters one has to include (besides dipole spin-spin interactions) spin-orbit effects very accurately.[81] The spin-orbit contribution to the ZFS has been discussed in terms of a general many-electron theory,[82,83] which has been recently reinvestigated in a linear response theory framework.[84] At the moment it appears that the combination of methods based on density functional theory (DFT) together with a spin-orbit approach is a practical way to handle large polynuclear metal complexes. Pederson and coworkers have implemented the spin-orbit effect using a perturbative approach in the all-electron code NRMOL,[19, 20, 84-98] which has successfully been used to estimate the ZFS parameters $D$ and $E$ for large polynuclear metal complexes, including several SMMs.[87-94]

While there is surprisingly good agreement in several cases, for monomers in particular there is considerable underestimation of the $D$ parameter[99]. Recently, Neese has reported that the underestimation of zero field splitting parameters is basically due to an intrinsic inaccuracy of the Generalized Gradient Approximation

(GGA) functionals, because a minimum number of approximations have been
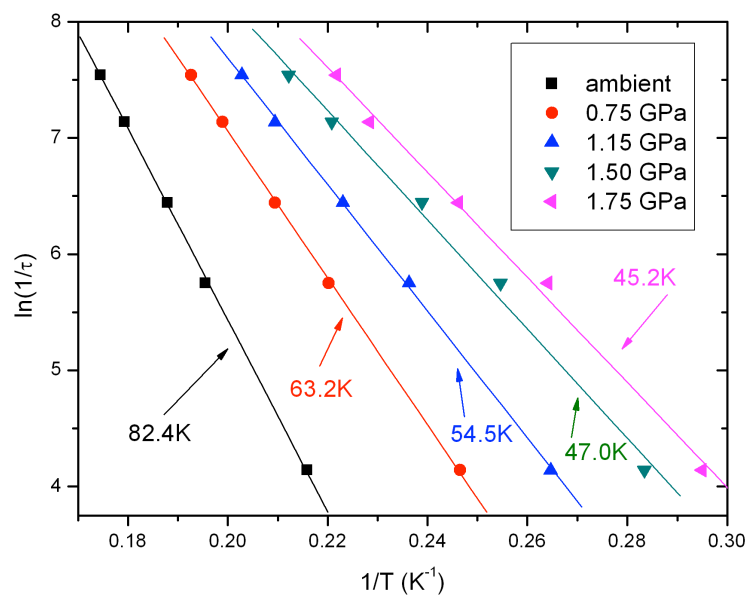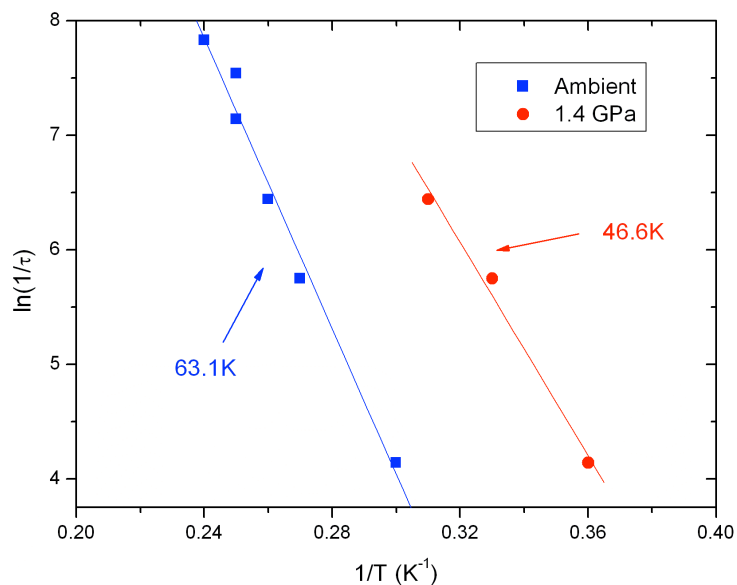


**Figure 14**  Arrhenius plots based on out-of-phase ac susceptibility measurements of **2** at different pressures.
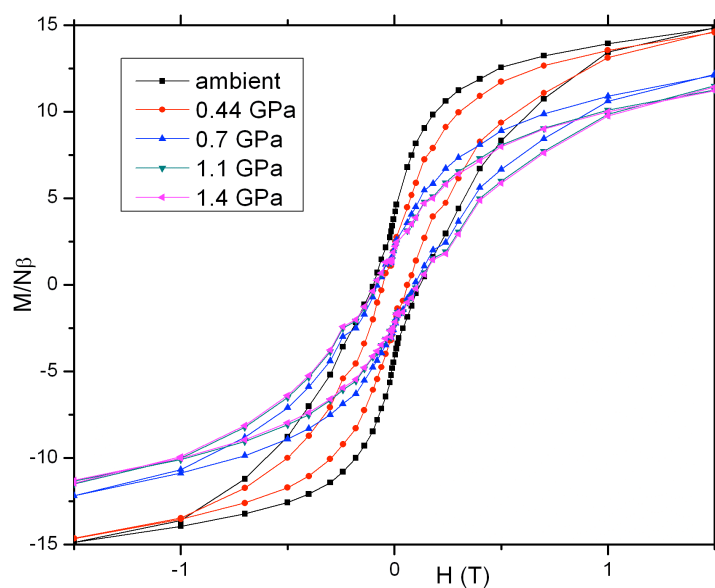


**Figure 15**  Hysteresis loops for **2** recorded at the indicated pressures at 2 K.

included in the treatment of the spin-orbit and spin-spin coupling.[100] However, results for very simple molecules show that the use of a hybrid functional does not significantly improve the GGA results.[99] A similar conclusion was reached in a recent paper that compared different approaches for a series of $Mn^{II}$ complexes.[98]

Here it is reported DFT results on the pressure dependent $D$ for complex **1** using the NRLMOL code with the PBE exchange-correlation functional.[101] The geometries of a single molecule as a function of pressure have been generated directly from the crystallography data reported here. The basis set for the 228 atom molecule included 6318 basis functions built from contracted atomic like orbitals and long-range Gaussians. The results show only small dependence on the exchange-correlation functional or basis set quality.[95]

The lowest energy state found by DFT was in all cases a ferromagnetically coupled ground state with $S = 12$. Interestingly, the tendency of increased antiferromagnetic coupling has also been noted in the DFT calculation. During the self-consistent calculation all electronic degrees of freedom were allowed to relax. For the low pressure cases all calculations converged to a ferromagnetic state with $S = 12$ without any problem. In the 1.5 GPa case we also obtained a self-consistent solution corresponding to $S = 10$, although higher in energy compared with the $S = 12$ state.

The mixing of states with different multiplicities to the ground state poses a great problem to all single determinant approaches like DFT. This will also strongly impact the accuracy of the ZFS values. The absolute values of $D$ are often underestimated by about 50%, which can be related to a failure of the method itself.[99, 102, 103]

Even though there is no quantitative agreement between experiment and current DFT based methods there is still hope to reproduce experimental trends in a qualitative manner. For the lower pressures with spin state $S = 12$ we obtain an approximately constant negative value of $D = -0.25$ cm$^{-1}$. For higher pressures the calculations predict a small increase of the absolute value of $D$ to a value of -0.27 cm$^{-1}$ at 1.5 GPa, assuming the complex keeps the $S = 12$ spin ground state. The calculation of the ZFS corresponding to the $S = 10$ solution showed a tendency for an easy plane anisotropy (positive $D$). This may suggest a lowering of the $D$ value with decreasing $S$. Unfortunately, it was not possible to stabilize a solution with $S = 11$ in our DFT calculations. Even though the results should be taken only very carefully, it appears that the low pressure behavior of the ZFS is qualitatively correctly reproduced by these theoretical calculations supporting the experimental observation.

**Conclusions**

The first part of this chapter presented the first combined high pressure magnetic and single-crystal crystallographic study of two polymetallic single-molecule magnets of the "$Mn_6$" family allowing us to qualitatively correlate changes in molecular structure with changes in magnetic behaviour. The application of hydrostatic pressure up to 1.5 GPa flattens the Mn-N-O-Mn torsion angles weakening the magnetic exchange between the metals. The JT axes change in both their relative compressions and their alignment with respect to the $Mn_3$ planes. The crystallographic data are in good agreement with the experimental high pressure magnetic measurements. The $\chi_M T$ data displays a gradual lowering in the low temperature peak height and slope, indicating weaker exchange with increasing pressure and excited states at much lower energy. In both cases simulations suggest that one interaction is switched from ferro- to antiferromagnetic at high pressure, in agreements with fits of the magnetisation data. Ac out-of-phase ($\chi_M{}^{//}$) susceptibility data and hysteresis loop measurements demonstrate a dramatic decrease in the energy barrier for magnetisation reversal in both cases. These overall findings are consistent with weakened exchange interactions leading to increased nesting of excited states upon the ground state, and even a possible change in the ground state spin value. While some of our previous papers have demonstrated that "internal" chemical modification of the magnetic cores of these molecules can control $J$ and thus $U_{eff}$, the present paper demonstrates that the same phenomenon can be observed by applying "external" hydrostatic pressure.

# 2.3 High pressure effects on a trimetallic $Mn^{II/III}$ SMM

## *2.3.1 Experimental section*

**Syntheses**

All reactions were carried out in aerobic conditions using materials as received with no further purifications. [$Mn_3$(Hcht)$_2$(bpy)$_4$](ClO$_4$)$_3$·Et$_2$O·2MeCN (**3**·Et$_2$O·2MeCN) was made as previously described.[75, 76]

**X-ray crystallography**

High-pressure single crystal experiments were carried out using a Merrill-Bassett[34] diamond anvil cell (half-opening angle 40°), equipped with Boehler-Almax diamonds with 600 µm culets and a tungsten gasket.[77] Petroleum ether was used as hydrostatic medium and a small ruby chip was loaded into the cell as the pressure calibrant with the ruby fluorescence used to measure the pressure.[78] Diffraction data were collected using synchrotron radiation of wavelength $\lambda$ = 0.4767 Å at room temperature on a Bruker Smart APEX II diffractometer[35, 79] on Station 9.8 at SRS,

**Table 10** Crystallographic Data for Complex **3** at 0.16, 0.57 and 12.5 GPa

| | $3 - [Mn_3(Hcht)_2(bpy)_4](ClO_4)_3$ | | |
|---|---|---|---|
| **Crystal data** | **0.16 GPa** | **0.57 GPa** | **1.25 GPa** |
| Space group | *I2/m* | *I2/m* | *I2/m* |
| Temperature (K) | 300 | 300 | 300 |
| *a, b, c* (Å) | 11.897 (2), 22.067 (4), 13.312 (3) | 11.549 (2), 21.720 (4), 12.991 (3) | 11.331 (2), 21.547 (4), 12.817 (3) |
| $\beta$ (°) | 93.82 (3) | 94.04 (3) | 93.67 (3) |
| *V* (Å$^3$) | 3487.0 (12) | 3250.7 (11) | 3122.9 (11) |
| Radiation type | Synchrotron | Synchrotron | Synchrotron |
| $\mu$ (mm$^{-1}$) | 0.72 | 0.77 | 0.80 |
| $\lambda$ (Å) | 0.4767 | 0.4767 | 0.4767 |
| Crystal size (mm) | 0.11 × 0.10 × 0.08 | 0.11 × 0.10 × 0.08 | 0.11 × 0.10 × 0.08 |
| $T_{min}$/ $T_{max}$ | 0.45 / 0.94 | 0.49 / 0.94 | 0.26 / 0.94 |
| Measured, independent, observed reflections | 8357, 1787, 1011 | 8838, 1985, 1223 | 6315, 1627, 830 |
| Criterion for observed reflections | $I > 2.0\sigma(I)$ | $I > 2.0\sigma(I)$ | $I > 2.0\sigma(I)$ |
| $R_{int}$ | 0.071 | 0.057 | 0.075 |
| $\theta_{max}$ (°) | 15.4 | 16.3 | 15.4 |
| Refinement | *F* | *F* | *F* |
| *R, wR, S* | 0.074, 0.042, 0.98 | 0.067, 0.040, 0.96 | 0.100, 0.052, 1.00 |
| Reflections | 1011 reflections | 1223 reflections | 830 reflections |
| Parameters | 195 | 195 | 77 |
| Restraints | 32 | 31 | 34 |
| $(\Delta/\sigma)_{max}$ | 0.006 | 0.003 | 0.003 |
| $\Delta\rho_{max}, \Delta\rho_{min}$ (eÅ$^{-3}$) | 0.33, −0.30 | 0.41, −0.30 | 0.51, −0.66 |

Daresbury Laboratory. Integrations were carried out using the program SAINT[36] and absorption corrections with the program SADABS[40] and SHADE.[37] Data collections were taken at 0.16, 0.57 and 1.25 GPa. Refinements of the compressed form of **3** were carried out starting from the coordinates obtained from a separate data collection carried out under ambient conditions. The program CRYSTALS[41] was

used to refine the structures against $F$ using all the reflections. Due to the low completeness of the data sets, some restraints on C-C distances have been applied; in the 0.16 and 0.57 GPa all the O atoms of the perchlorates and one of the Cl atoms were refined with isotropic displacement parameters while the remaining atoms with an anisotropic parameter. At 1.25 GPa the quality of the crystal and of the diffraction pattern has considerably worsened therefore all the atoms except for the Mn atoms and one of the Cl atom were refined isotropically and the aromatic rings of the bpy ligands were refined as rigid groups. Unit cells and refinement parameters are reported in Table 10.

**Magnetic measurements**

Variable temperature magnetic susceptibility dc measurements were made on a Quantum Design Magnetic Property Measurements System (SQUID magnetometer) equipped with a 7T magnet operating in the 300-2 K temperature range. Diamagnetic corrections were applied using Pascal's constants. For the high-pressure magnetic measurements a cell of piston-cylinder design was constructed. The body of the pressure cell was made of non-magnetic CrNiAl and BERYLCO-25 alloys with zirconia rods used as pistons. The sample was contained inside a PTFE capsule with Daphne 7373 oil (IDEMITSU-ILS) used as the pressure transmitting medium. Pressure was applied in a hydraulic press and was calibrated by the load. Data were collected at 0.43, 0.56, 0.68 and 0.85 GPa.

## *2.3.2  Results and Discussion*

### Description of Structures

The structure of **3** (Figure 14) contains a linear $[Mn^{III}Mn^{II}_2O_4]^{3+}$ core in a *2/m* symmetry with the central $Mn^{3+}$ centre bound to the peripheral $Mn^{2+}$ ions by four oxygen atoms (O15) provided by the two $Hcht^{2-}$ ligands, positioned one above and one below the trimetallic chain. One protonated oxygen atom (O20) from each ligand completes the octahedral coordination of the $Mn^{3+}$ atom and defines the only Jahn – Teller axis present in the molecule. The $Mn^{III}$-O-$Mn^{II}$ angle is approximately 102° and the coordination of each of the two $Mn^{II}$ ions is completed by two bpy ligands. Charge neutrality is maintained by the presence of three perchlorate anions, with

(under ambient conditions) one molecule of $Et_2O$ and two molecules of $CH_3CN$ per cluster in the crystal lattice.

When viewed along the crystallographic $a$ and $c$ axes (Figure 15) the molecules align
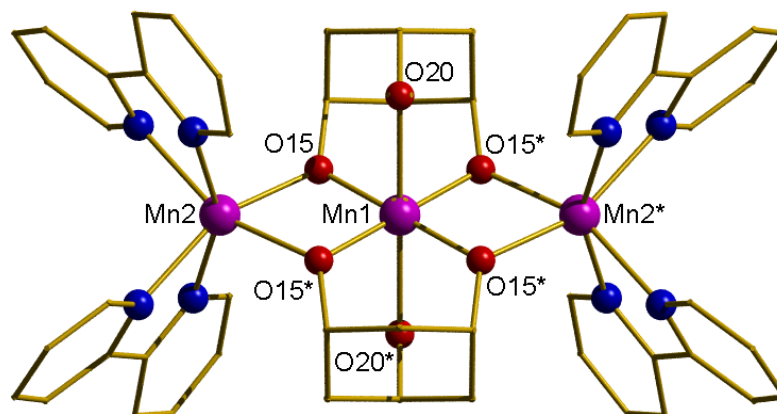


**Figure 14** The molecular structure of complex **3**. Colour scheme: Mn = purple, C = gold, O = red and N = blue. H atoms and counter ions are omitted for clarity.

**Table 11** Bond distances and angles in **3** as a function of pressure.

| P (GPa) | Mn1–Mn2 | Mn1–O20 | Mn1–O15 | Mn2–O15 |
|---|---|---|---|---|
| 0[77,78] | 3.144(1) | 2.330(5) | 1.898(3) | 2.142(3) |
| 0.16 | 3.121(1) | 2.327(9) | 1.889(4) | 2.143(4) |
| 0.57 | 3.119(1) | 2.304(7) | 1.898(3) | 2.126(3) |
| 1.25 | 3.118(1) | 2.315(12) | 1.858(5) | 2.147(5) |
| Δ/σ | 18.3 | 1.0 | 6.8 | 0.8 |

| P (GPa) | Mn1–O15–Mn2 | Mn1–O15–C16 | O15 – O15* | bpy twist |
|---|---|---|---|---|
| 0[77,78] | 102.0(1)° | 122.9(3)° | 2.530(5) | 15.4(1)° |
| 0.16 | 101.2(2)° | 122.6(3)° | 2.546(5) | 13.0(3)° |
| 0.57 | 101.5(1)° | 122.1(3)° | 2.535(4) | 14.7(2)° |
| 1.25 | 102.0(2)° | 125.7(5)° | 2.502(7) | 16.6(2)° |
| Δ/σ | 0 | 4.8 | 3.25 | 5.3 |
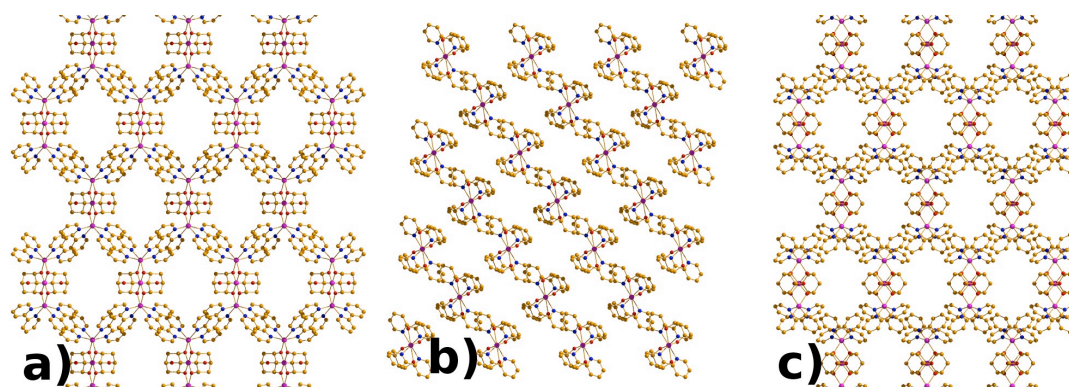


**Figure 15** Packing diagrams of **3** along the three crystallographic axes $a$, $b$ and $c$.

in alternate rows forming an attractive honeycomb-like architecture. Along the $b$ axis

the arrangement is that of a *zig-zag* series of parallel chains of adjacent molecules, (Figure 15). Two thirds of the perchlorate anions occupy the centre of the cavities with the remaining third positioned between the *zig-zag* chains.

## Effect of pressure on 3

The most evident effects caused by the application of pressure are the contraction of the unit cell and the complete elimination of the $Et_2O$ and $CH_3CN$ solvent molecules from the crystal structure. Even in the lowest pressure data set measured, 0.16 GPa, these molecules are no longer present. The absence of significant peaks in the difference map, the squeeze procedure that fails to improve the model together with attempts to force solvents to be present, importing them from the ambient pressure model, causing an increase in $R_1$ and a significant decrease in the overall quality or the refinement of the occupancy of these atoms that tends to zero are all clues that allow us to conclude that the solvent has indeed been expelled out of the crystal. To our knowledge this is the first case reported of pressure-induced solvent elimination from the crystal structure of a molecular cluster. The ejection of the solvent leaves large voids in the crystals of **3** accounting for approximately 9.3% of the total volume at 0.16 GPa. These empty spaces are then progressively reduced with higher pressure reaching approximately 5.5% of the total volume at 1.25 GPa (Figures 16 and 17). Distances between the molecules in the crystal are shortened by roughly 0.5 Å; for example inter-molecular separations between $Mn^{3+}$ ions along the three dimensions shift from 11.897(3), 14.005(3) and 22.067(5) Å at 0.16 GPa to 11.331(3), 13.586(3) and 21.547(4) Å at 1.25 GPa, respectively.

As far as *intra*-molecular interactions are concernced (Table 11), changes in the length of the Jahn–Teller axis (O20–Mn1–O20*) are not statistically significant, whilst the bonds between the central Mn atom and the bridging oxygens (Mn1–O15 and symmetry equivalent) contract from 1.898(3) at ambient pressure to 1.858(5) Å at the highest pressure measured. The Mn2-O15 distance does not change however. The Mn1-O15-Mn2 angle remains "fixed" at a value of *ca.* 102° but the Mn1-Mn2 separation decreases from 3.143(1) Å at room pressure to 3.118(2) Å at 1.25 GPa (Figure 5, Table 2). The planes of the bpy rings become slightly more twisted with

respect to each other changing from 15.4(1)° at ambient pressure to 16.6(2)° at 1.25 GPa. The Mn2–N distances remaining substantially unchanged.
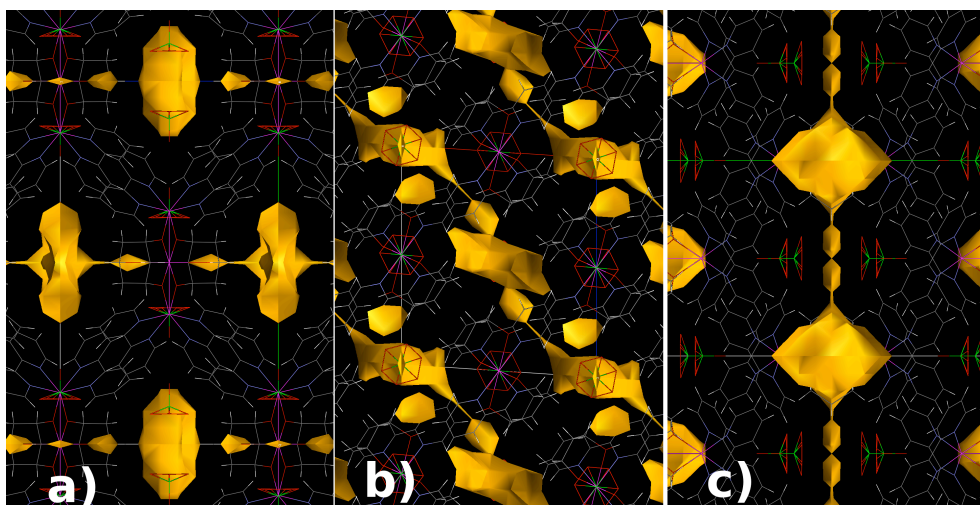


**Figure 16** Voids diagram of **3** along the three crystallographic axes *a*, *b* and *c* at 0.16 GPa – Voids:Volume ratio 9.3% – Pictures drawn with Materials Mercury 2[111].
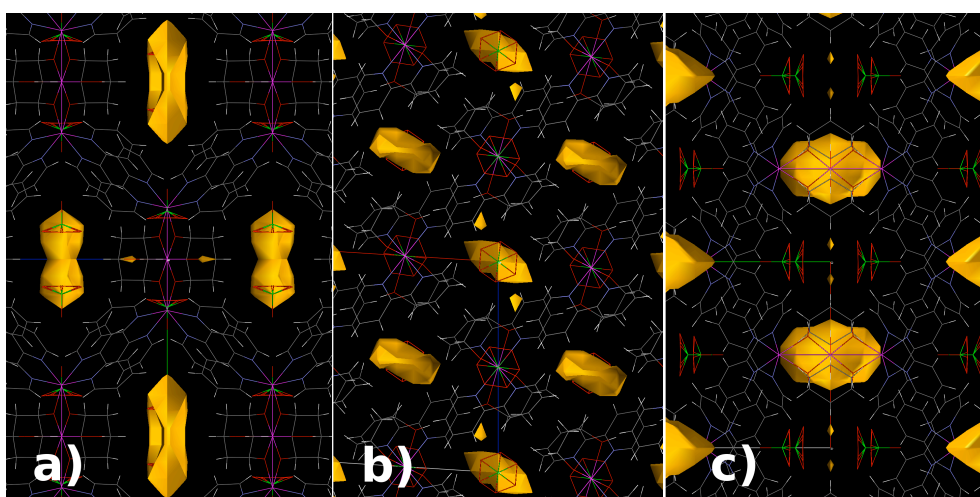


**Figure 17** Voids diagram of **3** along the three crystallographic axes *a*, *b* and *c* at 1.25 GPa – Voids:Volume ratio 5.5% – Pictures drawn with Materials Mercury 2[111].

### 2.3.3 Magnetochemistry

**DC magnetic susceptibility and magnetisation measurements on 3**

Variable temperature magnetic susceptibility data were collected on **3** in the temperature range 300-2 K in an applied field of 1 kG (Figure 18) at ambient and four different pressures. The magnetic behaviour of **3** at ambient pressure has been

described in detail previously.[75, 76] Simulation of the susceptibility data using the Hamiltonian in Eqn (5) and the coupling scheme in Figure 18 afforded the parameters $S = 7$, $g = 2.02$ and $J = 1.15$ cm$^{-1}$.

$$\hat{H} = -2J\left(\hat{S}_1 \cdot \hat{S}_2 + \hat{S}_2 \cdot \hat{S}_{1'}\right) \tag{5}$$

A fit of the magnetisation data, collected between 2 and 7 K and in fields of 1 - 7 T, with the axial ZFS plus Zeeman Hamiltonian of Eqn (1), afforded the parameters $S = 7$, $g = 1.98$ and $D = -0.17$ cm$^{-1}$.[75, 76]
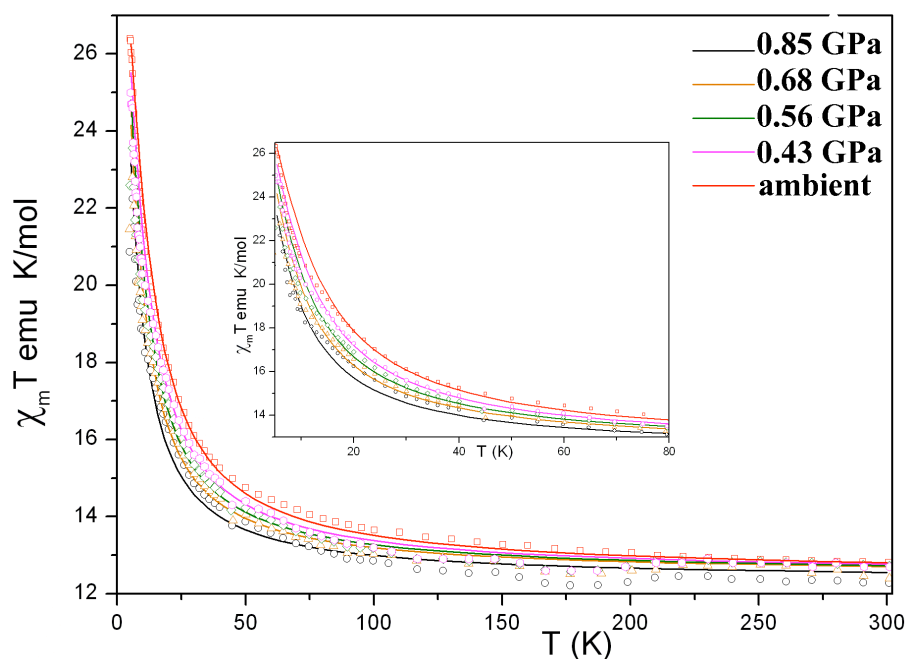


**Figure 18** Plots of $\chi_M T$ versus T for **3** recorded in the 300-2 K temperature range at the indicated pressures; the solid lines represent simulations of the data. The simulation at ambient pressure gives $J = 1.15$ cm$^{-1}$ whereas at 1.25 GPa, $J = 0.60$ cm$^{-1}$.

**Table 12** Comparison of the $J$ values and the energy ($E_1$, $E_2$) between the ground spin state and first ($S_1$) /second ($S_2$) excited spin states as function of pressure for complex **3**.

| P (GPa) | S | J/cm$^{-1}$ | E$_1$/cm$^{-1}$ (S$_1$) | E$_2$/cm$^{-1}$ (S$_2$) |
|---|---|---|---|---|
| ambient[77,78] | 7 | 1.15 | 4.6 (S=6) | 9.2 (S=5) |
| 0.43 | 7 | 0.83 | 3.3 (S=6) | 6.6 (S=5) |
| 0.56 | 7 | 0.74 | 3.0 (S=6) | 6.0 (S=5) |
| 0.68 | 7 | 0.67 | 2.7 (S=6) | 5.4 (S=5) |
| 0.85 | 7 | 0.60 | 2.4 (S=6) | 4.8 (S=5) |

Under pressure the room temperature $\chi_M T$ value of approximately 13 cm$^3$ K mol$^{-1}$ remains almost unchanged at all pressures (Figure 18). As the temperature is decreased the value remains relatively constant until ~100 K, below which $\chi_M T$ begins to increase following different paths as a function of the applied pressure to a

maximum value at approximately 5 K. The intensities of these peaks are 26 cm$^3$ K mol$^{-1}$ at 0.43 GPa and 24 cm$^3$ K mol$^{-1}$ at 0.85 GPa. Below 5 K the value of $\chi_M T$ drops sharply in all cases, most likely due to ZFS effects. This trend is a clear indication that the ferromagnetic interactions between the manganese ions are weakened by the application of hydrostatic pressure. Simulations of the magnetic susceptibility made with the program MAGPACK[82] and the Hamiltonian in Eqn (1) are shown in Table 12. These data help us to qualitatively clarify that the $J$ value constantly decreases from ~1.16 cm$^{-1}$ at ambient pressure to ~0.60 cm$^{-1}$ at 0.85 GPa. The simulations also show that the excited spin states become closer in energy to the ground state as a direct result of the weaker interactions between the metals: $S = 6$ and $S = 5$ move from 4.6 and 9.2 cm$^{-1}$ to 2.4 and 4.8 cm$^{-1}$ respectively from the ground state $S = 7$ (Table 12).

Magnetisation data for **3** were collected in the ranges $1 - 7$ T, $2 - 7$ K and $0 - 0.85$ GPa. At all pressures these data almost perfectly overlap those previously reported for **3** at ambient conditions.[75, 76] The results of the fittings of the experimental data with the axial ZFS plus Zeeman Hamiltonian of Eqn (1) unsurprisingly result in the same parameter set as those obtained at ambient pressure: $S = 7$, $g = 1.98$ and $D = -0.17$ cm$^{-1}$.

### 2.3.4 Discussion

Because of the background of the pressure cell used in our experiment it is not wise to analyse the data in a rigorously quantitative manner, nevertheless it is possible to interpret the trends in a qualitative fashion to extract some conclusions. It is also important to note that the pressure is not constant inside the cell over the whole temperature range because of the different thermal expansions/contractions of the differerent components of the cell: we expect a change of the order of ~0.25 GPa between 300 and 5 K. In addition we often observe a small discontinuity in the signal at *ca.* 225 K which is due to the freezing of the oil and the consequent sudden drop in the pressure inside the cell.[55, 56] The Mn–O–Mn angle and the Jahn–Teller axis are generally unaffected by pressure whilst the planarity of the Mn$^{III}$–O15–Mn$^{II}$–O15* unit is fixed by the molecular symmetry. Significant modifications are observed in the lengths of the Mn$^{III}$–O15 bonds and therefore on the Mn$^{III}$–Mn$^{II}$ separation. This

crystallographic evidence allows us to speculate that the weakening of the magnetic exchange, at least in part, is related to the decrease in metal-metal separation and $Mn^{III}$–O distances. This has already been observed in $Mn^{III}$-salen dimers,[104-106] although here at least one of the Mn-O bonds lies on the Jahn–Teller axis of the metal centre.

## 2.3.5 Conclusions

This part of the chapter presented a study that combines high pressure crystallography and high pressure magnetism in an attempt to correlate structural and magnetic changes in a molecular magnet. The application of hydrostatic pressure on complex **3** up to 1.25 GPa substantially modifies the crystal composition causing **3** to be the first molecular cluster compound to lose lattice solvent molecules through the application of external pressure. In the core of the complex we observe a contraction of the Mn–Mn distance due to a shortening of the $Mn^{III}$-O bond. The $Mn^{III}$–O–$Mn^{II}$

**Table 13** Crystallographic data for complex **4** at 0.2, 0.7, 1.2 and 2.0 GPa.

| Crystal data | 4 – $[(tacn)_6Fe_8O_2(OH)_{12}][ClO_4]_{3.9}Br_{4.1}\cdot 6H_2O$ | | | |
| --- | --- | --- | --- | --- |
| | 0.2 GPa | 0.7 GPa | 1.2 GPa | 2.0 GPa |
| Space group | Monoclinic, $P2_1/c$ | Monoclinic, $P2_1/c$ | Monoclinic, $P2_1/c$ | Monoclinic, $P2_1/c$ |
| Temperature (K) | 300 | 300 | 300 | 300 |
| $a$, | 14.0457 (6), | 13.8528 (11), | 13.687 (3), | 13.574 (3), |
| $b$, | 23.2347 (11), | 22.898 (2), | 22.625 (5), | 22.337 (5), |
| $c$ (Å) | 13.1469 (11) | 13.0124 (17) | 12.860 (3) | 12.840 (3) |
| $\beta$ (°) | 110.924 (5) | 111.477 (9) | 111.95 (3) | 112.66 (3) |
| $V$ (Å$^3$) | 4007.5 (4) | 3841.0 (7) | 3693.7 (15) | 3592.6 (15) |
| Radiation type, | Synchrotron, | Synchrotron, | Synchrotron, | Synchrotron, |
| $\lambda$ (Å) | 0.4869 | 0.4869 | 0.4869 | 0.4869 |
| $\mu$ (mm$^{-1}$) | 3.67 | 3.88 | 4.03 | 4.15 |
| Crystal size (mm) | 0.18 x 0.09 x 0.08 | 0.18 x 0.09 x 0.08 | 0.18 x 0.09 x 0.08 | 0.18 x 0.09 x 0.08 |
| $T_{min}/T_{max}$ | 0.50/0.75 | 0.35/0.73 | 0.29/0.72 | 0.24/0.72 |
| Measured, | 20676, | 14554, | 13117, | 10057, |
| Independent | 4871, | 3654, | 3334, | 2706, |
| observed | 2833 | 2079 | 1821 | 1343 |
| reflections | | | | |
| Criterion for observed reflections | $I > 2.0\sigma(I)$ | $I > 2.0\sigma(I)$ | $I > 2.0\sigma(I)$ | $I > 2.0\sigma(I)$ |
| $R_{int}$ | 0.123 | 0.101 | 0.124 | 0.140 |
| $\theta_{max}$ (°) | 17.7 | 16.3 | 15.7 | 14.7 |
| Refinement on | $F$ | $F$ | $F$ | $F$ |
| $R$, $wR$, $S$ | 0.096, 0.106, 1.10 | 0.092, 0.087, 1.06 | 0.092, 0.098, 1.19 | 0.110, 0.115, 1.20 |
| Reflections | 2833 | 2079 | 1821 | 1343 |
| Parameters | 465 | 465 | 451 | 267 |
| Restraints | 352 | 354 | 337 | 55 |
| $\Delta\rho_{max}$, $\Delta\rho_{min}$ (e Å$^{-3}$) | 2.35, −1.67 | 1.74, −1.14 | 1.02, −1.07 | 1.86, −1.54 |

angle remains essentially unchanged, as does the length of the Jahn–Teller axis. Up to 0.85 GPa the $\chi_M T$ data display a gradual lowering in the low temperature peak heights and slopes indicating a decrease in the strength of the magnetic exchange with increasing pressure. Simulations of the data confirm this, showing an almost two-fold reduction of the coupling constant $J$. As a consequence, the excited spin states move closer in energy to the ground state. These findings allow us to speculate that the exchange, at least in part, is weakened by a reduction in both or either of the $Mn^{III}$-O and $Mn^{III}$-$Mn^{II}$ distances. High pressure magnetisation data in fields of up to 7T are identical to those obtained at ambient pressure. This is in good agreement with the crystallographic evidence that shows a geometrically unchanged Jahn–Teller axis.

## 2.4 High pressure study of a $Fe_8$ single-molecule magnet

### 2.4.1 Experimental section

**Syntheses**

All reactions were carried out in aerobic conditions using materials as received with no further purifications. Single crystals of $[(tacn)_6Fe_8O_2(OH)_{12}](ClO_4)_{3.9}Br_{4.1}\cdot 6H_2O$, (**4** – where tacn is 1,4,7-triazacyclononane) was made as previously reported in the literature.[107, 108]

**X-ray crystallography**

Prior to carrying-out the high-pressure measurements diffraction data were collected on a crystal of **4** at ambient temperature and pressure using graphite monochromated Mo-K$\alpha$ radiation and a Bruker Smart Apex diffractometer. The crystal was monoclinic and its unit-cell dimensions and angle were: $a$ = 14.1151(13), $b$ = 23.312(2), $c$ = 13.2398(13) Å, $\beta$ = 110.881(5)°, based on 6800 data 4.6º < $2\theta$ < 42º. The aim of this experiment was simply to verify the starting model of the sample used in this pressure study, and further crystallographic data are not given here. The

same crystal was used for the high-pressure diffraction measurements described below.

High-pressure experiments were carried out using a Merrill-Bassett diamond anvil cell (half opening angle 40º)[34], equipped with Boehler – Almax diamonds[77] with 600
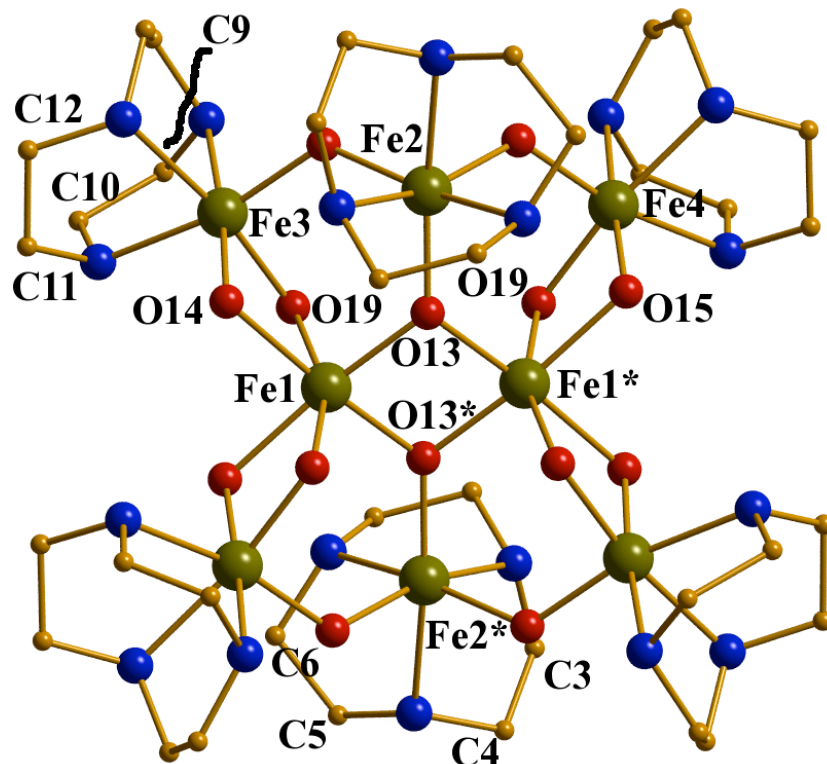


**Figure 19** The molecular structure of complex **4**. Color scheme: Fe= green, C = orange, O = red and N = blue. H atoms and counter ions are omitted for clarity.
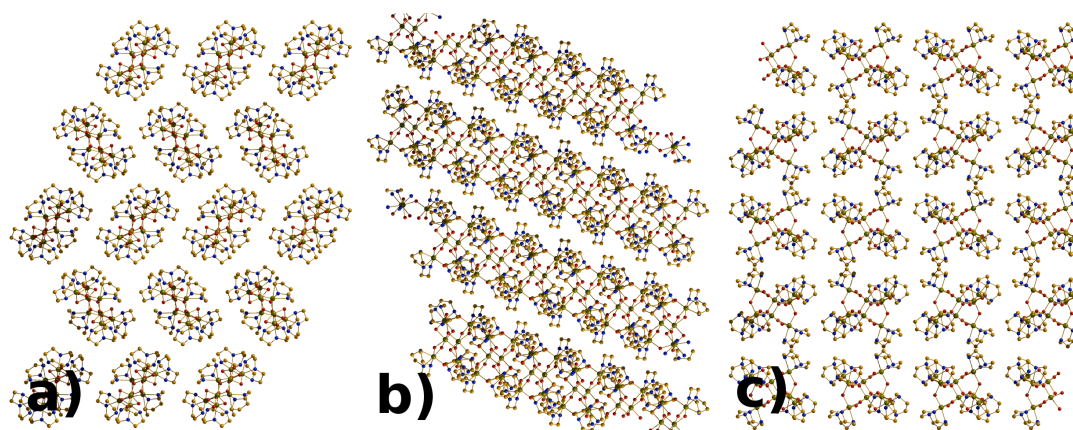


**Figure 20** Packing diagrams of **4** along the three crystallographic axes *a*, *b* and *c*.

μm culets and a tungsten gasket.[34] A 4:1 mixture of methanol and ethanol was used as a hydrostatic medium. A small ruby chip was loaded into the cell as the pressure

calibrant, with the ruby fluorescence used to measure the pressure.[78] Diffraction data were collected on Station 9.8 at the Synchrotron Radiation Source, Daresbury Laboratory on a Bruker SMART-APEX II[35] diffractometer with a silicon monochromator and a wavelength of λ = 0.4869 Å. The refinement based on the model of the original structure[107, 108] yielded a conventional R-factor of 0.0569 for 3229 data with $I > 2\sigma(I)$.

Data collection and processing procedures for the high pressure experiments were as described previously.[79] Integrations were carried out using the program SAINT,[36] and absorption corrections with the programs SADABS[40] and SHADE.[37] Data collections were taken at 0.2, 0.7, 1.2 and 2.0 GPa.

The refinements were quite challenging because of the presence of several disordered water molecules together with bromide and perchlorate ions that display both static and dynamic disorder. At high pressure the situation does not improve and, although the iron complex is largely well behaved, it was impossible to locate the H atoms on the water molecules in the highest pressure datasets. The perchlorates based on Cl(2) and Cl(3) were restrained to be tetrahedral. The perchlorate ion based on Cl(2) was rotationally disordered about one of the Cl-O bonds, and the remaining oxygen sites were modelled using a torus of electron density, as described by,[109] whilst on the main complex thermal similarities and vibrational restraints were applied up to 1.2 GPa. The 2.0 GPa dataset needed to be treated differently because the quality of the crystal had deteriorated; all the lighter atoms (C, N, O) had to be refined isotropically whilst Cl, Br and Fe atoms were refined anisotropically.

Unit cell details and refinement parameters are given in Table 13.

Structures were visualized using Diamond.[110] Void volumes were measured using Platon,[111] and visualized using Mercury.[112]

**High-Pressure Magnetic Measurements**

Variable temperature dc magnetic susceptibility measurements were made on a Quantum Design Magnetic Property Measurement System (SQUID magnetometer) equipped with a 7 T magnet operating in the 300-2 K temperature range. Diamagnetic corrections were applied using Pascal's constants. For the high-pressure magnetic measurements a cell of piston-cylinder design was constructed [55]. The body

of the pressure cell was made of non-magnetic CrNiAl and BERYLCO-25 alloys with zirconia rods used as pistons. The sample was contained inside a PTFE capsule with Daphne 7373 oil (IDEMITSU-ILS) used as the pressure transmitting medium. Pressure was applied in a hydraulic press and was calibrated by the load. Data were collected at 0.12, 0.25, 0.38, 0.57, 0.68, 0.82 and 0.93 GPa.

## 2.4.2 Results and Discussion

### Description of the Structures

The structure of complex **4**, (Figure 19) reported for the first time in 1984 by Wieghardt et al.[108], comprises a near-planar array of eight Fe(III) ions held together by a combination of twelve $\mu_2$-hydroxo bridges and two $\mu_3$-oxo bridges (O13 and symmetry equivalent), with each of the six peripheral ions further coordinated by an $\eta^3$-tacn (1,4,7-triazacyclononane) ligand. A disordered mixture of bromide and perchlorate counter ions in the ratio 4.1 : 3.9 maintains charge neutrality, with an

**Table 14** Selected bond distances (Å) involving the Fe ions and their associated oxo and hydroxo bridges in compound **4** at 0.2, 0.7, 1.2 and 2.0 GPa.

| P (GPa) | Fe1-O13* | Fe1-O13 | Fe1-O14 | Fe1-O15 | Fe1-O17 | Fe1-O19 | Fe2-O13 |
|---|---|---|---|---|---|---|---|
| 0.20 | 1.955(13) | 1.975(8) | 2.053(12) | 2.009(10) | 2.063(9) | 2.093(13) | 1.871(8) |
| 0.70 | 1.912(16) | 1.985(12) | 2.035(17) | 2.007(14) | 2.044(12) | 2.102(15) | 1.880(11) |
| 1.20 | 1.943(18) | 1.963(13) | 2.018(18) | 1.988(15) | 2.036(13) | 2.083(18) | 1.856(12) |
| 2.00 | 1.98(3) | 1.940(19) | 2.02(3) | 1.97(2) | 2.02(2) | 2.11(3) | 1.849(19) |
| P (GPa) | Fe2-O16 | Fe2-O(18) | Fe3-O16* | Fe3-O14 | Fe3-O17 | Fe4O15 | Fe4-O18 |
| 0.20 | 2.022(14) | 2.005(8) | 1.938(13) | 1.963(8) | 1.909(10) | 1.929(12) | 1.954(8) |
| 0.70 | 2.000(19) | 2.010(11) | 1.962(17) | 1.967(11) | 1.946(14) | 1.916(15) | 1.956(12) |
| 1.20 | 2.00(2) | 2.000(13) | 1.92(2) | 1.961(13) | 1.941(15) | 1.924(17) | 1.930(13) |
| 2.00 | 2.01(3) | 2.033(19) | 1.91(3) | 1.925(19) | 1..95(2) | 1.91(3) | 1.89(3) |

**Table 15** Selected bridging angles (°) involving the Fe ions and their associated oxo and hydroxo bridges in compound **1** at 0.2, 0.7, 1.2 and 2.0 GPa.

| P (GPa) | Fe1*-O13-Fe1 | Fe1*-O13-Fe2 | Fe1-O13-Fe2 | Fe1-O14-Fe3 | Fe1-O15-Fe4 | Fe1-O17-Fe3 |
|---|---|---|---|---|---|---|
| 0.20 | 96.1(4) | 130.0(6) | 129.0(5) | 99.5(5) | 102.4(6) | 101.0(4) |
| 0.70 | 97.2(5) | 132.2(8) | 126.6(7) | 99.8(6) | 102.5(8) | 100.2(5) |
| 1.20 | 96.7(6) | 130.7(10) | 128.2(8) | 99.7(7) | 102.0(9) | 99.7(6) |
| 2.00 | 96.1(9) | 130.3(13) | 129.4(12) | 100.3(11) | 103.4(14) | 99.4(9) |

additional six molecules of solvent water per cluster filling the intermolecular voids. When the structure is viewed (Figure 20a) along the crystallographic *a* axis the arrangement of the molecules is that of a *zig-zag* series of parallel chains of

molecules. When viewed along the crystallographic *b* and *c* axes (Figure 20b, 20c) the molecules align in rows.

## Effect of Pressure

Between ambient pressure and 2 GPa the unit cell volume of **4** contacts by 11.7% (Table 13). While the reduction along the *b* axis is fairly smooth and constant (Figure 21), plots of the lengths of the *a* and *c* axes seem to follow two separate regimes: one
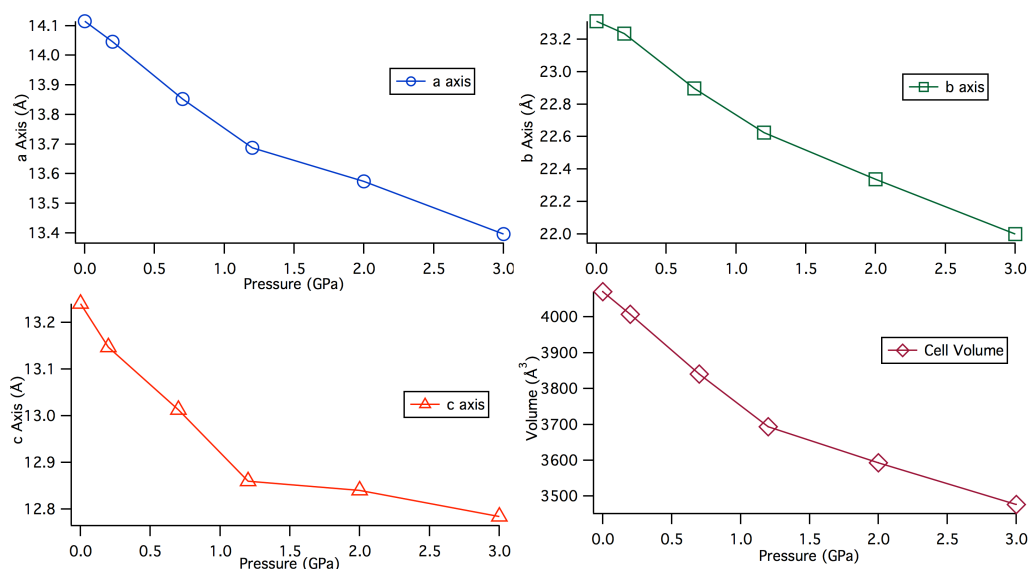


**Figure 21** Cell dimensions along the crystallographic axes *a*, *b*, *c* and unit cell volume.
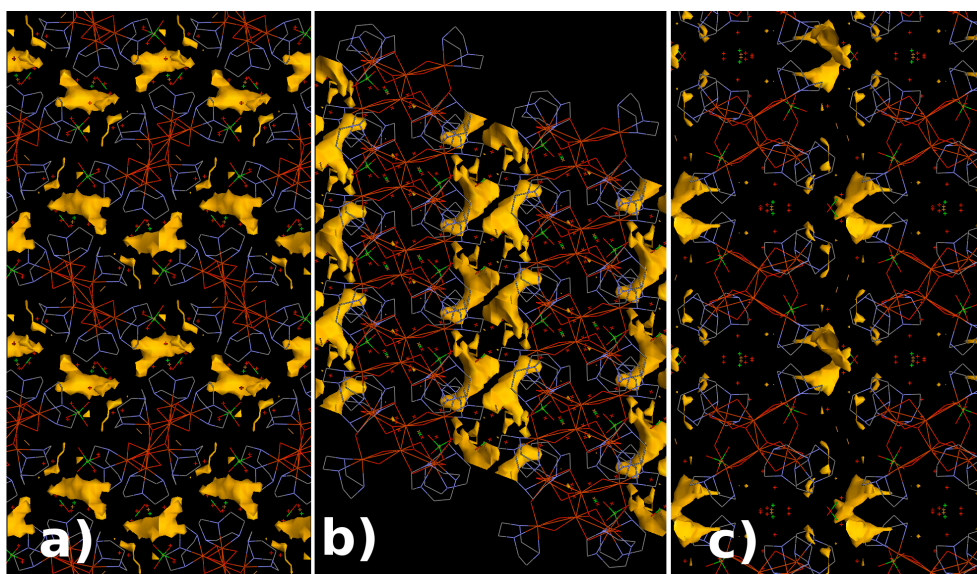


**Figure 22** Voids diagram of **4** along the three crystallographic axes *a*, *b* and *c* at 0.2 GPa.

from ambient pressure up to 1.2 GPa and the second from 1.2 GPa to 2.0 GPa

(Figure 21), with a similar pattern appearing for the contraction of cell volume (Table 13).

The cationic $[Fe_8]^{8+}$ cage complex itself appears rather unaffected by pressure, since the observed alterations in the bond distances and angles are not statistically significant (Table 14 and Table 15). Instead compression is taken up by the interstitial voids in the structure; Figures 22 and 23 show that the substantial void volume present at ambient pressure has virtually disappeared at 2 GPa. As this occurs intermolecular distances shorten, notably those formed between C atoms belonging to tacn ligands on one molecule and those on molecule next to it, and
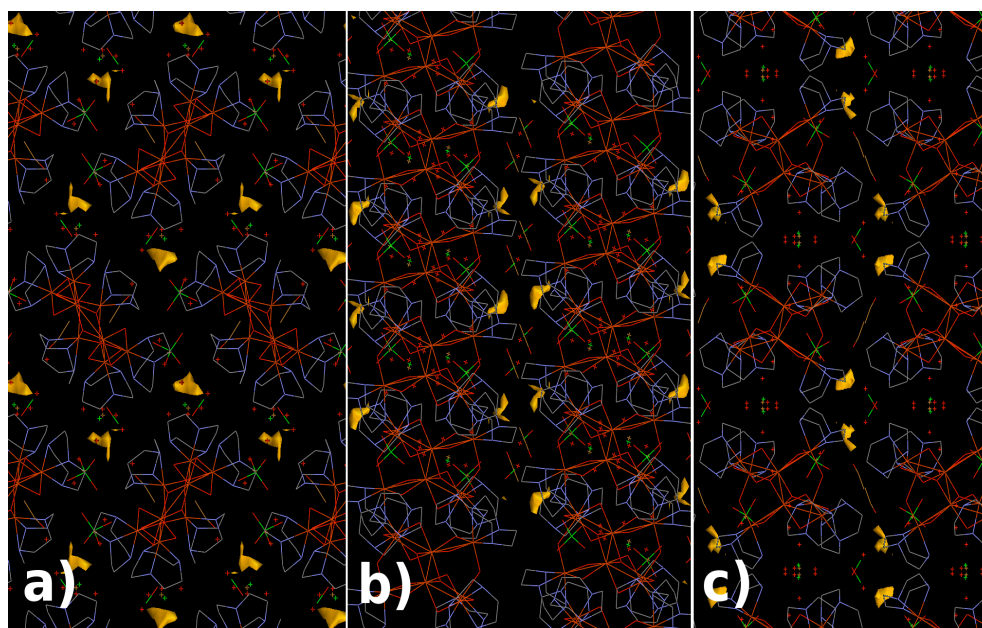


**Figure 23** Voids diagram of **4** along the crystallographic axes *a*, *b* and *c* at 2.0 GPa.

**Table 16** Selected intermolecular distances (Å) as function of pressure involving adjacent molecules of **4** and perchlorate anions in the crystal.

| P (GPa) | C3-C11 | C4-C12 | C5-Cl2 | C6-Cl1 | C9-Cl1 | C10-Cl2 |
|---|---|---|---|---|---|---|
| 0.20 | 3.658(18) | 4.160(20) | 4.893(23) | 3.726(24) | 3.879(19) | 4.278(22) |
| 0.70 | 3.525(25) | 3.983(27) | 4.811(21) | 3.679(27) | 3.800(23) | 4.167(26) |
| 1.20 | 3.373(29) | 3.919(32) | 4.740(25) | 3.710(30) | 3.786(25) | 4.096(31) |
| 2.00 | 3.354(43) | 3.775(46) | 4.660(39) | 3.673(53) | 3.717/41) | 3.971(41) |
| Δ/σ | 6.15 | 7.67 | 5.14 | 0.91 | 3.58 | 6.59 |

between the perchlorate anions (Table 16).

When the pressure was increased beyond 2 GPa the crystal disintegrated.

## Variation of magnetic properties with pressure

**4** is amongst the most widely studied of all single molecule magnets.[107, 113-115] At ambient pressure it has a spin ground state characterized by $S = 10$ and a magneto anisotropy $D = -0.20$ cm$^{-1}$, affording an energy barrier to magnetization reversal of $U_{eff} \approx 28$ K.

High-pressure magnetic susceptibility dc measurements on **4** were collected up to 0.93 GPa. Under pressure the room temperature $\chi_M T$ value of approximately 19 cm$^3$ K mol$^{-1}$ remains almost unchanged at all pressures (Figure 24). As the temperature is decreased the values start to increase slowly at first but more steeply below 100 K, until a peak is finally reached with a value of ~51 cm$^3$ K mol$^{-1}$ at approximately 10 K. Below 10 K the value of $\chi_M T$ drops sharply at all pressures, most likely due to ZFS effects. As can be clearly seen from Figure 4 all the variable pressure plots are essentially super-imposable on the ambient pressure data.
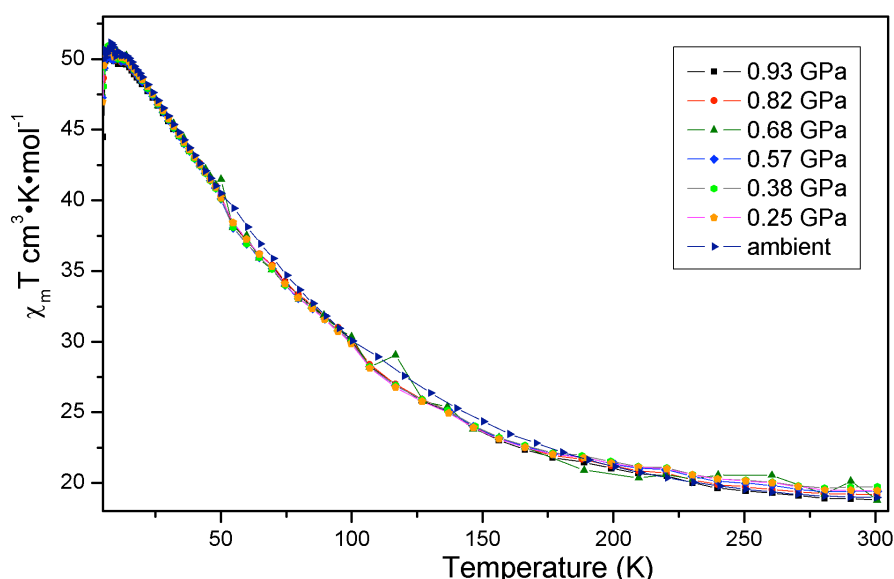


**Figure 24** Plots of $\chi_M T$ versus T for **1** recorded in the 300-5 K temperature range at the indicated pressures.

The independence of the magnetic properties of **4** with pressure up to 0.93 GPa are consistent with insensitivity of the structural parameters of the $[Fe_8]^{8+}$ cage to pressure. Where distortions of metal complexes are observed crystallographically (in two Mn6 and one Mn3 single molecule magnets), corresponding changes in the magnetic properties have also been observed. This is significant because it

demonstrates that changes in the magnetic properties that occur at high pressure are a consequence of induced distortions of the SMM complex, and not as the result of some other physical phenomenon.

The results presented here for **4** also illustrate the importance of crystal packing effects in determining the effect of pressure on a structure: we compress macroscopic crystals, not individual molecules. In **4** crystal packing is such that pressure is 'absorbed' by interstitial voids, without the need to distort the $Fe_8$ complex. In other SMM systems intramolecular conformational changes do occur with pressure. There therefore is no guarantee that pressure in the range of a few GPa can modify magnetic properties of a single-molecule magnet, and much depends on the characteristics of the individual system under study.

### 2.4.3 Conclusions

This last part the chapter reported a joint magnetic and single crystal diffraction study of a $Fe_8$ single molecule magnet. Magnetic data were measured to 0.93 GPa, whereas structural data are available up to 2 GPa. Though there is a significant decrease in the volume of the unit cell, this occurs via compression of interstitial voids rather than by alterations of the intramolecular structural parameters of the $Fe_8$ complex, and the geometry of the polymetallic metal cation remains largely unaffected. Consistently, there was also no significant change in the variable temperature susceptibility. While in some ways this is a 'negative' result, it validates the link made elsewhere in the literature between pressure-induced structural distortions and changes in magnetic properties.

It is notable that interstitial void space is essentially absent in **4** at 2 GPa, and it seems likely that some intramolecular effects would occur above this pressure. Indeed, the disintegration of **4** above 2 GPa is suggestive of a phase transition, which may well result in changes to the structure of the $Fe_8$ complexes.

## 2.5  References

1.      B. Bleaney and K. D. Bowers, *Proc. Roy. Soc. London*, 1952, **A214**, 451.
2.      D. Gatteschi, O. Kahn and R. D. Willet, *Magneto Structural Correlation in Exchange Coupled Systems*, D. Reidel, Dordrecht, 1985.
3.      V. H. Crawford, H. W. Richardson, J. R. Wasson, D. J. Hodgson and W. E. Hatfield, *Inorg. Chem.*, 1976, **15**, 2107.
4.      W. E. Hatfield, *Comm. Inorg. Chem.*, 1981, **1**, 105.
5.      J. Glerup, D. J. Hodgson and E. Petersen, *Acta Chem. Scandinav.*, 1983, **A37**, 161.
6.      M. F. Charlot, O. Kahn and M. Drillon, *Chem. Phys.*, 1982, **70**, 177.
7.      D. J. Hodgson, in *Magneto Structural Correlations in Exchange Coupled Systems*, eds. D. Gatteschi, O. Kahn and R. D. Willet, Reidel, D, Dordrecht, Editon edn., 1985, pp. 497.
8.      R. E. Marsh, *Acta Cryst.*, 1958, **11**, 654.
9.      C. P. Landee and R. E. Greeney, *Inorg. Chem.*, 1986, **25**, 3371.
10.     S. S. Tandon, L. K. Thompson, M. E. Manuel and J. N. Brisdon, *Inorg. Chem.*, 1994, **33**, 5555.
11.     Z. Xu, L. K. Thompson and D. O. Miller, *Inorg. Chem.*, 1997, **36**, 3985.
12.     L. K. Thompson, Z. Xu, A. E. Goeta, J. A. K. Howard, H. J. Clase and D. O. Miller, *Inorg. Chem.*, 1998, **37**, 3217.
13.     Z. Xu, L. K. Thompson, D. O. Miller, H. J. Clase, J. A. K. Howard and A. E. Goeta, *Inorg. Chem.*, 1998, **37**, 3620.
14.     S. M. Gorun and S. J. Lippard, *Inorg. Chem.*, 1991, **30**, 1625.
15.     H. Weihe and H. U. Güdel, *J. Am. Chem. Soc.*, 1997, **119**, 6539.
16.     H. Weihe and H. U. Güdel, *J. Am. Chem. Soc.*, 1998, **120**, 2870.
17.     T. Cauchy, E. Ruiz and S. Alvarez, *J. Am. Chem. Soc.*, 2006, **128**, 15722.
18.     F. Neese, *J. Am. Chem. Soc.*, 2006, **128**, 10213.
19.     M. R. Pederson and S. N. Khanna, *Phys. Rev. B*, 1999, **60**, 9566.
20.     A. V. Postnikov, J. Kortus and M. R. Pederson, *Phys. Stat. Sol.*, 2006, **243**, 2533.
21.     E. Ruiz, J. Cano, S. Alvarez and P. Alemany, *J. Am. Chem. Soc.*, 1998, **120**, 11122.
22.     M. Melnik, *Coord. Chem. Rev.,* 1982, **42**, 269.
23.     M. Kato and Y. Muto, *Coord. Chem. Rev.,* 1998, **92**, 45.
24.     S. Ohba, M. Kato, T. Tokii, Y. Muto and O. W. Stewart, *Mol. Cryst.Liq. Cryst. Science and Technology, Section A: Mol. Cryst.Liq. Cryst.*, 1993, **233**, 335.
25.     R. Hotzelmann, K. Wieghardt, U. Flörke, H. J. Haupt, D. C. Weatherburn, J. Bonvoisin, G. Blondin and J. J. Girerd, *J. Am. Chem. Soc.*, 1992, **114**, 1681.
26.     G. Fernández, M. Corbella, G. Aullón, M. A. Maestro and J. Mahía, *Eur. J. Inorg. Chem.*, 2007, 1285.
27.     K. Isele, F. Gigon, A. F. Williams, G. Bernardinelli, P. Franz and S. Decurtins, *Dalton Trans.*, 2007, 332.

28. M. A. Halcrow, J.-S. Sun, J. C. Huffman and G. Christou, *Inorg. Chem.*, 1995, **34**, 4167.
29. J. M. Clemente-Juan, B. Chansou, B. Donnadieu and J.-P. Tuchagues, *Inorg. Chem.*, 2000, **39**, 5515.
30. J. B. Vincent, H. R. Chang, K. Folting, J. C. Huffman, G. Christou and D. N. Hendrickson, *J. Am. Chem. Soc.*, 1987, **109**, 5703.
31. J. K. McCusker, H. G. Jang, S. Wang, G. Christou and D. N. Hendrickson, *Inorg. Chem.*, 1992, **31**, 1874.
32. J. K. McCusker, J. B. Vincent, E. A. Schmitt, M. L. Mino, K. Shin, D. K. Coggin, P. M. Hagen, J. C. Huffman, G. Christou and D. N. Hendrickson, *J. Am. Chem. Soc.*, 1991, **113**, 3012.
33. D. R. Allan, S. Parsons and S. J. Teat, *J Synchr. Rad.*, 2001, **8**, 10.
34. L. Merrill and W. A. Bassett, *Rev. Sci. Instrum.*, 1974, **45**, 290.
35. Bruker-Nonius, Madison, Wisconsin, USA, Editon edn., 2004, pp. Area-Detector Integration Software.
36. Bruker-Nonius, Bruker-AXS, Madison, Wisconsin, USA, Editon edn., 2006.
37. S. Parsons, The University of Edinburgh, Edinburgh, United Kingdom, Editon edn., 2004.
38. G. M. Sheldrick, University of Gottingen, Germany and Bruker-AXS, Gottingen, Germany and Madison, Wisconsin, USA, Editon edn., 2001.
39. G. M. Sheldrick, Bruker-AXS, Madison, WIsconsin, USA, Editon edn., 2001.
40. G. M. Sheldrick, Bruker-AXS, Madison, WIsconsin, USA, Editon edn., 2004.
41. D. J. Watkin, K. Prout, J. R. Carruthers, P. W. Betteridge and R. I. Cooper, Chemical Crystallography Laboratory, University of Oxford, Oxford, UK, Editon edn., 2003.
42. R. Miletich, D. R. Allan and W. F. Kuhs, *Rev. Mineral. Geochem.*, 2000, **41**, 445.
43. R. J. Angel, R. T. Downs and L. W. Finger, *Rev. Mineral. Geochem.*, 2000, **41**, 559.
44. S. A. Moggach, D. R. Allan, S. Parsons and L. Sawyer, *Acta Cryst. Sec. B*, 2006, **62**, 310.
45. S. A. Moggach, S. Parsons and L. Sawyer, *Acta Cryst. Sec. E*, 2006, **62**, 1046.
46. A. J. D. Moreno, P. T. C. Freire, F. E. A. Melo, M. A. Silva, I. Araujo; Guedes and J. Mendes Filho, *Sol. State Comm.*, 1997, **103**, 655.
47. I. D. H. Oswald, D. R. Allan, G. M. Day, W. D. S. Motherwell and S. Parsons, *Crys. Gro. Des.*, 2005, **5**, 1055.
48. D. R. Allan and S. J. Clark, *Phys. Rev. B*, 1999, **60**, 6328.
49. D. R. Allan, S. J. Clark, S. Parsons and M. Ruf, *J. Phys.: Condens. Matt.*, 2000, **12**, L613.
50. D. R. Allan, S. J. Clark, M. J. P. Brugmans, G. J. Ackland and W. L. Vos, *Phys. Rev. B*, 1998, **58**, R11809.
51. E. V. Boldyreva, *J. Mol. Struct.*, 2003, **647**, 159.
52. S. A. Moggach, S. Parsons and P. A. Wood, *Crystallogr. Rev.*, 2008, **14**, 143.
53. S. A. Moggach, D. R. Allan, C. A. Morrison, S. Parsons and L. Sawyer, *Acta Cryst. Sec. B*, 2005, **61**, 58.
54. P. Guionneau, M. Marchive, Y. Garcia, J. A. K. Howard and D. Chasseau, *Phys. Rev. B*, 2005, **72**, 214408.

55. K. V. Kamenev, S. Tancharakorn, N. Robertson and A. Harrison, *Rev. Sci. Instrum.*, 2006, **77**, 073905.

56. J. Sanchez-Benitez, S. Tancharakorn, M. K. Hutchinson and K. V. Kamenev, *J. Phys. Conf Ser.*, 2008, **121**, 122001.

57. M. Mito, H. Deguchi, T. Tajiri, S. Takagi, M. Yamashita and H. Miyasaka, *Phys. Rev. B*, 2005, **72**, 144421.

58. W. Kaneko, M. Mito, S. Kitagawa and M. Ohba, *Chem. Eur. J.*, 2008, **14**, 3481.

59. M. Ohba, W. Kaneko, S. Kitagawa, T. Maeda and M. Mito, *J. Am. Chem. Soc.*, 2008, **130**, 4475.

60. A. Sieber, R. Bircher, O. Waldmann, G. Carver, G. Chauboussant, H. Mutka and H. U. Güdel, *Angew. Chemi. Int. Ed.*, 2005, **44**, 4239.

61. A. Sieber, G. Chauboussant, R. Bircher, C. Boskovic, H. U. Güdel, G. Christou and H. Mutka, *Phys. Rev. B*, 2004, **70**, 172413.

62. Y. Suzuki, K. Takeda and K. Awaga, *Phys. Rev. B*, 2003, **67**, 132402/132401.

63. G. G. Levchenko, E. E. Zubov, V. N. Varyukhin, A. B. Gaspar and J. A. Real, *J. Phys. Chem. B*, 2004, **108**, 16664.

64. M. Mito, M. Fujino, H. Deguchi, S. Takagi, W. Fujita and K. Awaga, *Polyhedron*, 2005, **24**, 2501.

65. T. Tanaka, W. Fujita and K. Awaga, *Chem. Phys. Lett.*, 2004, **393**, 150-152.

66. W. Fujita and K. Awaga, *Mol. Cryst. Liq. Cryst. Sci. Technol., Sec. A*, 2000, **341**, 389.

67. M. Yamashita, H. Shimizu, K. Sakoyama, T. Manabe, T. Otsuka and K. Awaga, *Synth. Met.*, 1999, **103**, 2162.

68. K. Awaga, T. Sekine, M. Okawa, W. Fujita, S. M. Holmes and G. S. Girolami, *Chem. Phys. Lett.*, 1998, **293**, 352.

69. C. J. Milios, R. Inglis, A. Vinslava, R. Bagai, W. Wernsdorfer, S. Parsons, S. P. Perlepes, G. Christou and E. K. Brechin, *J. Am. Chem. Soc.*, 2007, **129**, 12505.

70. C. J. Milios, S. Piligkos and E. K. Brechin, *Dalton Trans.*, 2008, 1809.

71. C. J. Milios, A. Vinslava, W. Wernsdorfer, A. Prescimone, P. A. Wood, S. Parsons, S. P. Perlepes, G. Christou and E. K. Brechin, *J. Am. Chem. Soc.*, 2007, **129**, 6547.

72. C. J. Milios, A. Vinslava, S. A. Moggach, S. Parsons, W. Wernsdorfer, G. Christou, S. P. Perlepes and E. K. Brechin, *J. Am. Chem. Soc.*, 2007, **129**, 2754.

73. C. J. Milios, A. Vinslava, P. A. Wood, S. Parsons, W. Wernsdorfer, G. Christou, S. P. Perlepes and E. K. Brechin, *J. Am. Chem. Soc.*, 2007, **129**, 8.

74. L. F. Jones, M. E. Cochrane, B. D. Koivisto, D. A. Leigh, S. P. Perlepes, W. Wernsdorfer and E. K. Brechin, *Inorg. Chim. Acta*, 2008, **361**, 3420.

75. R. T. W. Scott, S. Parsons, M. Murugesu, W. Wernsdorfer, G. Christou and E. K. Brechin, *Chem. Comm.*, 2005, 2083.

76. A. Prescimone, J. Wolowska, G. Rajaraman, S. Parsons, W. Wernsdorfer, M. Murugesu, G. Christou, S. Piligkos, E. McInnes and E. K. Brechin, *Dalton Trans.*, 2007, 5282.

77. S. A. Moggach, D. R. Allan, S. Parsons and J. E. Warren, *J. Appl. Crystallogr.*, 2008, **41**, 249.

78. G. J. Piermarini, S. Block, J. D. Barnett and R. A. Forman, *J. Appl. Phys.*, 1975, **46**, 2774.
79. A. Dawson, D. R. Allan, S. Parsons and M. Ruf, *J. Appl. Crystallogr.*, 2004, **37**, 410.
80. V. Schomaker and K. N. Trueblood, *Acta Cryst.*, 1968, **B24**, 63.
81. S. Piligkos, University of Copenhagen, Copenhagen, Denmark, Editon edn.
82. J. J. Borrás-Almenar, J. M. Clemente-Juan, E. Coronado and B. S. Tsukerblat, *J. Comput. Chem.*, 2001, **22**, 985.
83. S. Carretta, T. Guidi, P. Santini, G. Amoretti, O. Pieper, B. Lake, J. van Slageren, F. El Hallak, W. Wernsdorfer, H. Mutka, C. Russina, C. J. Milios and E. K. Brechin, *Phys. Rev. Letters*, 2008, **100**, 157203.
84. K. A. Jackson and M. R. Pederson, *Phys. Rev. B*, 1990, **42**, 3276.
85. R. Boca, *Theoretical Foundations of Molecular Magnetism*, Elsevier, Lausanne, 1999.
86. F. Neese and E. I. Solomon, *Inorg. Chem.*, 1998, **37**, 6568.
87. S. Zein, C. Duboc, W. Lubitz and F. Neese, *Inorg. Chem.*, 2008, **47**, 134.
88. F. Neese, *J. Chem. Phys.*, 2007, **127**, 164112.
89. M. R. Pederson and K. A. Jackson, *Phys. Rev. B*, 1990, **41**, 7453.
90. M. R. Pederson, D. V. Porezag, J. Kortus and D. C. Patton, *Phys. Status Solidi b*, 2000, **217**, 197.
91. J. Kortus, M. R. Pederson, T. Baruah, N. Bernstein and C. S. Hellberg, *Polyhedron*, 2003, **22**, 1871.
92. K. Park, M. R. Pederson, S. L. Richardson, N. Ariaga-Alcalde and G. Christou, *Phys. Rev. B*, 2003, **68**, 020405.
93. T. Baruah and M. R. Pederson, *Int. J. Quant. Chem.*, 2003, **93**, 324.
94. M. R. Pederson, N. Bernstein and J. Kortus, *Phys. Rev. Letters*, 2002, **89**, 097202.
95. J. Kortus and M. R. Pederson, *Phys. Rev. B*, 2000, **62**, 5755.
96. J. Ribas-Ariño, T. Baruah and M. R. Pederson, *J. Am. Chem. Soc.*, 2006, **128**, 9497.
97. J. Ribas-Ariño, T. Baruah and M. R. Pederson, *J. Chem. Phys.*, 2005, **123**, 044303.
98. E. Ruiz, J. Cirera, J. Cano, S. Alvarez, C. Loose and J. Kortus, *Chem. Comm.*, 2008, 52.
99. J. Cirera, E. Ruiz, S. Alvarez, F. Neese and J. Kortus, *Chem.: Eur. J.*, 2008, accepted.
100. F. Neese, *J. Am. Chem. Soc.*, 2006, **128**, 10213.
101. J. Perdew, K. Burke and M. Ernzerhof, *Phys. Rev. Letters*, 1996, **77**, 3865.
102. S. Zein and F. Neese, *J. Phys. Chem. A*, 2008, **112**, 7976.
103. R. Reviakine, A. V. Arbuznikov, J.-C. Tremblay, C. Remenyi, O. L. Malkina, V. G. Malkin and M. Kaupp, *J. Chem. Phys.*, 2006, **125**, 054110.
104. Y. Sato, H. Miyasaka, N. Matsumoto and H. Okawa, *Inorg. Chim. Acta*, 1996, **247**, 57-63.
105. H. Miyasaka, R. Clérac, T. Ishii, H.-C. Chang, S. Kitagawa and M. Yamashita, *J. Chem. Soc., Dalton Trans*, 2002, 1528.
106. H. Miyasaka, K. Mizushima, S. Furukawa, K.-I. Sugiura, T. Ishii and M. Yamashita, *Mol. Cryst.Liq. Cryst.*, 2002, **379**, 171.
107. D. Gatteschi, R. Sessoli and A. Cornia, *Chem. Commun.*, 2000, 725.

108. K. Weighardt, K. Pohl, I. Jibril and G. Huttner, *Angew. Chemi. Int. Ed.*, 1984, **23**.

109. L. Schröder, D. J. Watkin, A. Cousson, R. I. Cooper and W. Paulus, *J. Appl. Cryst.*, 2004, **37**, 545.

110. K. Brandenburg and H. Putz, Crystal Impact, Bonn, Germany, Editon edn., 2005.

111. A. L. Spek, Utrecht University, Utrecht, The Netherlands, Editon edn., 2004, p. A multipurpose Crystallographic Tool.

112. C. F. Macrae, I. J. Bruno, J. A. Chisholm, P. R. Edgington, P. McCabe, E. Pidcock, L. Rodriguez-Monge, R. Taylor, J. Van de Streek and P. A. Wood, *J. Appl. Cryst.*, 2008, **41**, 466.

113. A.-L. Barra, F. Bencini, A. Caneschi, D. Gatteschi, C. Paulsen, C. Sangregorio, R. Sessoli and L. Sorace, *Chem. Phys. Chem.*, 2001, **2**, 523.

114. D. Gatteschi and R. Sessoli, *Angew. Chemi. Int. Ed.*, 2003, **42**, 268.

115. D. W. Yuan and Z. Zeng, *J Mag Magn. Mmat.*, 2006, **301**, 265.

# Chapter 3

# The Effect of Pressure on

# Hydroxo-bridged Copper

# Dimers

## 3.1  Introduction

Transition metal dimers have been studied in detail since the early 1950s when Bleaney and Bowers[1] established a theoretical expression to characterise the interaction between the Cu(II) centres in copper(II) acetate monohydrate as a function of temperature and the coupling constant, $J$. Hydroxo-bridged Cu(II) dimers[2] were one of the earliest and most extensively studied families of such molecules, borne from their relative simplicity: they are magnetically simple because each metal ion has only one unpaired electron; they can be either ferro- or antiferromagnetically coupled; and they are relatively simple to prepare. By the mid 1970s Hatfield and Hodgson[2] had derived an equation that predicts the $J$ value of planar hydroxo-bridged dimers based on the Cu-O-Cu bridging angle ($\square$). This states that an antiferromagnetic interaction is to be expected if $\alpha > 97.5°$, and a ferromagnetic interaction is to be expected if $\alpha < 97.5°$. Since this pioneering study many analogous molecules have been made and measured in an attempt to determine which other structural parameters (for example, the Cu-O and Cu-Cu distances, the twisting of the $[Cu_2O_2]$ core, the position of the H-atom of the hydroxide ligand *etc.*) can influence the magnetic behavior.[3-9]

In order to undertake such magneto-structural correlations the synthetic chemist must make many different molecules that all share a common magnetic core, and this necessitates the use of a different organic skeleton. This approach therefore assumes that variables such as the chemical nature of the chelating ligands and their coordination to the metal, the nature and number of counter ions and how they are positioned in the crystal lattice, the molecular and crystallographic symmetry *etc.*, have no effect on the measured magnetic properties. That is, all but the "magnetic" core is innocent.

The ideal scenario would be to have exactly the same dimer available in two, three or more different structural conformations, but this is essentially impossible via traditional chemical methods. An alternative way to achieve this is through the application of external hydrostatic pressure and to correlate the structural changes

seen by X-ray crystallography to magnetic changes observed in high pressure magnetometry.

In this chapter a combined high pressure study on one known and two novel hydroxo-bridged copper dimers are reported with the aim of extending the ambient pressure magneto-structural correlations on this well known family of complexes.

## 3.2 Experimental section

### 3.2.1 Syntheses

All reactions were carried out in aerobic conditions using materials as received with no further purification.

$[Cu_2(OH)_2(H_2O)_2(tmen)_2][ClO_4]_2$ (**5**; tmen = tetramethylethylenediamine). To a stirred solution of $Cu(ClO_4)_2$ (2 mmol) in water (30 ml) was added tmen (2 mmol) dropwise. The resulting blue solution was stirred for four hours. The solution was then filtered and left to slowly evaporate. After four days, the blue crystals obtained were isolated by filtration, washed with $Et_2O$ and dried *in vacuo*; yield ~50%. A sample for X-ray crystallography was kept in the mother liquor to prevent water loss. Anal. Calcd. (found) for **5**, $C_{12}H_{38}Cl_2Cu_2N_4O_{12}$: C, 22.93 (23.12); H, 6.09 (5.90); N, 8.92 (9.11).

$[Cu_2(OH)_2(tben)_2][ClO_4]_2$ (**6**; tben = di-$^t$butylethylenediamine). To a stirred solution of $Cu(ClO_4)_2$ (2 mmol) in  water (30 ml) was added tben (2 mmol) dropwise. The resulting blue solution was stirred for four hours. The solution was then filtered and left to slowly evaporate. After four days, the blue crystals obtained were isolated by filtration, washed with $Et_2O$ and dried *in vacuo*; yield ~40%. A sample for X-ray crystallography was kept in the mother liquor to prevent water loss. Anal. Calcd. (found) for **6**, $C_{20}H_{50}Cl_2Cu_2N_4O_{10}$: C, 34.09 (34.21); H, 7.15 (6.87); N, 7.95 (8.07).

$[Cu_2(OH)_2(bpy)_2][BF_4]_2$ (**7**; bpy = 2,2'-bipyridine). To a stirred solution of $Cu(BF_4)_2$ (2 mmol) in water (20 ml), a solution of bpy (2 mmol) in ethanol (20 ml) was added. The resulting blue suspension was then brought to a more basic pH by the addition of NaOH (0.1 M) until a colour change from deep to pale blue occurred and a clear solution was obtained. The resulting solution was stirred for six hours, before being filtered and allowed to stand. After three days the blue-green crystals obtained were

isolated by filtration, washed with Et$_2$O and dried *in vacuo*; yield ~40%. A sample for X-ray crystallography was kept in the mother liquor to prevent solvent loss. Anal. Calcd. (found) for **7**, C$_{20}$H$_{18}$B$_2$Cu$_2$F$_8$N$_4$O$_2$: C, 37.12 (37.28); H, 2.80 (2.65); N, 8.66 (8.71).

**Table 1** Crystallographic data for Complex **5** at 0.25, 0.70, 1.20 and 2.50 GPa.

| Crystal data | 5 – [Cu$_2$(OH)$_2$(H$_2$O)$_2$(tmen)$_2$][ClO$_4$]$_2$ | | | |
| | 0.25 GPa | 0.7 GPa | 1.2 GPa | 2.5 GPa |
|---|---|---|---|---|
| Chemical formula | **5** | **5** | **5** | **5**·[Cu$_2$(OH)$_2$(H$_2$O)(tmen)$_2$][ClO$_4$]$_2$ |
| Space group | Monoclinic, *P2$_1$/c* | Monoclinic, *P2$_1$/c* | Monoclinic, *P2$_1$/c* | Triclinic, *P* $\overline{1}$ |
| T (K) | 300 | 300 | 300 | 300 |
| *a*, | 7.7554 (3), | 7.6403 (3), | 7.5255 (4), | 11.0214 (10), |
| *b*, | 15.0450 (4), | 14.7724 (4), | 14.4578 (5), | 14.705 (3), |
| *c* (Å) | 11.2606 (4) | 11.1904 (4) | 11.1416 (4) | 16.0463 (18) |
| a, | 90, | 90, | 90, | 62.486 (12), |
| b, | 106.887 (2), | 107.386 (3), | 108.311 (2), | 81.394 (7), |
| γ (°) | 90 | 90 | 90 | 69.543 (11) |
| *V* (Å$^3$) | 1257.23 (8) | 1205.31 (7) | 1150.85 (8) | 2160.9 (6) |
| Radiation type, λ (Å) | Synchrotron, 0.4869 | Synchrotron, 0.4869 | Synchrotron, 0.4869 | Synchrotron, 0.4869 |
| μ (mm$^{-1}$) | 1.96 | 2.05 | 2.15 | 2.28 |
| Crystal size (mm) | 0.12 × 0.10 × 0.08 | 0.12 × 0.10 × 0.08 | 0.12 × 0.10 × 0.08 | 0.12 × 0.10 × 0.08 |
| $T_{min}$/$T_{max}$ | 0.07 / 0.85 | 0.38 / 0.85 | 0.18 / 0.84 | 0.01 / 0.83 |
| Measured, independent, observed reflections | 11332, 1652, 1253 | 11243, 1646, 1122 | 11994, 2004, 1156 | 14618, 2633, 1150 |
| Criterion for observed reflections | *I* > 2.0σ(*I*) | *I* > 2.0σ(*I*) | *I* > 2.0σ(*I*) | *I* > 2.0σ(*I*) |
| $R_{int}$ | 0.074 | 0.084 | 0.071 | 0.098 |
| θ$_{max}$ (°) | 17.5 | 17.7 | 20.4 | 15.7 |
| Refinement | *F* | *F* | *F* | *F* |
| R, *wR*, S | 0.077, 0.101, 1.30 | 0.083, 0.099, 1.11 | 0.125, 0.147, 1.12 | 0.106, 0.057, 0.99 |
| Reflections | 1253 | 1122 | 1156 | 1150 |
| Parameters | 118 | 118 | 113 | 238 |
| Restraints | 4 | 42 | 42 | 73 |
| Δr$_{max}$ Δr$_{min}$ | 1.09, –0.72 (e·Å$^{-3}$) | 1.09, –0.86 (e·Å$^{-3}$) | 1.86, –1.10 (e·Å$^{-3}$) | 0.64, –0.51 (e·Å$^{-3}$) |

### *3.2.2 X-ray crystallography*

High-pressure single crystal X-ray diffraction experiments were carried out using a Merrill-Bassett diamond anvil cell (half-opening angle 40°),[10] equipped with Boehler-Almax diamonds with 600 µm culets and a tungsten gasket.[11] Petroleum ether was used as hydrostatic medium for all the compounds and a small ruby chip

was loaded into the cell as the pressure calibrant with the ruby fluorescence used to measure the pressure.[12] Diffraction data were collected using synchrotron radiation

**Table 2** Crystallographic data for Complex **6** at ambient pressure, 0.21 and 0.90 GPa.

| Crystal data | 6 – [Cu$_2$(OH)(tben)$_2$][ClO$_4$]$_2$ | | |
| --- | --- | --- | --- |
| | ambient | 0.21 GPa | 0.9 GPa |
| Space group | Monoclinic, $C2/c$ | Monoclinic, $C2/c$ | Monoclinic, $C2/c$ |
| T (K) | 150 | 300 | 300 |
| $a, b, c$ (Å) | 29.8826 (6), 11.7561 (2), 18.9518 (4) | 30.038 (10), 11.866 (2), 18.963 (6) | 29.083 (12), 11.634 (3), 18.528 (8) |
| β (°) | 103.6960 (10) | 104.837 (18) | 105.20 (2) |
| $V$ (Å$^3$) | 6468.5 (2) | 6533 (3) | 6050 (4) |
| Radiation, λ (Å) | Mo-$K\alpha$ | Synchrotron, 0.47670 | Synchrotron, 0.47670 |
| μ (mm$^{-1}$) | 1.53 | 1.52 | 1.64 |
| Crystal size (mm) | $0.25 \times 0.21 \times 0.10$ | $0.12 \times 0.11 \times 0.09$ | $0.13 \times 0.11 \times 0.90$ |
| $T_{min}/T_{max}$ | 0.56 / 0.86 | 0.37 / 0.87 | 0.00 / 0.23 |
| Measured, Independent, Observed reflections | 38959, 7982, 5207 | 11282, 1864, 1124 | 5849, 1276, 670 |
| Criterion for observed reflections | $I > 2.0\sigma(I)$ | $I > 2.0\sigma(I)$ | $I > 2.0\sigma(I)$ |
| $R_{int}$ | 0.046 | 0.118 | 0.168 |
| $\theta_{max}$ (°) | 29.0 | 14.5 | 13.1 |
| Refinement | $F^2$ | $F$ | $F$ |
| $R_1$, $wR$, $S$ | 0.039, 0.009, 0.99 | 0.073, 0.081, 1.07 | 0.123, 0.085, 1.59 |
| Reflections | 7522 | 1124 | 670 |
| Parameters | 343 | 303 | 173 |
| Restraints | 4 | 256 | 54 |
| $\Delta\rho_{max}$, $\Delta\rho_{min}$ (e Å$^{-3}$) | 0.94, –0.72 | 0.56, –0.51 | 0.51, –0.51 |
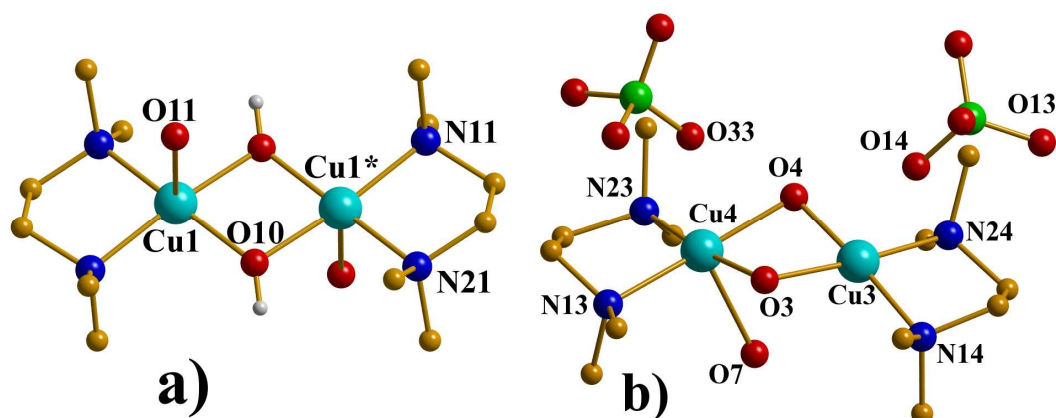


**Figure 1** The molecular structure of complex **5**: a) at 0.25 GPa  b) at 2.5 GPa – Colour scheme: Cu = turquoise, C = gold, O = red and N = blue. Most of the H atoms and counter ions are omitted for clarity, in part b) the second independent dimer has been omitted as its structure is similar to that in a).

of wavelength λ = 0.4869 Å for **5**, 0.4767 Å for **6** and **7**; all at room temperature on a Bruker Smart APEX II diffractometer[13] at Station 9.8 at SRS, Daresbury

Laboratory.[14] Integrations were carried out using the program SAINT[15] and absorption corrections with the program SADABS[16] and SHADE.[17] Data collections were taken at 0.25, 0.70, 1.20 and 2.50 GPa for **5**, at 0.21 and 0.90 GPa for **6** and at 0.30, 0.80, 1.53, 2.25, 2.80, 3.50, 4.00, 4.30 and 4.70 GPa for **7**. Refinements of the compressed forms of **5**, **6** and **7** were carried out starting from the coordinates obtained from a separate data collection carried out under ambient conditions using Mo-Kα raditation on a Bruker Smart diffractometer. The program CRYSTALS[18] was used to refine the structures of **5** and **6** against $F$ using the reflections with $I>2\sigma$; **7** has been refined against $F^2$ using all reflections.

Due to the low completeness of the data sets, some thermal similarity restraints on C and N thermal parameters have been applied on data sets of **5** up to 1.20 GPa, whilst in the 2.50 GPa data set perchlorate anions were restrained to be tetrahedral, and only the Cu and Cl atoms could be refined anisotropically. Restraints on the shape of the perchlorates and on the C-C and C-N distances as well as anisotropic refinement of only the heavy atoms were required for **6**. In contrast, complex **7** did not require any special treatment during its processing. Unit cells and refinement parameters are reported in Tables 1, 2 and 3. Voids were calculated using PLATON[19] and visualised with MERCURY[20] while structures and packing diagrams were drawn using DIAMOND.[21]

### 3.2.3  Magnetic measurements.

Variable temperature magnetic susceptibility dc measurements were made on a Quantum Design Magnetic Property Measurement System (SQUID magnetometer) equipped with a 7T magnet operating in the 350 - 2 K temperature range. Diamagnetic corrections were applied using Pascal's constants. For the high-pressure magnetic measurements a cell of piston-cylinder design was constructed.[22] The body of the pressure cell was made of non-magnetic CrNiAl and BERYLCO-25 alloys with zirconia rods used as pistons. The sample was contained inside a PTFE capsule with Daphne 7373 oil (IDEMITSU-ILS) used as the pressure transmitting medium. Pressure was applied in a hydraulic press and was calibrated by the load. Data were collected at 0.22, 0.59 and 0.84 GPa for **5**, at 0.30, 0.58, 0.87 GPa for **6** and at 0.40,

0.61 and 0.86 GPa for **7**. The program MAGPACK[23] has been used to simulate susceptibility curves.

**Table 3** Crystallographic Data for **7** at ambient pressure, 0.30, 0.80, 1.53, 2.25 GPa.

| Crystal data | ambient | 0.30 GPa | 0.80 GPa | 1.53 GPa | 2.25 GPa |
|---|---|---|---|---|---|
| | | $7 - [Cu_2(OH)_2(bipy)_2][BF_4]_2$ | | | |
| Spacegroup | Monoclinic, $C2/m$ | Monoclinic, $C2/m$ | Monoclinic, $C2/m$ | Monoclinic, $C2/m$ | Monoclinic, $C2/m$ |
| T (K) | 150 | 300 | 300 | 300 | 300 |
| $a, b, c$ (Å) | 13.312 (6), 15.054 (7), 6.245 (2) | 13.323 (2), 15.038 (3), 6.2630 (6) | 13.0669 (18), 14.932 (2), 6.1859 (5) | 12.8135 (15), 14.810 (2), 6.1079 (4) | 12.628 (2), 14.716 (3), 6.0524 (6) |
| $\beta$ (°) | 115.06 (2) | 115.043 (8) | 114.558 (7) | 114.240 (7) | 113.837 (9) |
| $V$ (Å$^3$) | 1133.6 (9) | 1136.8 (3) | 1097.8 (3) | 1056.9 (2) | 1028.8 (3) |
| Radiation $\lambda$(Å) | Mo $K\alpha$ | Synchrotron, 0.47670 | Synchrotron, 0.47670 | Synchrotron, 0.47670 | Synchrotron, 0.47670 |
| $\mu$ (mm$^{-1}$) | 1.97 | 1.97 | 2.04 | 2.11 | 2.17 |
| Crystal size (mm) | 0.28 x 0.21 x 0.15 | 0.15 x 0.13 x 0.10 | 0.15 x 0.13 x 0.10 | 0.15 x 0.13 x 0.10 | 0.15 x 0.13 x 0.10 |
| $T_{min}/T_{max}$ | 0.66 /0.74 | 0.56 / 0.82 | 0.64 / 0.82 | 0.63 / 0.81 | 0.59 / 0.80 |
| measured, independent, observed reflections | 13989, 1707, 1467 | 2969, 779, 595 | 2362, 689, 581 | 2801, 725, 609 | 2258, 646, 552 |
| Criterion for observed reflections | $I > 2.0\sigma(I)$ | $I > 2.0\sigma(I)$ | $I > 2.0\sigma(I)$ | $I > 2.0\sigma(I)$ | $I > 2.0\sigma(I)$ |
| $R_{int}$ | 0.061 | 0.060 | 0.046 | 0.042 | 0.039 |
| $\theta_{max}$ (°) | 30.3 | 17.4 | 17.3 | 17.5 | 17.5 |
| Refinement | $F^2$ | $F^2$ | $F^2$ | $F^2$ | $F^2$ |
| $R_1$, wR, S | 0.049, 0.058, 1.20 | 0.038, 0.076, 0.90 | 0.039, 0.062, 1.91 | 0.030, 0.064, 0.91 | 0.033, 0.073, 1.01 |
| Reflections | 1650 | 761 | 678 | 708 | 633 |
| Parameters | 94 | 94 | 94 | 94 | 94 |
| $\Delta\rho_{max}$, $\Delta\rho_{min}$ | 0.60, –0.68 | 0.38, –0.38 | 0.33, –0.31 | 0.37, –0.25 | 0.36, –0.44 |

## 3.3   Results and Discussion

### 3.3.1   *Description of Structures*

The structures of  **5**, **6** and **7** all display the same central metallic skeleton which comprises a diamond-shaped $[Cu_2(OH)_2]$ unit of two $Cu^{(II)}$ ions bridged by two $\mu$-OH⁻ ligands (Figures 1 and 2). In **5** the copper ions are square pyramidal ($\tau$-value[24] $\tau$ = 0.07) with a $[CuO_3N_2]$ coordination sphere, with one molecule of water and one tmen ligand per metal centre. In **6** the bulky $^t$butyl groups the tben ligands impose

greater steric restraints on the molecule, such that the geometries of the metal ions are intermediate between square planar and tetrahedral (average L-M-L $\approx$ 44°)

**Table 4** Crystallographic Data for Complex **7** at ambient pressure, 2.80, 3.50, 4.00, 4.30 and 4.70 GPa

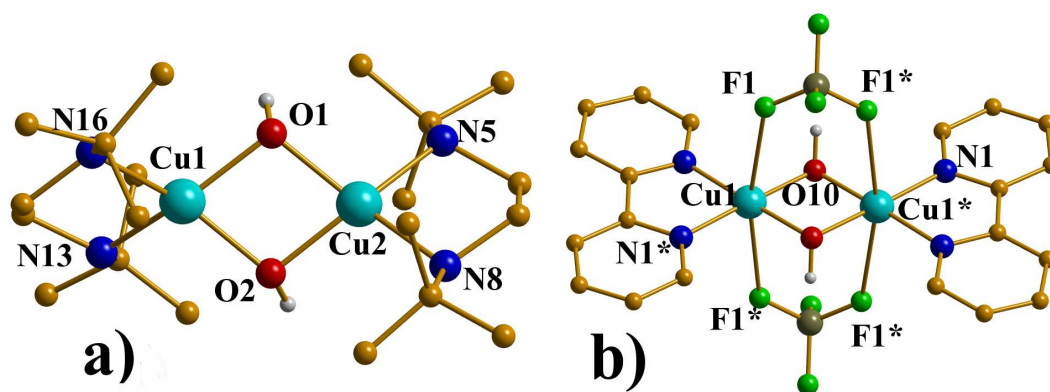| Crystal data | 7 – $[Cu_2(OH)_2(bipy)_2][BF_4]_2$ | | | | |
| --- | --- | --- | --- | --- | --- |
| | **2.80 GPa** | **3.50 GPa** | **4.00 GPa** | **4.30 GPa** | **4.70 GPa** |
| Spacegroup | Monoclinic, *C*2/*m* | Monoclinic, *C*2/*m* | Monoclinic, *C*2/*m* | Monoclinic, *C*2/*m* | Monoclinic, *C*2/*m* |
| T (K) | 300 | 300 | 300 | 300 | 300 |
| *a*, *b*, *c* (Å) | 12.5039 (16), 14.673 (2), 6.0173 (5) | 12.3731 (7), 14.6135 (10), 5.9739 (2) | 12.2874 (15), 14.573 (2), 5.9483 (4) | 12.3731 (7), 14.6135 (10), 5.9739 (2) | 12.1792 (16), 14.516 (2), 5.8991 (5) |
| β (°) | 113.653 (7) | 113.441 (3) | 113.258 (7) | 113.441 (3) | 112.909 (8) |
| *V* (Å$^3$) | 1011.3 (2) | 991.02 (10) | 978.6 (2) | 991.02 (10) | 960.7 (2) |
| Radiation, λ (Å) | Synchrotron, 0.47670 | Synchrotron, 0.47670 | Synchrotron, 0.47670 | Synchrotron, 0.47670 | Synchrotron, 0.47670 |
| μ (mm$^{-1}$) | 2.21 | 2.25 | 2.28 | 2.25 | 2.33 |
| Crystal size (mm) | 0.15 x 0.13 x 0.10 | 0.15 x 0.13 x 0.10 | 0.15 x 0.13 x 0.10 | 0.15 x 0.13 x 0.10 | 0.15 x 0.13 x 0.10 |
| $T_{min}/T_{max}$ | 0.65 / 0.80 | 0.65 / 0.80 | 0.59 / 0.80 | 0.62 / 0.80 | 0.56 / 0.79 |
| measured, independent, observed reflections | 2599, 679, 569 | 2792, 698, 587 | 2579, 667, 566 | 2225, 617, 532 | 1875, 571, 481 |
| Criterion for observed reflections | $I > 2.0\sigma(I)$ | $I > 2.0\sigma(I)$ | $I > 2.0\sigma(I)$ | $I > 2.0\sigma(I)$ | $I > 2.0\sigma(I)$ |
| $R_{int}$ | 0.037 | 0.033 | 0.040 | 0.041 | 0.056 |
| $\theta_{max}$ (°) | 17.4 | 17.3 | 17.3 | 17.3 | 17.3 |
| Refinement on | $F^2$ | $F^2$ | $F^2$ | $F^2$ | $F^2$ |
| $R_1$, *wR*, *S* | 0.029, 0.085, 0.75 | 0.030, 0.062, 0.74 | 0.035, 0.119, 0.75 | 0.048, 0.158, 0.92 | 0.040, 0.085, 1.23 |
| Reflections | 669 | 689 | 656 | 603 | 550 |
| Parameters | 94 | 94 | 94 | 91 | 94 |
| Δρ$_{max}$, Δρ$_{min}$ | 0.34, –0.30 | 0.32, –0.40 | 0.43, –0.42 | 0.51, –0.40 | 0.39, –0.44 |



**Figure 2** The molecular structure of complex **6** in a) and complex **7** in b) – Colour scheme: Cu = turquoise, C = gold, O = red, N = blue, B = dark green and F = light green. H atoms and counter ions are omitted for clarity.

making additional ligation by solvent impossible and forcing the Cu ions to be four coordinate with $[CuO_2N_2]$ coordination spheres. The copper centres in **7** are in (Jahn-Teller, JT) distorted octahedral geometries with $[CuO_2N_2F_2]$ coordination spheres, comprising the two $OH^-$ bridging ions, one molecule of bpy and two $BF_4^-$ ions; the F-Cu-F vector defining the JT axis (Figure 2b). The charge neutrality in **5** and **6** is maintained by the presence of two perchlorate ions per complex. The Cu-O-Cu bridging angles (Tables 5-7) are 102.03(13)° for **5**, 102.72(6)° and 101.62(6)° for **6**, and 97.40(14)° for **7**. When viewed along the crystallographic *a* axis, molecules of **5** lie in a head-to-tail fashion such that they form a zig-zag like packing of the molecules, whilst when viewed along the *b* and *c* axes they appear aligned in infinite 1D rows (Figure 3). In complex **6** the molecules align in parallel straight rows along the *a* direction, forming *S*-shaped and "butterfly-like" dimeric units of molecules along the *b* and *c* axes, respectively (Figure 4). The packing diagrams of **7**, shown in Figure 5, are perhaps the most aesthetically pleasing with the molecules forming infinite parallel rows down the *a* axis, and alternate parallel rows down the *b* and *c* axes (Figure 5).

### 3.3.2 Effect of Pressure on the structure of 5

The most evident consequence of the application of pressure is the constant contraction of the unit cell (Table 1). Due to the lack of strong inter-molecular interactions, such as H-bonds or $\pi$-$\pi$ stacking, the compression is driven by the reduction of the lattice voids (Figure 6): using a probe of 0.8 Å, at 0.21 GPa the void/volume ratio is approximately 13.4% of the total unit cell volume whereas at 1.20 GPa the ratio is essentially 0%. Although the compression of the inter-molecular voids reduces the tension on bonds and angles of the molecules in the crystal, at 1.20 GPa some distortions are already visible (Table 5). In particular the Cu-O-Cu bridging angle is becoming more acute, the 102.03(13)° seen under ambient conditions decreasing to 101.2(3)° at 0.21 GPa and 99.7(7)° at 1.20 GPa. As a consequence the intra-molecular Cu-Cu distance is also shortened from 2.9784(12) Å at ambient pressure to 2.939(3) Å at 1.2 GPa. At ambient pressure the water molecule bonded to each copper ion is approximately perpendicular to the Cu-Cu vector with an angle of 91.41(16)°, but becomes severely distorted at higher

pressures, the Cu-Cu-O angle becoming 80.4(7)° at 1.2 GPa (Table 5). The reason
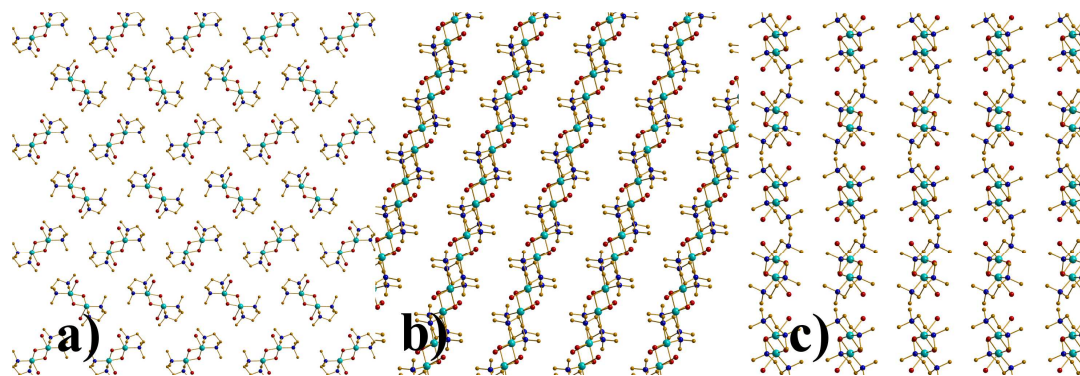


**Figure 3** Packing diagrams of **5** along the three crystallographic axes *a*, *b* and *c*.
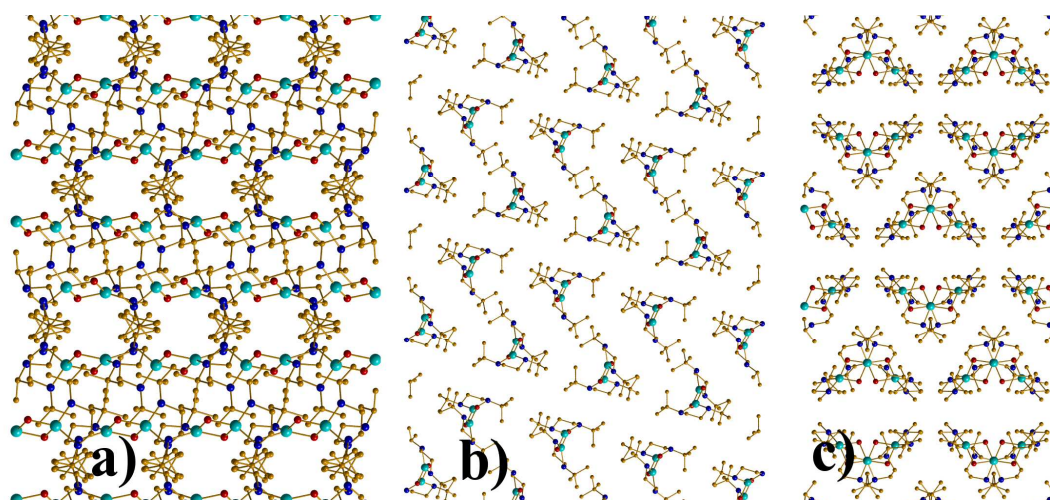


**Figure 4** Packing diagrams of **6** along the three crystallographic axes *a*, *b* and *c*.

**Table 5** Bond distances and angles in **5** as a function of pressure up to 1.2 GPa – Before the phase transition.

| P (GPa) | Cu1-Cu1* | Cu1-O10 | Cu1-N11 | Cu1-N21 |
|---------|----------|---------|---------|---------|
| 0 | 2.9784(12) | 1.911(4) | 2.023(4) | 2.043(5) |
| 0.25 | 2.9578(19) | 1.913(6) | 2.029(8) | 2.033(7) |
| 0.7 | 2.946(2) | 1.899(7) | 2.025(9) | 2.043(7) |
| 1.2 | 2.939(3) | 1.905(18) | 2.011(10) | 2.026(9) |
| Δ/σ | 12.3 | 0 | 1.1 | 1.6 |
| **P (GPa)** | **Cu1-O11** | **Cu1-O1** | **Cu1-O10-Cu1** | **Cu1-Cu1-O11** |
| 0 | 2.535(7) | 4.429(7) | 102.03(13)° | 91.41(16)° |
| 0.25 | 2.501(15) | 4.673(13) | 101.2(3)° | 88.7(3)° |
| 0.7 | 2.47(2) | 4.678(13) | 101.1(3)° | 87.4(3)° |
| 1.2 | 2.47(3) | 4.639(16) | 99.7(7)° | 80.4(7)° |
| Δ/σ | 2.1 | 12.1 | 3.8 | 15.5 |

for such a big modification is most probably the reduction of the inter-molecular

**Table 6** Bond distances and angles in **5** as a function of pressure at 1.2 and 2.5 GPa – before and after the phase transition – atoms are marked according to the "after phase" labels.

| P (GPa) | Cu1-Cu2 | Cu1-O1 | Cu1-O2 | Cu2-O1 |
|---|---|---|---|---|
| **1.2** | 2.939(3) | 1.905(18) | 1.905(18) | 1.905(18) |
| **2.5** | 2.914(3) | 1.941(11) | 1.979(15) | 1.907(11) |
| **Δ/σ** | 5.9 | 1.7 | 3.1 | 0 |
| **P (GPa)** | **Cu1-O2-Cu2** | **Cu2-Cu1-O6** | **Cu1-Cu2-O5** | **Cu1-O13** |
| **1.2** | 99.7(7)° | 80.4(7)° | 80.4(7)° | 4.639(16) |
| **2.5** | 99.5(6)° | 80.1(4)° | 91.2(4)° | 3.733(16) |
| **Δ/σ** | 0 | 0 | 13.4 | 40 |
| **P (GPa)** | **Cu4-O4** | **Cu4-O7** | **Cu4-O33** | **Cu3-O7** |
| **1.2** | 1.905(18) | 2.47(3) | 4.639(16) | 4.639(16) |
| **2.5** | 1.89(3) | 2.36(3) | 2.964(12) | 2.920(15) |
| **Δ/σ** | 0 | 2.59 | 84 | 78 |
| **P (GPa)** | **Cu2-O2** | **Cu1-O6** | **Cu2-O5** | **Cu1-O1-Cu2** |
| **1.2** | 1.905(18) | 2.47(3) | 2.47(3) | 99.7(7)° |
| **2.5** | 1.838(17) | 2.51(4) | 2.24(3) | 98.4(4)° |
| **Δ/σ** | 2.7 | 0 | 5.4 | 1.6 |
| **P (GPa)** | **Cu3-Cu4** | **Cu3-O3** | **Cu3-O4** | **Cu4-O3** |
| **1.2** | 2.939(3) | 1.905(18) | 1.905(18) | 1.905(18) |
| **2.5** | 2.849(9) | 1.90(4) | 2.004(16) | 2.003(17) |
| **Δ/σ** | 9.5 | 0 | 4.1 | 4 |
| **P (GPa)** | **Cu3-O14** | **Cu3-O3-Cu4** | **Cu3-O4-Cu4** | **Cu3-Cu4-O7** |
| **1.2** | 4.639(16) | 99.7(7)° | 99.7(7)° | 80.4(7)° |
| **2.5** | 3.008(7) | 93.9(13)° | 94.0(7)° | 67.4(6)° |
| **Δ/σ** | 93 | 3.9 | 5.75 | 14.1 |
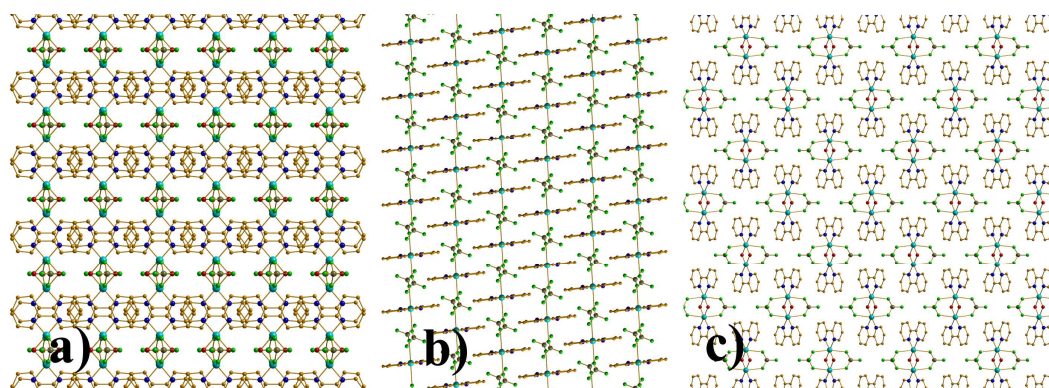


**Figure 5** Packing diagrams of **7** along the three crystallographic axes *a*, *b* and *c*.

distances that, in particular, brings one of the perchlorate anions very close to the coordinated water position: at 1.20 GPa the distance between the water molecule and the centroid of the three disordered oxygens of the anion is only 3.50 Å. Because of the lack of voids and the close $H_2O\cdots ClO_4$ contact, a further increase in pressure induces a phase transition between 1.20 and 2.50 GPa. At the highest pressure measured the space group has changed from monoclinic *P2₁/c* to triclinic $P\bar{1}$, the

result being that the asymmetric unit now contains two full dimer molecules and four perchlorate anions, as opposed to the one half of a dimer and one perchlorate present at ambient pressure.
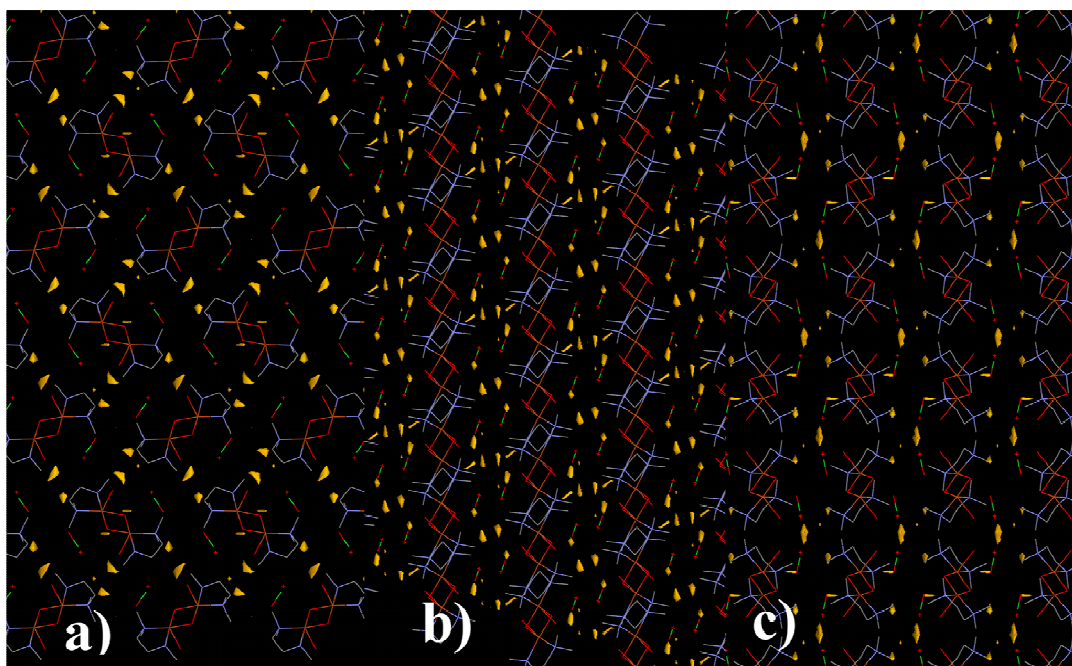


**Figure 6** Void diagrams of **5** along the three crystallographic axes *a*, *b* and *c* at 0.25 GPa – Probe size: 0.8 Å.

The loss of symmetry is likely caused by the elimination of one of the coordinated water molecules from 50% of the dimers present in the structure. To the best of our knowledge this is the first ever example of pressure-induced $H_2O$ elimination. The water ejection produces two different complexes: one with two waters (Cu1-Cu2) and one with only one (Cu3-Cu4) (Figure 1b). This rather distruptive phase transition causes re-arrangements in the intra-molecular bond distances and angles (Table 6). In both dimers a further contraction in the Cu-Cu separation can be observed: from 2.939(3) Å to 2.914(3) Å for Cu1-Cu2 and 2.849(9) Å for Cu3-Cu4, with a concomitant modification of the Cu-O-Cu angle (99.7(7)° to 93.9(13)° and 94.0(7)°) seen for Cu3-O-Cu4, but not for Cu1-O-Cu2 (Table 6, Figure 10).

The loss of water sees a major re-arrangement of the atoms in the crystal lattice with the "vacant" site on Cu3 now occupied by the oxygen atom (Cu3···O14, 3.008(7) Å) of a perchlorate anion. Cu4 is in a distorted now octahedral geometry with the axial positions filled by a perchlorate O-atom (O33···Cu4, 2.964(12) Å) and a water O-

atom (O7···Cu4, 2.36(3) Å). The latter adopts a bent coordination mode to the metal centre with a Cu3-Cu4-O angle of just 67.4(6)°; the O33···Cu3 distance being just



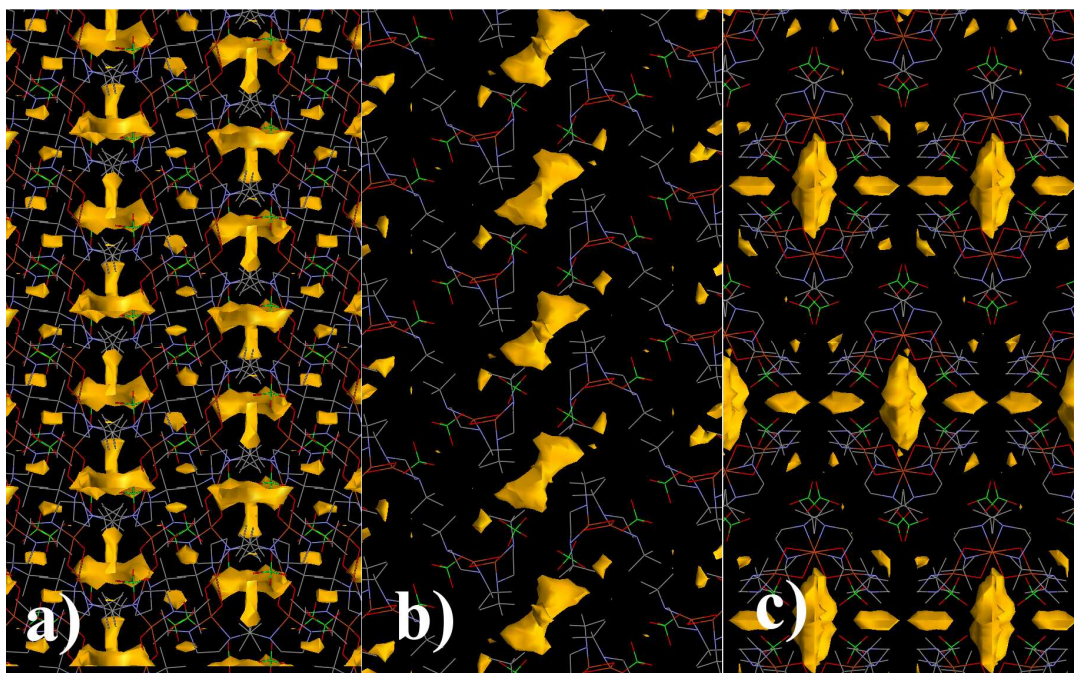**Figure 7** Void diagrams of **6** along the three crystallographic axes *a*, *b* and *c* at ambient pressure – Probe size: 0.8 Å.
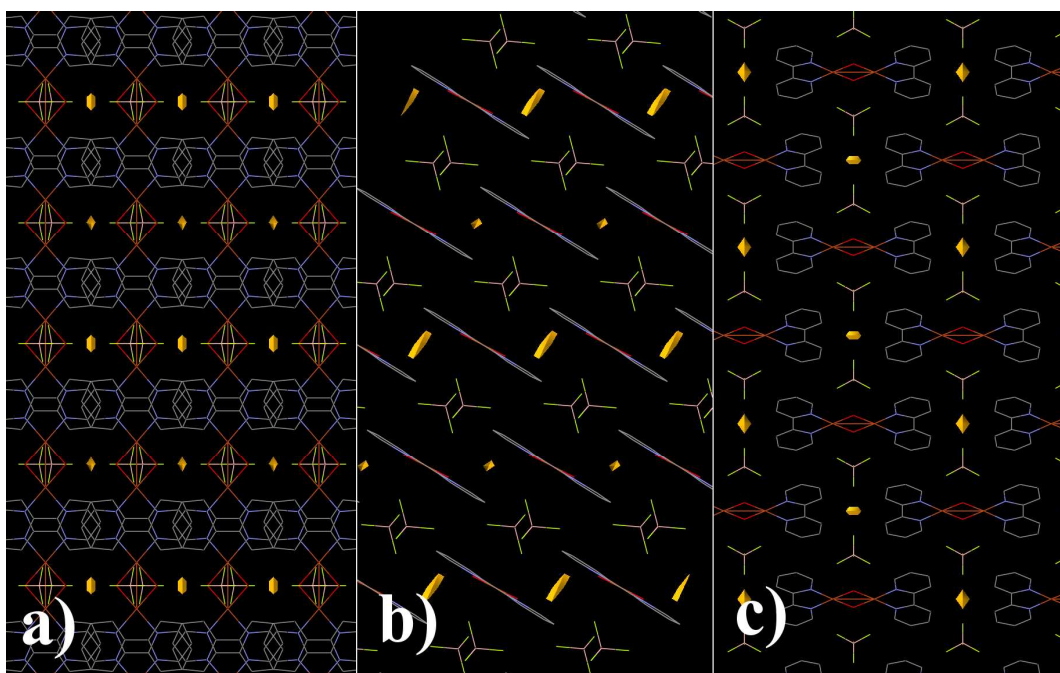


**Figure 8** Void diagrams of **7** along the three crystallographic axes *a*, *b* and *c* at ambient pressure – Probe size: 0.8 Å.

2.920Å. This effect can be partly attributed to the loss of planarity of the $[Cu_2O_2]$

unit with increasing pressure. The water molecule attached to Cu1 maintains its original alignment with respect to the Cu-Cu plane with increasing pressure, whilst that on Cu2 flips to an angle of 91.2(4)° (Table 6).

### 3.3.3 Effect of Pressure on the structures of 6 and 7

Compounds **6** and **7** are less affected by the application of pressure, but both still show significant structural modifications. As for **5** a compression of the unit cell (Tables 2, 3 and 4) is observed with increasing pressure. Using a probe of 0.8 Å, the void/volume ratio is approximately 13.4% of the total volume in **6** (Figure 7), and at

**Table 7** Bond distances and angles in **6** as a function of pressure.

| P (GPa) | Cu1-Cu2 | Cu1-O1 | Cu1-O2 | Cu1-N13 |
|---------|---------|--------|--------|---------|
| **0** | 2.9784(3) | 1.9045(13) | 1.9231(13) | 1.9987(15) |
| **0.21** | 2.964(3) | 1.887(12) | 1.891(9) | 2.001(11) |
| **0.9** | 2.908(7) | 1.85(3) | 1.915(17) | 1.97(2) |
| Δ/σ | 10 | 1.8 | 0.5 | 1.4 |
| **P (GPa)** | **Cu1-N16** | **Cu1-O5** | **Cu2-O1** | **Cu2-O2** |
| **0** | 2.0113(15) | 3.7202(17) | 1.9086(14) | 1.9198(12) |
| **0.21** | 1.994(18) | 3.877(15) | 1.893(8) | 1.910(12) |
| **0.9** | 1.99(4) | 3.88(2) | 1.968(18) | 1.77(3) |
| Δ/σ | 0.5 | 7.9 | 3.2 | 5 |
| **P (GPa)** | **Cu2-N5** | **Cu2-N8** | **Cu1-O6** | **Cu2-O7** |
| **0** | 2.0187(14) | 1.9973(16) | 4.0222(17) | 3.943(2) |
| **0.21** | 2.05(3) | 2.003(16) | 4.036(17) | 3.98(2) |
| **0.9** | 1.87(6) | 1.81(4) | 3.95(3) | 3.91(3) |
| Δ/σ | 2.5 | 4.6 | 2.4 | 0 |
| **P (GPa)** | **Cu2-O4** | **α1** | **α2** | **average α** |
| **0** | 4.1852(19) | 102.72(6) | 101.62(6) | 102.17(6) |
| **0.21** | 4.035(14) | 103.3(5) | 102.4(5) | 102.85(5) |
| **0.9** | 3.892(19) | 99.3(10) | 104.2(11) | 101.7(10) |
| Δ/σ | 15.3 | 3.4 | 2.3 | 0.5 |

0.9 GPa remains practically unchanged. For **7** the same probe reveals that the structure is more compact, with a void/volume ratio of approximately 1.5% of the total volume (Figure 8) at ambient conditions. At 4.7 GPa this "free space" has been completely removed. However, under pressure **6** shows small modifications in its intra-molecular geometry: the metal-metal distance contracts from 2.9784(3) Å at ambient pressure to 2.908(7) Å at 0.90 GPa (Table 7), with the two Cu-O-Cu bridging angles becoming more acute, decreasing from 102.72(6)° and 101.62(6)° to 99.3(10)° and 104.2(11)° at 0.90 GPa. Only one of the two Cu-O-Cu bridging angles

changes significantly; the second being within the "3σ rule". The shortening of the Cu-Cu distance is likely due to the contraction of the distances between Cu2 and one of the two bridging oxygens (OH ligands) that shorten from 1.9198(12) Å to 1.77(3) Å.

The structure of **7** is more "rigid" than **5** and **6**, due to the presence of the two $BF_4^-$ anions that form long contacts (~2.8 Å) at the axial sites of both the metal centres (Figure 2), making them pseudo six coordinate. This has the effect of "locking" the magnetic core in place somewhat, leaving less scope for pressure-induced distortion. This could also be the reason why crystals of **7** survived in the pressure cell up to 4.7 GPa, while those of **5** and **6** deteriorated at much lower pressures. However, as can

**Table 8** Bond distances and angles in **7** as a function of pressure.

| P (GPa) | Cu1-Cu2 | Cu1-O10 | Cu1-F1 | Cu1-N1 | α |
|---------|---------|---------|--------|--------|---|
| **0** | 2.8663(17) | 1.908(2) | 2.775(2) | 1.982(3) | 97.40(14) |
| **0.3** | 2.8689(17) | 1.910(2) | 2.768(3) | 1.980(3) | 97.37(17) |
| **0.8** | 2.8649(14) | 1.911(2) | 2.711(2) | 1.984(3) | 97.13(14) |
| **1.53** | 2.8544(12) | 1.9069(19) | 2.655(2) | 1.978(3) | 96.91(13) |
| **2.25** | 2.8427(15) | 1.908(2) | 2.609(3) | 1.970(3) | 96.33(16) |
| **2.8** | 2.8422(12) | 1.907(2) | 2.577(2) | 1.976(3) | 96.35(14) |
| **3.5** | 2.8331(13) | 1.914(2) | 2.548(2) | 1.972(3) | 95.49(14) |
| **4** | 2.8313(14) | 1.913(3) | 2.530(3) | 1.968(4) | 95.45(18) |
| **4.3** | 2.8374(17) | 1.920(3) | 2.543(4) | 1.980(5) | 95.3(2) |
| **4.7** | 2.8210(19) | 1.904(3) | 2.503(3) | 1.964(4) | 95.6(2) |
| Δ/σ | 17.9 | 0 | 75.4 | 3.6 | 7.2 |

be seen from Table 7, the Cu-F distances decrease from 2.775(2) Å at ambient conditions to 2.503(3) Å at 4.7 GPa. The Cu-Cu separation is compressed from 2.8663(17) Å to 2.8210(19) Å (Table 8), with a concomitant decrease in the Cu-O-Cu bridging angles, from 97.40(14)° at room pressure to 95.6(2)° at the highest pressure measured.

### 3.3.4 *Effect of Pressure on the Magnetism of 5-7*

Variable temperature magnetic susceptibility data were collected on **5-7** in the temperature range 350-20 K in an applied field of 1 kOe (Figures 9-11) at ambient and three different pressures.

The magnetic behaviour of **5** under ambient pressure has been described in detail previously,[2] while **6** and **7** behave very similarly to their $BF_4^-$ and $ClO_4^-$ analogues,

respectively.[2, 25] Simulations of the susceptibility data (Figures 9-11) using the Hamiltonian expressed in Eqn (1) reveal strong antiferromagnetic exchange in **5** ($J = -260$ cm$^{-1}$), **6** ($J = -252$ cm$^{-1}$) and weak ferromagnetic exchange in **7** ($J = +22$ cm$^{-1}$).

$$\hat{H} = -2J\left(\hat{S}_1 \cdot \hat{S}_2\right) \qquad (1)$$

At all pressures and low temperatures (T $\leq$ 90 K) the $\chi_M T$ values of **5** and **6** are 0 cm$^3$



**Figure 9** Plots of $\chi_M T$ versus T for **5** recorded in the 350-20 K temperature range at the indicated pressures; the solid lines represent simulations of the data.
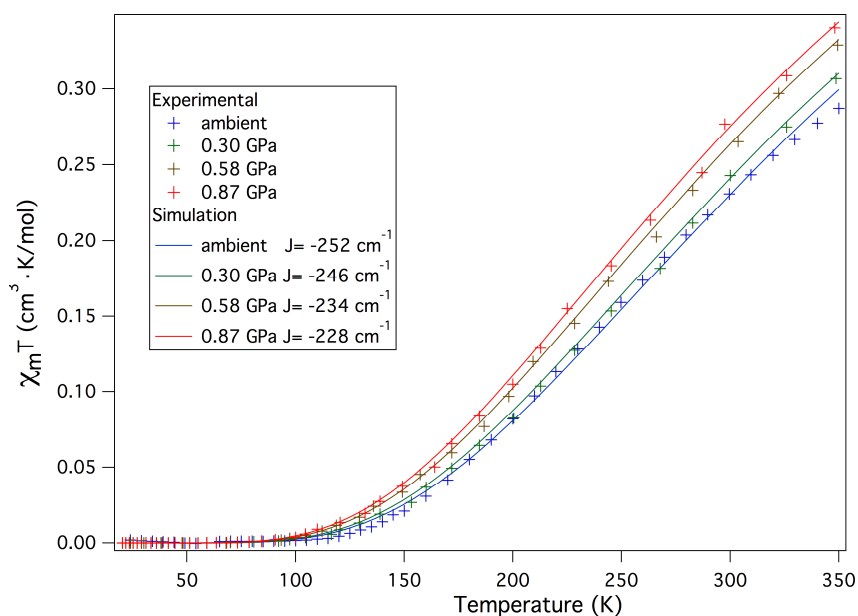


**Figure 10** Plots of $\chi_M T$ versus T for **6** recorded in the 350-20 K temperature range at the indicated pressures; the solid lines represent simulations of the data.

K mol$^{-1}$, indicative of diamagnetic ground states. As the temperature increases (T $\geq$ 90 K) the value of $\chi_M$T increases, following different paths as a function of the applied pressure to a value of approximately 0.28 cm$^3$ K mol$^{-1}$ at 350 K and ambient pressure, 0.35 cm$^3$ K mol$^{-1}$ at 0.22 GPa, 0.35 cm$^3$ K mol$^{-1}$ at 0.59 GPa and 0.39 cm$^3$ K mol$^{-1}$ at 0.84 GPa for **5**. For **6** a similar trend is found, with values of approximately 0.28 cm$^3$ K mol$^{-1}$ at ambient pressure, 0.30 cm$^3$ K mol$^{-1}$ at 0.30 GPa, 0.33 cm$^3$ K mol$^{-1}$ at 0.58 GPa and 0.34 cm$^3$ K mol$^{-1}$ at 0.87 GPa. This behaviour is a clear indication that the antiferromagnetic interaction between the metal centres is weakened by the application of pressure. Although the background of the pressure cell used in our experiments and the weak signal coming from samples do not permit to treat the data in a rigorously quantitative manner, it is still possible to interpret the trends in a qualitative fashion to extract some conclusions. Indeed it is also important to point out that the pressure within the cell changes with changing temperature - we expect a drop of the order of ~0.2 GPa between 350 and 20 K.[22] The parameters obtained from the simulations of high pressure data for **5** and **6** are summarised in Table 9 and confirm the weakening of the antiferromangnetic interaction in both cases. Between ambient pressure and 0.84 GPa the *J* value changes from -260 cm$^{-1}$ to -203 cm$^{-1}$ for **5** and from -252 cm$^{-1}$ to -228 cm$^{-1}$ for **6**.

High pressure susceptibility measurements on **7** are shown in Figure 11 and show a constant increase in the value of $\chi_M$T with pressure for a given temperature. At 350
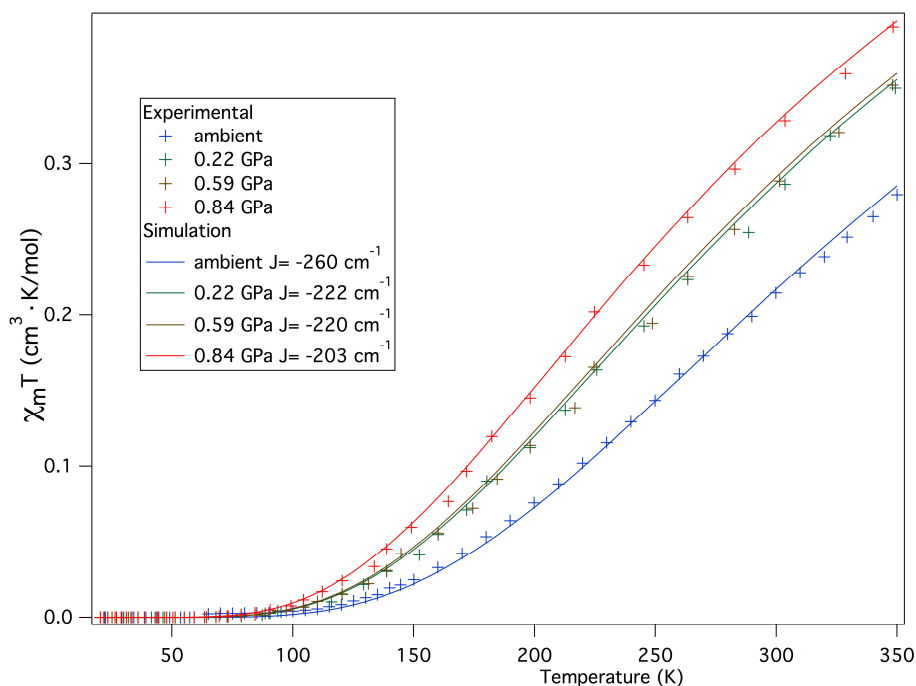


**Figure 11** Plots of $\chi_M$T versus T for **7** recorded in the 350-20 K temperature range at the indicated pressures; the solid lines represent simulations of the data.
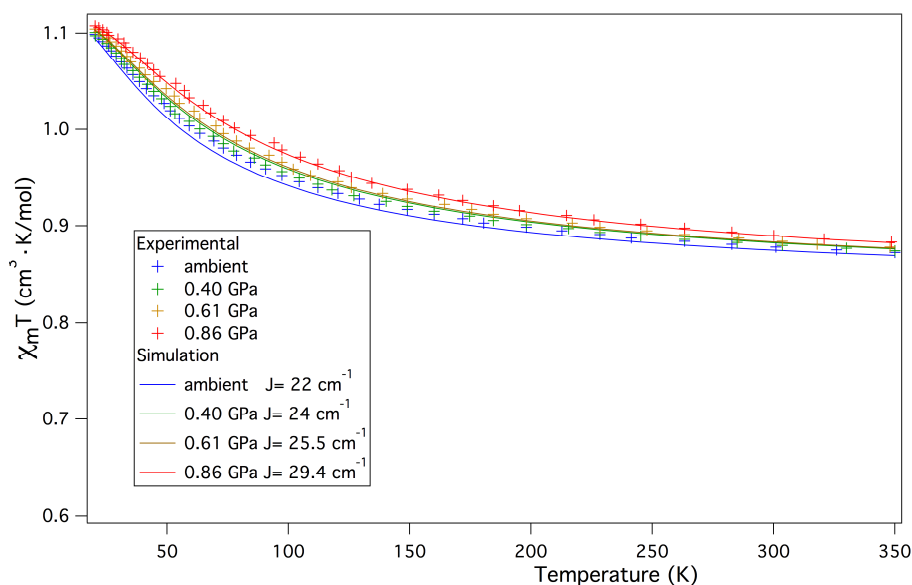
K the value of $\chi_M T$ is 0.88 cm$^3$ K mol$^{-1}$ at ambient pressure, rising to a maximum of 1.1 cm$^3$ K mol$^{-1}$ at 20 K; at 0.86 GPa $\chi_M T$ increases from 0.89 cm$^3$ K mol$^{-1}$ at 350 K to 1.12 cm$^3$ K mol$^{-1}$ at 20 K. This trend is an indication that the ferromagnetic interaction between the metal centres is strengthened by the increasing pressure, albeit only moderately. Parameters obtained from the simulations of the high pressure data are summarised in Table 9: at 0.84 GPa the *J* value increases from 22 cm$^{-1}$ to 29.4 cm$^{-1}$.

For this specific family of compounds a useful relationship between the Cu-O-Cu bridging angle ($\alpha$) and the nature and strength of magnetic interaction, shown in Eqn (2) has been postulated:[2]

$$J = -74.53 \cdot \alpha + 7270 \ cm^{-1} \tag{2}$$

The predictions of Eqn (2) and the experimental observations at ambient conditions are in good qualitative agreement, with **5** and **6** displaying strong antiferromagnetic interactions and **7** exibiting weak ferromagnetic exchange. The application of

**Table 9** Comparison of the *J* values as function of pressure for complexes **5**, **6** and **7** – *g*= 2.09 for **5** and **6**; *g*= 2.11 for **7**.

| **5** | | **6** | | **7** | |
|---|---|---|---|---|---|
| **P (GPa)** | **J/cm$^{-1}$** | **P (GPa)** | **J/cm$^{-1}$** | **P (GPa)** | **J/cm$^{-1}$** |
| **ambient** | -260 | **ambient** | -252 | **ambient** | 22 |
| **0.22** | -222 | **0.22** | -246 | **0.22** | 24 |
| **0.59** | -220 | **0.59** | -234 | **0.59** | 25.5 |
| **0.84** | -203 | **0.84** | -228 | **0.84** | 29.4 |

pressure causes a decrease in the antiferromagnetic *J* value for **5** and **6** (Figure 9, Figure 10 and Table 9): for **5** this trend, agrees with the crystallographic findings that show a reduction in the bridging angle $\alpha$, the Cu-O distances unchanged and a shortening of the Cu-Cu distance. The high pressure magnetic behaviour of **6** cannot be explained using Eqn (2) because of crystallographic uncertainty. However, calculations have predicted that a reduction in the antiferromagnetic coupling constant can also be caused by a contraction of Cu-O distances.[8] For compound **6** such compression occur quite signifincantly for one Cu-O distance in the molecule. Qualitatively therefore, we can say that the magnetic behaviour of **6** is again in agreement with previous predictions. The slight increase in the ferromagnetic

exchange in **7** (Figure 11, Table 9) is also consistent with the crystallographic observation of decreasing Cu-O-Cu bridging angle, and thus Eqn (2).

Interestingly between 1.20 GPa and 2.50 GPa, **5** undergoes a phase transition that drastically twists the $[Cu_2O_2]$ core unit of the molecule and forces two of the Cu-O-Cu angles (O3, O4) to drop below the value of 97.5° expected to afford ferromagnetic exchange. The observation of this, potentially exciting, pressure-induced AF→F switch is however hindered by two factors: a) the second molecule in the lattice has Cu-O-Cu angles greater than 97.5° (AF exchange) and thus what we observe experimentally is an average of the two; and b) we are limited by technology because our SQUID pressure cell could reach a maximum pressure of only 0.87 GPa - below the pressure of the crystallographic phase transition.

## 3.4 Conclusions

This chapter has presented the use of high pressure magnetometry and single-crystal X-ray crystallography to study three dinuclear hydroxo-bridged copper(II) complexes. Under the effects of hydrostatic pressure the metallic core, and in particular the Cu-O-Cu angle, in all the three dimers is significantly distorted. **5** undergoes a phase transition between 1.20 and 2.50 GPa, switching from space group $P2_1/c$ to $P\bar{1}$ with the loss of a coordinated water molecule and severe structural distortion. In one of the two independent molecules the Cu-O-Cu bridging angles fall below the value expected to instigate ferromagnetic exchange. In all three complexes the observed structural distortions affect the magnetic behaviour: dc susceptibility measurements have shown a decrease in the antiferromagnetic exchange for **5** and **6** and an increase of the ferromagnetic exchange for **7**, with increasing pressure. The overall findings of this work are consistent with the reported magneto-structural correlations at ambient pressure. While previous papers have demonstrated this validity via chemical modification of the magnetic cores, this work proves that the same phenomena can be observed by the application of "external" hydrostatic pressure.

## 3.5  References

1.      B. Bleaney and K. D. Bowers, *Proc. Roy. Soc. London*, 1952, **A214**, 451.
2.      V. H. Crawford, H. W. Richardson, J. R. Wasson, D. J. Hodgson and W. E. Hatfield, *Inorg. Chem.*, 1976, **15**, 2107.
3.      D. Gatteschi, O. Kahn and R. D. Willet, *Magneto Structural Correlation in Exchange Coupled Systems*, Reidel, D., Dordrecht, 1985.
4.      W. E. Hatfield, *Inorg. Chem.*, 1983, **22**, 833.
5.      P. J. Hay, J. C. Thibeault and R. Hoffmann, *J. Am. Chem. Soc.*, 1975, **97**, 4884.
6.      D. Gatteschi, O. Kahn, J. S. Miller and F. Palacio, *Magnetic Molecular Materials*, Kluwer Academic, Dordrecht, The Netherlands, 1991.
7.      E. Ruiz, P. Alemany, S. Alvarez and J. Cano, *J. Am. Chem. Soc.*, 1997, **119**, 1297.
8.      E. Ruiz, P. Alemany, S. Alvarez and J. Cano, *Inorg. Chem.*, 1997, **36**, 3683.
9.      O. Castell, R. Caballol, V. M. Garcìa and K. Handrick, *Inorg. Chem.*, 1996, **35**, 1609.
10.     L. Merrill and W. A. Bassett, *Rev. Sci. Instrum.*, 1974, **45**, 290.
11.     S. A. Moggach, D. R. Allan, S. Parsons and J. E. Warren, *J. Appl. Crystallogr.*, 2008, **41**, 249.
12.     G. J. Piermarini, S. Block, J. D. Barnett and R. A. Forman, *J. Appl. Phys.*, 1975, **46**, 2774.
13.     Bruker-Nonius, *APEX-ll, Version V1*, (2004), Madison, Wisconsin, USA.
14.     D. R. Allan, S. Parsons and S. J. Teat, *J. Synchr. Rad.*, 2001, **8**, 10.
15.     Bruker-Nonius, *SAINT version 7*, (2006) Bruker-AXS, Madison, Wisconsin, USA.
16.     G. M. Sheldrick, *SADABS Version 2004-1*, (2004) Bruker-AXS, Madison, WIsconsin, USA.
17.     S. Parsons, *S.SHADE*, (2004) The University of Edinburgh, Edinburgh, United Kingdom.
18.     D. J. Watkin, K. Prout, J. R. Carruthers, P. W. Betteridge and R. I. Cooper, *CRYSTALS Issue 12*, (2003) Chemical Crystallography Laboratory, University of Oxford, Oxford, UK.
19.     A. L. Spek, *PLATON- A multipurpose Crystallographic Tool*, (2004) Utrecht University, Utrecht, The Netherlands.
20.     C. F. Macrae, I. J. Bruno, J. A. Chisholm, P. R. Edgington, P. McCabe, E. Pidcock, L. Rodriguez-Monge, R. Taylor, J. Van de Streek and P. A. Wood, *J. Appl. Cryst.*, 2008, **41**, 466.
21.     K. Brandenburg and H. Putz, *DIAMOND*, (2005) Crystal Impact, Bonn, Germany.
22.     K. V. Kamenev, S. Tancharakorn, N. Robertson and A. Harrison, *Rev. Sci. Instrum.*, 2006, **77**, 073905.
23.     J. J. Borrás-Almenar, J. M. Clemente-Juan, E. Coronado and B. S. Tsukerblat, *J. Comput. Chem.*, 2001, **22**, 985.
24.     A. W. Addison, T. N. Rao, J. Reedijk, J. Van Rijn and G. C. Verschoor, *J. Chem. Soc., Dalton Trans*, 1984, 1349.

25.    L. M. Mirica, D. J. Rudd, M. A. Vance, E. I. Solomon, K. O. Hodgson, B. Hedman and T. D. P. Stack, *J. Am. Chem. Soc.*, 2006, **128**, 2654.

# Chapter 4

# The Effect of Pressure on

# Oxo-bridged Mixed-valent

# Manganese Dimers

## 4.1  Introduction

Despite the availability of these exciting new tools, and to the best of our knowledge, there are only a handful of studies that combine high pressure single crystal X-ray diffraction and high pressure SQUID magnetometry.[1-5] These reports demonstrate that by the application of pressure it is possible to distort intra-molecular bond lengths and angles significantly and that these structural changes are manifested in a concomitant change in the magnetic behaviour. In this paper we focus our high-pressure study on two two mixed-valent oxo-bridged $Mn^{III}/Mn^{IV}$ dimers, a family of compounds that has attracted interest from both a magnetic and biological viewpoint.[6]

## 4.2  Experimental section

### 4.2.1  Syntheses

All reactions were carried out in aerobic conditions using materials as received with no further purifications. $[Mn_2O_2(bpy)_4][ClO_4]_3 \cdot 3CH_3CN$ (**8**·3CH$_3$CN) and $[Mn_2O_2(bpy)_4][PF_6]_3 \cdot 2CH_3CN \cdot H_2O$ (**9**·2CH$_3$CN·H$_2$O) were made as previously described.[7]

**General method:** a solution of 4.3 g $Mn(OAc)_2.4H_2O$ (OAc = $CH_3COO^-$) (17.5 mmol) in 60 mL of $H_2O$ was added to 8.2 g of 2,2'-bipyridyl (52.5 mmol) in 30 mL of acetone with stirring. 80 mL of 1 M acetate buffer (pH 5) was then added to the yellow solution, followed by 1.18 g of $KMnO_4$ (7.5 mmol) in 50 mL of $H_2O$. The resulting green solution was stirred for 15 min before $NaClO_4$ (4.5 g, 36.8 mmol) for **8**, or $NH_4PF_6$ for **9** (6.0 g, 36.5 mmol), was added to precipitate the product as a green powder. The product was first washed with ethanol and diethyl ether, and then recrystallized from acetonitrile to give brown-green crystals. Anal. Calcd. (found) for **8**, $C_{46}H_{41}Cl_3Mn_2N_{11}O_{14}$: C, 46.50 (46.23); H, 3.48 (3.28); Cl, 8.95 (9.03); Mn, 9.25 (9.20); N, 12.97 (12.84). Anal. Calcd. (found) for **9**, $C_{44}H_{40}F_{12}Mn_2N_{10}O_3P_3$: C, 44.50 (44.12); H, 3.39 (3.26); F, 19.20 (19.33); Mn, 9.25 (9.29); N, 11.79 (11.88); P, 7.82 (7.96).

## 4.2.2 X-ray crystallography

High-pressure single crystal experiments were carried out using a Merrill-Bassett diamond anvil cell (half-opening angle 40°),[8] equipped with Boehler-Almax diamonds with 600 μm culets and a tungsten gasket.[9] Petroleum ether was used as hydrostatic medium for all the compounds and a small ruby chip was loaded into the cell as the pressure calibrant with the ruby fluorescence used to measure the pressure.[10] Diffraction data were collected using synchrotron radiation of wavelength λ = 0.4865 Å for **8**, 0.4763 Å for **9** all at room temperature on a Bruker Smart APEX II[11] diffractometer on Station 9.8 at SRS, Daresbury Laboratory.[12] Data collection and processing procedures followed the procedures established by Dawson *et al.*[13] Integrations were carried out using the program Saint[14] and absorption corrections with the program Sadabs[15] and Shade.[16] A key step in improving the data fitting in the structures of **2**·2CH$_3$CN·1H$_2$O was masking of the gasket lines and the use of robust-resistant weighting during data merging.[17] Data collections were taken at 0.18, 1.00 and 2.00 GPa for **8**, at 0.45, 1.23, 1.75, 3.00 and 4.55 GPa for **9**·2CH$_3$CN·1H$_2$O. Refinements of the compressed form of **8** and **9**·2CH$_3$CN·1H$_2$O were carried out starting from the coordinates obtained from a separate data collection carried out under ambient pressure and T = 150 K using Mo-Kα radiation on a Bruker Smart diffractometer.[18] The anomalous scattering factors and mass absorption coefficients were calculated with WinGX.[19] The program Crystals[20] was used to refine the structures against *F* using all reflections with $I > 2\sigma(I)$).

In the ambient pressure refinement of **8** the perchlorate anion based on Cl58/Cl63 is disordered in the ratio 60:40 over two orientations that share a common plane of three O-atoms. The third anion, based on Cl55 was modelled with one ordered Cl-O axis, whilst the remaining three oxygen atoms disordered over three different orientations in the 45:35:20 ratio that were restrained to be tetrahedral.

Due to the low completeness of the high-pressure data sets, the aromatic rings in **8** were treated as rigid bodies. All the perchlorate anions in **8** were ordered at high pressure, but tetrahedral restraints were applied. With the exception of Cl and Mn, all atoms were refined isotropically.

In **9**·2CH$_3$CN·1H$_2$O all non-H atoms were modelled with anisotropic displacement parameters. Similarity restraints were applied to chemically equivalent bond

distances and angles of the bpys ligands and $PF_6$ anions . At ambient pressure it was possible to model one molecule of $CH_3CH$ explicitly with the remaining solvent being treated with the Squeeze routine.[21] All the solvent was modeled using Squeeze in the high-pressure refinements.

Refinement parameters are reported in Tables 1 and 2. Void diagrams were calculated[22] and visualised with Mercury.[23, 24]

**Table 1** Crystallographic data for **8** at ambient, 0.18, 1.00, and 2.00 GPa.

| [Mn₂O₂(bipy)₄][ClO₄]₃·3[CH₃CN] – 8 | | | | |
|---|---|---|---|---|
| **Pressure** | **ambient** | **0.18 GPa** | **1.00 GPa** | **2.00 GPa** |
| T (K) | 150 | 300 | 300 | 300 |
| Spacegroup | $P\bar{1}$ | $P\bar{1}$ | $P\bar{1}$ | $P\bar{1}$ |
| $a$, | 13.2108 (2), | 13.2520 (8), | 12.969 (3), | 12.657 (4), |
| $b$, | 13.7331 (3), | 13.8270 (8), | 13.5755 (14), | 13.394 (2), |
| $c$ (Å) | 16.0434 (3) | 16.0093 (11) | 15.7245 (14) | 15.538 (3) |
| $\alpha$, | 65.4150 (10), | 65.446 (5), | 64.279 (5), | 63.47 (1), |
| $\beta$, | 72.0270 (10), | 71.915 (6), | 72.026 (7), | 71.93 (1), |
| $\gamma$ (º) | 83.1960 (10) | 83.172 (4) | 83.282 (8) | 83.66 (2) |
| $V$ (Å³) | 2517.49 (9) | 2536.2 (3) | 2372.0 (6) | 2239.1 (11) |
| Radiation, $\lambda$ (Å) | Mo $K\alpha$ | Synchrotron, 0.48650 | Synchrotron, 0.48650 | Synchrotron, 0.48650 |
| $\mu$ (mm⁻¹) | 0.74 | 0.2 | 0.2 | 0.3 |
| Crystal size (mm) | 0.23 × 0.18 × 0.11 | 0.14 × 0.12 × 0.08 | 0.14 × 0.12 × 0.08 | 0.14 × 0.12 × 0.08 |
| $T_{min}$, $T_{max}$ | 0.59, 0.92 | 0.34, 0.94 | 0.53, 0.94 | 0.14, 0.94 |
| Refinement Criterion for observed reflections | $F$ $I > 2.0\sigma(I)$ | $F$ $I > 2.0\sigma(I)$ | $F$ $I > 2.0\sigma(I)$ | $F$ $I > 2.0\sigma(I)$ |
| Measured, independent observed reflections | 76562, 14287, 10940 | 15556, 4212, 2355 | 11178, 2959, 1766 | 10855, 2769, 1519 |
| $R_{int}$ | 0.037 | 0.093 | 0.071 | 0.110 |
| $\theta_{max}$ (º) | 30.0 | 17.7 | 15.7 | 15.7 |
| R, wR, S | 0.050, 0.052, 1.16 | 0.093, 0.068, 1.00 | 0.086, 0.049, 1.00 | 0.098, 0.068, 0.99 |
| Reflections | 10940 | 2355 | 1766 | 1519 |
| Parameters | 712 | 225 | 225 | 225 |
| Restraints | 3 | 42 | 45 | 45 |
| $\Delta\rho_{max}$, $\Delta\rho_{min}$ | 1.09, -1.08 (eÅ⁻³) | 0.59, -0.38 (eÅ⁻³) | 0.55, -0.49 (eÅ⁻³) | 0.52, -0.43 (eÅ⁻³) |

### 4.2.3 Magnetic measurements.

Variable temperature dc magnetic susceptibility measurements were made on a Quantum Design Magnetic Property Measurement System (SQUID magnetometer)

equipped with a 7T magnet operating in the 350-20 K temperature range. Diamagnetic corrections were applied using Pascal's constants. For the high-pressure magnetic measurements a cell of piston-cylinder design was used.[25] Data were collected at 0.32, 0.54 and 0.87 GPa for **8** and at 0.36, 0.58, 0.84 GPa for **9**.

# 4.3   Results and Discussion

## 4.3.1   Description of Structures

**Table 2** Crystallographic data for **9**·2CH$_3$CN·1H$_2$O at ambient, 0.45, 1.23, 1.75, 3.00 and 4.55 GPa.

| | 9·2CH$_3$CN·1H$_2$O | | | | | |
|---|---|---|---|---|---|---|
| **Pressure** | **ambient** | **0.45 GPa** | **1.23 GPa** | **1.75 GPa** | **3.00 GPa** | **4.55 GPa** |
| T (K) | 150 | 300 | 300 | 300 | 300 | 300 |
| Spacegroup | $P2_1/n$ | $P2_1/n$ | $P2_1/n$ | $P2_1/n$ | $P2_1/n$ | $P2_1/n$ |
| $a, b, c$ (Å) | 13.3430(3) 21.7678(5) 18.2512(4) | 13.3300(4) 21.746(1) 18.0899(9) | 12.9086(5) 21.526(2) 17.521(1) | 12.7539(5) 21.435(1) 17.328(1) | 12.4580(6) 21.262(2) 16.954(2) | 12.2052 (6), 21.026 (2) 16.620 (2) |
| β (º) | 103.675(1) | 103.272(3) | 101.683(4) | 101.105(5) | 100.128(5) | 99.439(5) |
| $V$ (Å$^3$) | 5150.7(2) | 5103.7(4) | 4766.6(5) | 4648.5(5) | 4420.8(6) | 4207.5(6) |
| Radiation, λ (Å) | Mo $K\alpha$ | Synchrotron, 0.48630 | Synchrotron, 0.48630 | Synchrotron, 0.48630 | Synchrotron, 0.48630 | Synchrotron, 0.48630 |
| μ (mm$^{-1}$) | 0.7 | 0.2 | 0.2 | 0.2 | 0.2 | 0.3 |
| Crystal size (mm) | 0.22 × 0.18 × 0.12 | 0.14 × 0.13 × 0.09 | 0.14 × 0.13 × 0.09 | 0.14 × 0.13 × 0.09 | 0.14 × 0.13 × 0.09 | 0.14 × 0.13 × 0.09 |
| $T_{min}, T_{max}$ | 0.65, 0.92 | 0.21, 0.94 | 0.29, 0.94 | 0.34, 0.93 | 0.33, 0.93 | 0.75, 0.93 |
| Refinement Criterion for observed reflections | $F$ $I > 2.0\sigma(I)$ | $F$ $I > 2.0\sigma(I)$ | $F$ $I > 2.0\sigma(I)$ | $F$ $I > 2.0\sigma(I)$ | $F$ $I > 2.0\sigma(I)$ | $F$ $I > 2.0\sigma(I)$ |
| Measured, independent, observed reflections | 62474, 2766, 7366 | 18747, 5257, 2512 | 17707, 4928, 2285 | 14441, 4766, 2131 | 15093, 4469, 1778 | 10746, 3352, 1104 |
| $R_{int}$ | 0.061 | 0.100 | 0.101 | 0.092 | 0.125 | 0.120 |
| $\theta_{max}$ (º) | 28.9 | 15.7 | 15.9 | 15.7 | 15.7 | 15.8 |
| $R, wR, S$ | 0.051, 0.060, 0.93 | 0.076, 0.065, 0.99 | 0.067, 0.055, 1.00 | 0.061, 0.046, 1.00 | 0.078, 0.080, 1.02 | 0.079, 0.078, 1.10 |
| Reflections | 7366 | 2512 | 2285 | 2131 | 1778 | 1104 |
| Parameters | 670 | 312 | 322 | 322 | 322 | 217 |
| Restraints | 1 | 0 | 0 | 1 | 318 | 193 |
| $\Delta\rho_{max}, \Delta\rho_{min}$ | 1.14, -0.77 | 0.47, -0.32 | 0.47, -0.35 | 0.49, -0.35 | 0.68, -0.68 | 0.65, -0.62 |

Compound **8** has been previously reported in a monoclinic spacegroup and with different solvent molecules in the structure.[26] The structures of **8** and **9**·2CH$_3$CN·1H$_2$O are analogous (Figure 1), containing a central mixed-valent

[Mn$^{III}$Mn$^{IV}$O$_2$] asymmetric rhomb of two Mn ions bridged by two μ-O$^{2-}$ ligands. Two bpy ligands fulfill the octahedral coordination around each Mn atom, with charge balance maintained by the presence of three [ClO$_4$]$^-$ ions (**8**), or three [PF$_6$]$^-$ ions (**9·2CH$_3$CN·1H$_2$O**). Bond length considerations and BVS calculations reveal Mn1 to be 3+ and Mn2 to be 4+ (Tables 3-6). In each case the Jahn-Teller axis of the Mn$^{3+}$ ion is defined by the N41-Mn1-N29 vector which is approximately perpendicular to the [Mn$_2$O$_2$] plane. The Mn-Mn separation and the O-Mn-O bridging angles are 2.7057(6) Å, 96.41(10)° and 96.02(10)° in **8** and 2.7177 Å, 97.00(11)° and 96.97(11)° in **9·2CH$_3$CN·1H$_2$O**.

There are three CH$_3$CN molecules of solvation per dimer in the crystal of **8,** and two
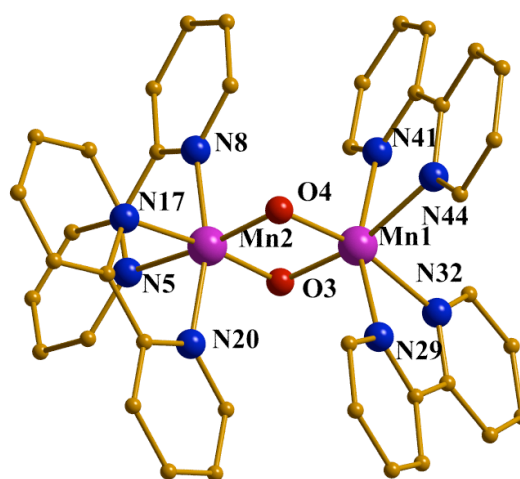


**Figure 1** The molecular structure of **8** and **9** – Colour scheme: Mn = violet, C = gold, O = red, N = blue, Cl = green, F = turquoise and P = grey. H atoms, counter ions and solvent molecules are omitted for clarity.
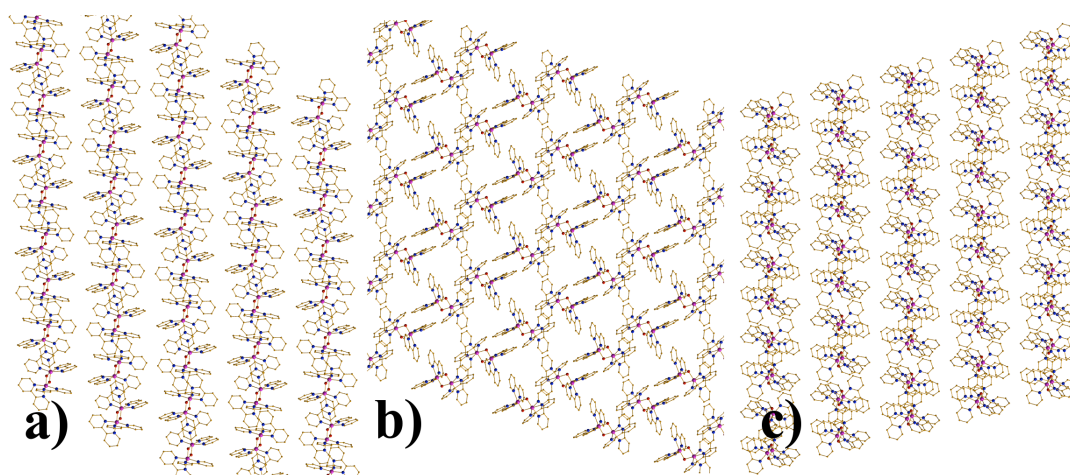


**Figure 2** Packing diagrams of **8** along the three crystallographic axes *a*, *b* and *c*.

$CH_3CN$ and one $H_2O$ molecule in the crystal of $\mathbf{9}\cdot 2CH_3CN\cdot 1H_2O$. In each case the solvent molecules and anions are H-bonded to the protons of the bpy rings at distances of approximately 2.6 Å, with the closest inter-cluster interactions being between staggered π-π stacked bpy rings at approximately 3.6 Å (C···C). Packing diagrams illustrating the views along the three crystallographic axes are shown in Figures 2 and 3.
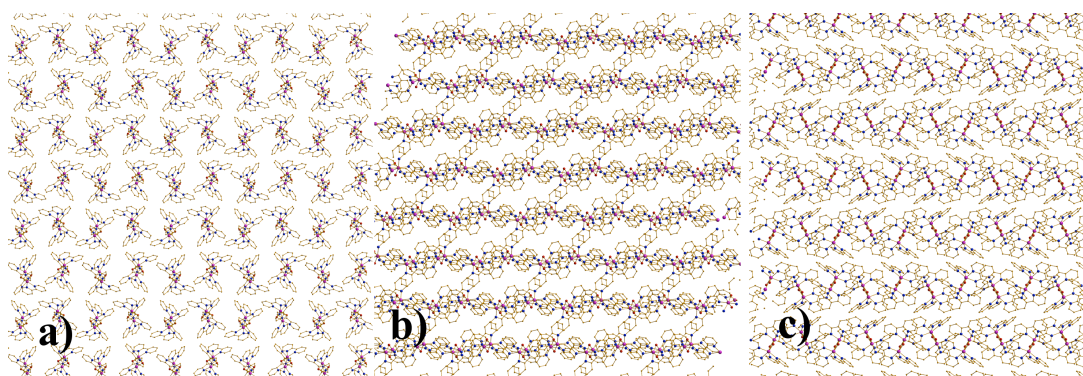


**Figure 3** Packing diagrams of **9** along the three crystallographic axes *a*, *b* and *c*.

**Table 3** SQUEEZE results for $\mathbf{9}\cdot 2CH_3CN\cdot 1H_2O$ as function of pressure.

| Pressure, GPa | Vol/Å$^3$ | N° e$^-$/cell | Asymmetric unit modeled after SQUEEZE applied |
|---|---|---|---|
| 0 | 504 | 125 | $\mathbf{9}\cdot 1CH_3CN$ |
| 0.45 | 844 | 130 | **9** |
| 1.23 | 701 | 136 | **9** |
| 1.75 | 648 | 126 | **9** |
| 3.00 | 564 | 164 | **9** |
| 4.55 | 476 | 162 | **9** |

## 4.3.2 Refinement of the high-pressure crystal structures

Although it was possible to refine compound **8** with all three solvent molecules at every pressure, the same could not be achieved for $\mathbf{9}\cdot 2CH_3CN\cdot 1H_2O$, and the Squeeze[21] routine was used to treat one $CH_3CN$ molecule and the water molecule at ambient pressure and all the solvent at high pressure. The input to the Squeeze procedure consists of the ordered part of the structure; voids in the ordered model are located, and an electron density synthesis calculated in these void regions. The electron density found is back transformed into 'solvent' contributions to the structure factors. The results of the Squeeze calculations are reported in Table 3,

which lists the volume of the solvent region and number of electrons (per cell) treated by the procedure.

The solvent in the crystal structure of **9**·2CH$_3$CN·1H$_2$O was badly disordered (even at high pressure) and little progress could be made during refinement using partial-



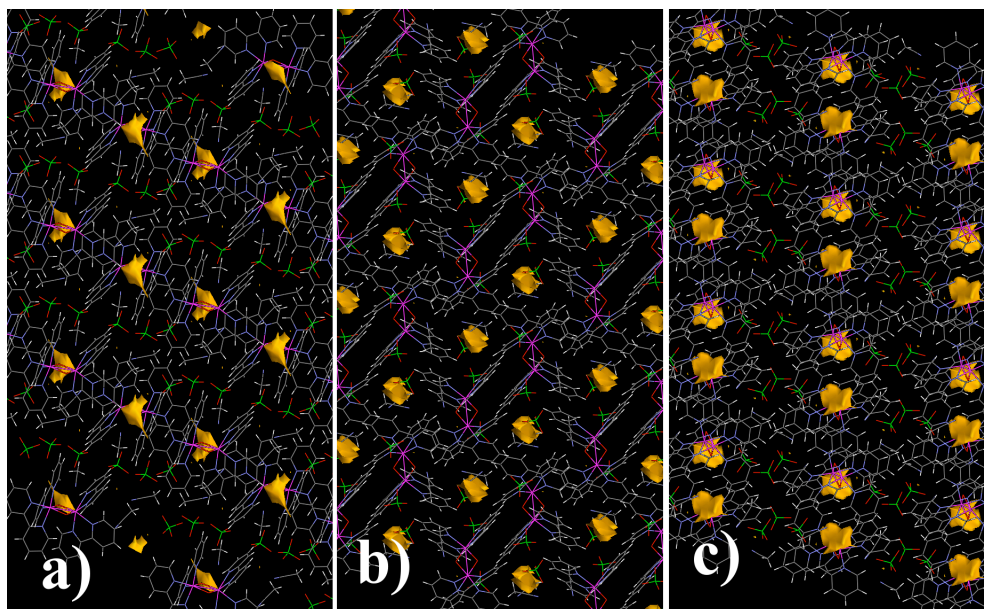**Figure 4** Void diagrams of **8** along the three crystallographic axes *a*, *b* and *c* at 0.18 GPa – Probe size: 0.8 Å.
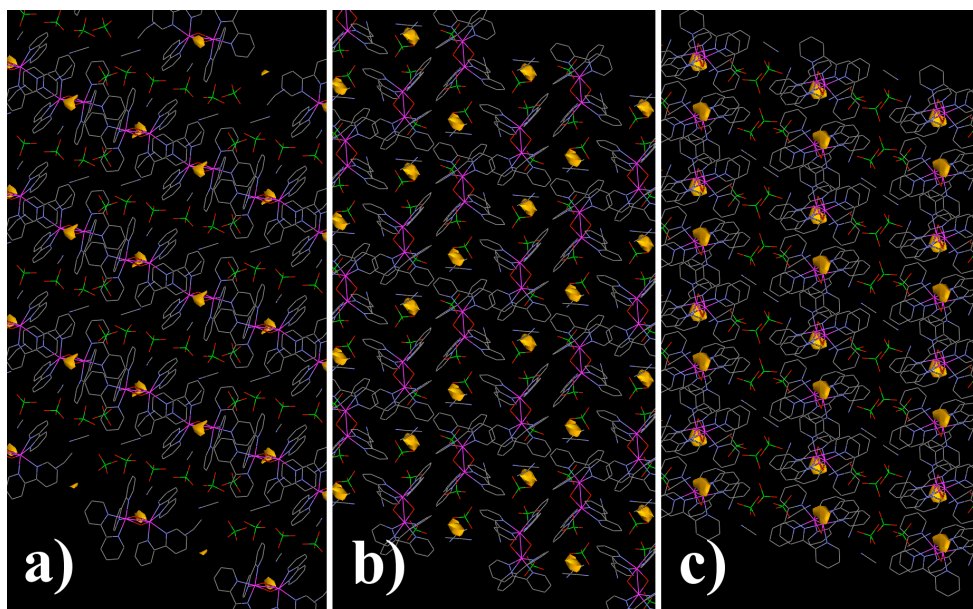


**Figure 5** Void diagrams of **8** along the three crystallographic axes *a*, *b* and *c* at 2.00 GPa – Probe size: 0.8 Å.

occupancy atomic models. However, the Squeeze routine is based on a Fourier transformation, and this will be distorted if a data set is not complete. For this

reason the Squeeze routine can be unstable when used with high-pressure data, since the pressure cell body results in shading of the diffraction pattern, leading to data sets of low completeness. The data in Table 3 illustrate some of the disadvantages of using the Squeeze routine with high-pressure data. The volume of the solvent void treated in the ambient pressure refinement was larger than in the high-pressure refinements because one MeCN molecule was modelled explicitly. Nevertheless the electron count is similar at ambient pressure and 0.45 GPa whereas it should be bigger to account for the extra MeCN molecules per cell now being treated using Squeeze. Rather than indicating that some solvent is being pushed out of the crystal as pressure increases, the most likely explanation for this is that the electron density integration is biased by the low completeness (ca. 53% on average) of the high-pressure data collections. This being said, the high-pressure data sets all have similar completeness, with the same region of reciprocal space being sampled for every pressure. It seems reasonable to assume that what ever the bias is in the Squeeze integration it should be consistent across each data set. If this assumption is correct the abrupt increase in the electron count at 3.00 GPa does appear to indicate that some surrounding hydrostatic medium is being pushed into the crystal voids. A similar effect has been observed in the porous zeolitic imidazole framework ZIF-8 at high pressure.[27]

### 4.3.3  Effect of Pressure on the structures

The unit cells of both compounds contract as pressure increases (Tables 1 and 2). It should be noted that compound **8** has a slightly larger cell volume at 0.18 GPa and 300 K (2517.49(9) $Å^3$) than at ambient pressure and 150 K (2536.2(3) $Å^3$); in this case 0.18 GPa of pressure is not enough to overcome thermal expansion. Two perchlorate anions which are disordered in the low temperature, ambient pressure structure become ordered at 0.18 GPa. Perchlorate anions are notoriously susceptible to disorder even at low temperature, as seen here for **8** at 150 K, and it is notable that in this case high pressure was a more effective means to force the structure to become ordered, even at ambient temperature.

**Table 4** Bond distances and angles in **8** as a function of pressure.

| Pressure (GPa) | Mn1-O3 | Mn1-O4 | Mn1-N44 | Mn1-N41 |
|---|---|---|---|---|
| **0** | 1.8419(15) | 1.8621(15) | 2.1093(19) | 2.2053(18) |
| **0.18** | 1.823(7) | 1.842(13) | 2.084(5) | 2.219(4) |
| **1.00** | 1.834(8) | 1.908(15) | 2.082(6) | 2.226(4) |
| **2.00** | 1.817(11) | 1.78(2) | 2.072(8) | 2.194(7) |
| **Δ/σ** | 2.4 | 4.1 | 4.6 | 1.3 |
| Pressure (GPa) | Mn1-N32 | Mn1-N29 | Mn1-O3-Mn2 | Mn1-Mn2 |
| **0** | 2.1666(19) | 2.2221(18) | 96.42(7) | 2.7058(4) |
| **0.18** | 2.173(12) | 2.163(4) | 98.1(7) | 2.700(2) |
| **1.00** | 2.232(12) | 2.162(4) | 96.1(7) | 2.688(2) |
| **2.00** | 2.245(16) | 2.142(6) | 95.6(11) | 2.676(4) |
| **Δ/σ** | -5 | 12.1 | 0.7 | 7.3 |
| Pressure (GPa) | Mn2-O3 | Mn2-O4 | Mn2-N5 | Mn2-N8 |
| **0** | 1.7867(15) | 1.7753(15) | 2.0971(18) | 2.0160(18) |
| **0.18** | 1.749(14) | 1.778(7) | 2.078(5) | 2.008(4) |
| **1.00** | 1.781(15) | 1.756(8) | 2.123(6) | 2.014(4) |
| **2.00** | 1.79(2) | 1.740(10) | 2.144(8) | 2.002(6) |
| **Δ/σ** | 0.3 | 3.6 | -5.3 | 2.2 |
| Pressure (GPa) | Mn2-N17 | Mn2-N20 | Mn1-O4-Mn2 | |
| **0** | 2.0813(18) | 2.0165(18) | 96.09(7) | |
| **0.18** | 2.074(10) | 1.996(4) | 96.6(7) | |
| **1.00** | 2.065(9) | 2.007(4) | 94.3(7) | |
| **2.00** | 2.060(13) | 2.021(5) | 98.7(11) | |
| **Δ/σ** | 1.6 | -1 | 2.4 | |

Intermolecular interactions are generally weak, and the compression in the crystal of **8** is mainly driven by the reduction of the voids (Figs. 2 and 3). Void volumes can be estimated using a tool available in Platon,[22] and at 0.18 GPa the void/volume ratio is approximately 4.5 % of the total unit cell volume, whereas at 2.00 GPa the ratio has decreased to 3 % (a probe radius of 0.8 Å was used for these calculations). The same observation cannot be made for compound **9**·2CH$_3$CN·1H$_2$O because of the uncertainty related to the presence or absence of solvent molecules.

Distortions of the intramolecular bond lengths and angles in **8** are also observed (Table 4). The Mn-Mn distance contracts from 2.7058(4) Å at ambient pressure to 2.676(4) Å at 2 GPa, likely due to the significant contraction of both Mn-O4 bonds. Alterations to the Mn-O3 distances are statistically insignificant and so is the behaviour of the Mn1-O4-Mn2 angle. There are also significant changes in the Mn1(Mn$^{3+}$)-N bond lengths, which sees two of the four decreasing and one (N32) increasing (Table 4). The Jahn-Teller axis (N41-Mn1-N29), is significantly shortened as the Mn1-N29 bond contracts from 2.2221(18) Å down to 2.142(6) Å.

**Table 5** Bond distances and angles in **9**·2CH$_3$CN·1H$_2$O as a function of pressure.

| Pressure (GPa) | Mn1-O3 | Mn1-O4 | Mn1-N29 | Mn1-N32 |
|---|---|---|---|---|
| **0** | 1.847(2) | 1.850(2) | 2.212(3) | 2.128(3) |
| **0.45** | 1.833(7) | 1.831(6) | 2.189(5) | 2.137(6) |
| **1.23** | 1.835(7) | 1.839(7) | 2.178(5) | 2.115(6) |
| **1.75** | 1.833(6) | 1.835(6) | 2.173(5) | 2.113(6) |
| **3.00** | 1.824(9) | 1.839(9) | 2.157(7) | 2.086(8) |
| **4.55** | 1.828(10) | 1.821(11) | 2.148(8) | 2.085(9) |
| **Δ/σ** | 1.9 | 2.6 | 7.5 | 4.5 |

| Pressure (GPa) | Mn1-N41 | Mn1-N44 | Mn1-O3-Mn2 | Mn1-Mn2 |
|---|---|---|---|---|
| **0** | 2.220(3) | 2.134(3) | 97.00(11) | 2.7177(7) |
| **0.45** | 2.207(6) | 2.144(7) | 97.1(3) | 2.706(2) |
| **1.23** | 2.193(6) | 2.127(7) | 96.5(4) | 2.702(2) |
| **1.75** | 2.178(5) | 2.127(6) | 95.3(3) | 2.698(2) |
| **3.00** | 2.178(7) | 2.097(8) | 97.0(5) | 2.691(3) |
| **4.55** | 2.156(8) | 2.084(9) | 96.5(4) | 2.672(3) |
| **Δ/σ** | 7.5 | 5.3 | 1.2 | 14.8 |

| Pressure (GPa) | Mn2-O3 | Mn2-O4 | Mn2-N5 | Mn2-N8 |
|---|---|---|---|---|
| **0** | 1.781(2) | 1.779(2) | 2.077(3) | 2.008(3) |
| **0.45** | 1.773(6) | 1.781(7) | 2.072(6) | 2.002(5) |
| **1.23** | 1.786(6) | 1.795(7) | 2.077(6) | 2.002(5) |
| **1.75** | 1.792(6) | 1.797(6) | 2.067(6) | 2.004(5) |
| **3.00** | 1.767(9) | 1.797(9) | 2.054(8) | 1.992(7) |
| **4.55** | 1.752(12) | 1.791(11) | 2.029(8) | 1.998(8) |
| **Δ/σ** | 2.4 | 1.1 | 5.6 | 1.2 |

| Pressure (GPa) | Mn2-N17 | Mn2-N20 | Mn1-O4-Mn2 | |
|---|---|---|---|---|
| **0** | 2.078(3) | 2.017(3) | 96.97(11) | |
| **0.45** | 2.090(6) | 2.023(6) | 97.1(3) | |
| **1.23** | 2.064(6) | 2.009(6) | 96.1(3) | |
| **1.75** | 2.058(6) | 2.013(5) | 96.0(3) | |
| **3.00** | 2.035(8) | 2.003(7) | 95.5(5) | |
| **4.55** | 2.017(9) | 1.982(8) | 95.4(5) | |
| **Δ/σ** | 6.4 | 4.1 | 3.1 | |

For Mn2 (Mn$^{4+}$) the changes are less significant, with the exception of Mn1-N5 bond which increases from 2.078(5) at 0.18 GPa to 2.144(8) Å at 2.00 GPa.

**9**·2CH$_3$CN·1H$_2$O shows essentially analogous behaviour: the Mn-Mn distance contracts from 2.7177(7) Å at ambient pressure to 2.672(3) Å at 4.55 GPa. This seems likely that this change should be accompanied by a decrease in the Mn-O distances and Mn-O-Mn angles, but, because the standard uncertainties at high pressure are large, the variations observed (Table 5) are not statistically significant. For Mn1(Mn$^{3+}$) all four bonds to the N-atoms shrink significantly (Table 5), and the same trend is observed in three of the four Mn2(Mn$^{4+}$)-N bonds. These bond length changes are somewhat unusual as all our previous studies on transition metal cluster

complexes have shown them to be somewhat resistant to pressure effects.[4, 5] Our attempts to analyse the structures at higher pressures were unfortunately hindered by the degradation of the crystals.
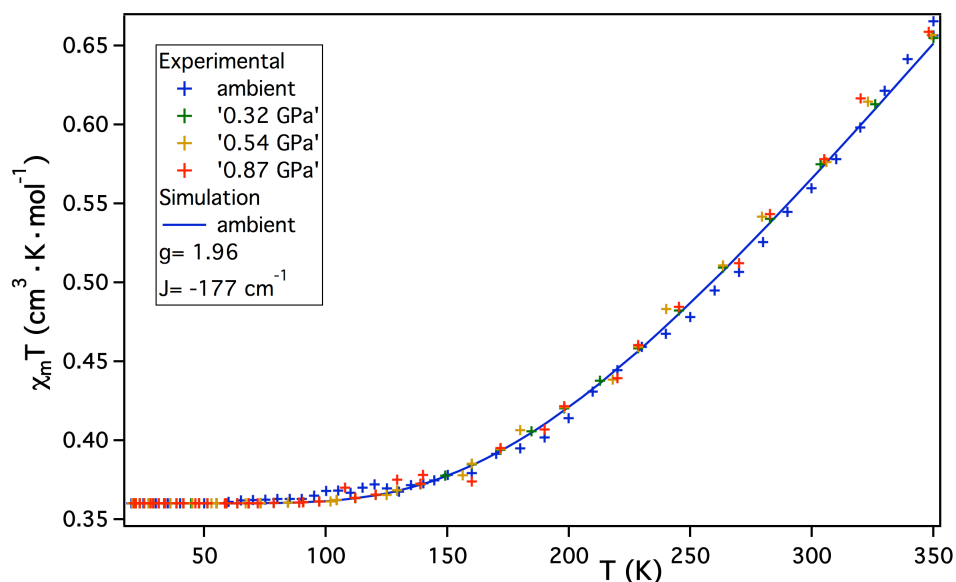


**Figure 6** Plots of $\chi_M T$ versus T for **8** recorded in the 350-20 K temperature range at the indicated pressures; the solid lines represent simulations of the data.

## 4.3.4 Effect of Pressure on magnetism

Variable temperature magnetic susceptibility data were collected on **8** and **9**·2CH$_3$CN·1H$_2$O in the temperature range 350-20 K in an applied field of 1 kG at ambient and three different pressures and is plotted as the $\chi_m T$ product versus T in Figures 6 and 7. The magnetic behaviour of **8** and **9**·2CH$_3$CN·1H$_2$O under ambient pressure is analogous to that previously reported for monoclinic analogue of **8**.[28] Simulations of the susceptibility data (Figures 6 and 7) using the Hamiltonian of Eqn (1) suggest strong antiferromagnetic exchange in **8** ($J$ = -177 cm$^{-1}$ $g$ = 1.96) and in **9**·2CH$_3$CN·1H$_2$O ($J$ = -185 cm$^{-1}$ $g$ = 1.98).[29]

$$\hat{H} = -2J\left(\hat{S}_1 \cdot \hat{S}_2\right) \qquad (1)$$

complexes is constant at ~0.36 cm$^3$·K·mol$^{-1}$. Above 100 K the value then increases steadily with temperature reaching values of 0.66 cm$^3$·K·mol$^{-1}$ (**8**) and 0.64 cm$^3$·K·mol$^{-1}$ (**9**) at 350 K. As can be seen from Figures 6 and 7 the variable pressure

data sets are essentially super-imposable on the ambient pressure data. The independence of the magnetic properties with pressure (up to 0.87 GPa for **8** and 0.84 GPa for **9)** is consistent with the minimal structural change below 1 GPa. Unfortunately, a lack technology does not allow us to measure the susceptibility at the higher pressures where the major structural changes occurred.
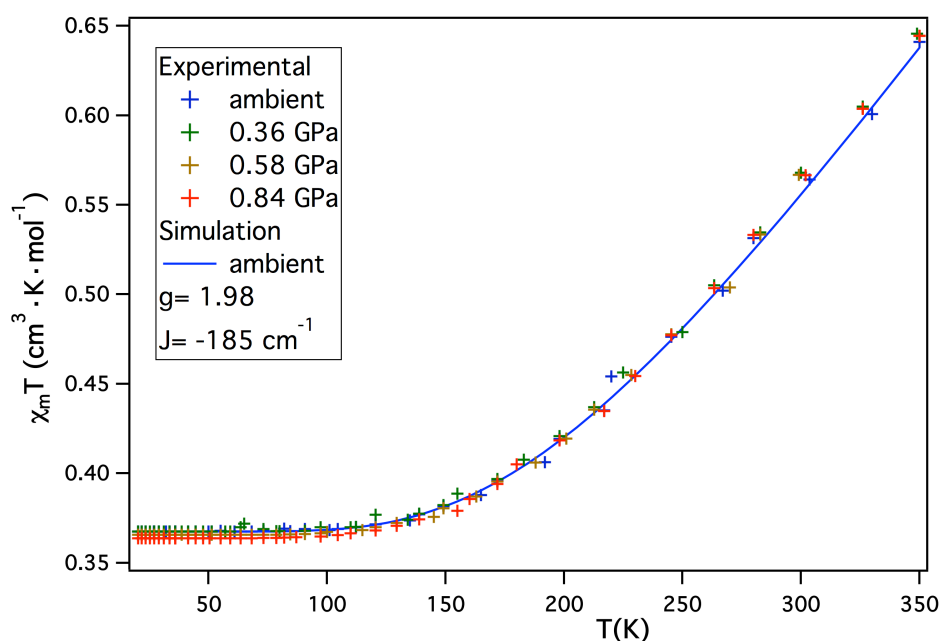


**Figure 7** Plots of $\chi_M T$ versus T for **9** recorded in the 350-20 K temperature range at the indicated pressures; the solid lines represent simulations of the data.

## 4.4 Conclusions

We have presented a rare example of the combined use of high-pressure magnetometry and high-pressure single-crystal X-ray crystallography to study two dinuclear oxo-bridged mixed-valent $Mn^{III}/Mn^{IV}$ complexes. Magnetic data were recorded up to 0.87 GPa for **8** and 0.84 GPa for **9**·$2CH_3CN$·$1H_2O$, with structural data available up to 2.00 GPa for **8** and 4.55 GPa for **9**·$2CH_3CN$·$1H_2O$. The significant decrease in the cell volumes below 1 GPa occur *via* the compression of interstitial voids, with little change in the intra-molecular bond lengths and angles, and consequently there are no changes in the variable temperature susceptibility. Above 1 GPa the metal-metal separations decrease and there are changes to both the bond lengths and bond angles that, in average, tend to decrease. The development of

a new low-background pressure cell suitable for magnetic measurements above 1.0 GPa is in progress to investigate the magnetic behaviour of these samples in the pressure range where structural modifications occur.

## 4.5  References

1.    A. Prescimone, C. J. Milios, S. A. Moggach, J. E. Warren, A. R. Lennie, J. Sanchez-Benitez, K. Kamenev, R. Bircher, M. Murrie, S. Parsons and E. K. Brechin, *Angew. Chem. Int. Ed.*, 2008, **47**, 2828.
2.    A. Prescimone, C. J. Milios, J. Sanchez-Benitez, K. Kamenev, C. Loose, J. Kortus, S. A. Moggach, M. Murrie, J. E. Warren, A. R. Lennie, S. Parsons and E. K. Brechin, *Dalton Trans.*, 2009, 4858.
3.    A. Prescimone, S. A. Moggach, J. Sanchez-Benitez, K. V. Kamenev, J. E. Warren, A. R. Lennie, S. Parsons and E. K. Brechin, *Dalton Trans.*, 2010, **39**(1), 113.
4.    A. Prescimone, J. Sanchez-Benitez, K. Kamenev, S. A. Moggach, M. Murrie, J. E. Warren, A. R. Lennie, S. Parsons and E. K. Brechin, *Dalton Trans.*, 2009, 7390.
5.    A. Prescimone, J. Sanchez-Benitez, K. Kamenev, S. A. Moggach, J. E. Warren, A. R. Lennie, S. Parsons and E. K. Brechin, *Z. Naturforsch. B.*, 2010, **in print**.
6.    A. Bencini and D. Gatteschi, *EPR of exchange Coupled Systems*, Springer-Verlag, Berlin, 1990.
7.    S. R. Cooper and M. Calvin, *J. Am. Chem. Soc.*, 1977, **99**, 6623.
8.    L. Merrill and W. A. Bassett, *Rev. Sci. Instrum.,* 1974, **45**, 290.
9.    S. A. Moggach, D. R. Allan, S. Parsons and J. E. Warren, *J. Appl. Crystallogr.*, 2008, **41**, 249.
10.   G. J. Piermarini, S. Block, J. D. Barnett and R. A. Forman, *J. Appl. Phys.*, 1975, **46**, 2774.
11.   Bruker-Nonius, Madison, Wisconsin, USA, Editon edn., 2004, pp. Area-Detector Integration Software.
12.   D. R. Allan, S. Parsons and S. J. Teat, *J. Synchr. Rad.*, 2001, **8**, 10.
13.   A. Dawson, D. R. Allan, S. Parsons and M. Ruf, *J. Appl. Crystallogr.*, 2004, **37**, 410.
14.   Bruker-Nonius, Bruker-AXS, Madison, Wisconsin, USA, Editon edn., 2006.
15.   G. M. Sheldrick, Bruker-AXS, Madison, WIsconsin, USA, Editon edn., 2004.
16.   S. Parsons, The University of Edinburgh, Edinburgh, United Kingdom, Editon edn., 2004.
17.   R. H. Blessing, *J. Appl. Crystallogr.*, 1997, **30**, 421.
18.   Bruker-Nonius, Bruker-AXS, Madison, Wisconsin, USA, Editon edn., 2002.
19.   L. J. Farrugia, *J. Appl. Crystallogr.*, 1999, **32**, 837.
20.   D. J. Watkin, K. Prout, J. R. Carruthers, P. W. Betteridge and R. I. Cooper, Chemical Crystallography Laboratory, University of Oxford, Oxford, UK, Editon edn., 2003.
21.   P. Van der Sluis and A. L. Spek, *Acta Cryst.*, 1990, **A46**, 194.
22.   A. L. Spek, Utrecht University, Utrecht, The Netherlands, Editon edn., 2004, A multipurpose Crystallographic Tool.

23.    C. F. Macrae, I. J. Bruno, J. A. Chisholm, P. R. Edgington, P. McCabe, E. Pidcock, L. Rodriguez-Monge, R. Taylor, J. Van de Streek and P. A. Wood, *J. Appl. Cryst.*, 2008, **41**, 466.

24.    K. Brandenburg and H. Putz, Crystal Impact, Bonn, Germany, Editon edn., 2005.

25.    K. V. Kamenev, S. Tancharakorn, N. Robertson and A. Harrison, *Rev. Sci. Instrum.*, 2006, **77**, 073905.

26.    P. M. Plaksin, R. C. Stoufer, M. Mathew and G. J. Palenik, *J. Am. Chem. Soc.*, 1972, **94**, 2121.

27.    S. A. Moggach, T. D. Bennett and A. Cheetham, *Angew. Chem. Int. Ed.*, 2009, **48**, 7087.

28.    R. I. Cooper, G. C. Dismukes, M. P. Klein and M. Calvin, *J. Am. Chem. Soc.*, 1978, **100**, 7248.

29.    M. Stebler, A. Ludi and H.-B. Bürgi, *Inorg. Chem.*, 1986, **25**, 4743.